



# Durham E-Theses

---

## *Liquid crystal devices in adaptive optics*

Birch, Philip Michael

### How to cite:

---

Birch, Philip Michael (1999) *Liquid crystal devices in adaptive optics*, Durham theses, Durham University. Available at Durham E-Theses Online: <http://etheses.dur.ac.uk/4792/>

### Use policy

---

The full-text may be used and/or reproduced, and given to third parties in any format or medium, without prior permission or charge, for personal research or study, educational, or not-for-profit purposes provided that:

- a full bibliographic reference is made to the original source
- a [link](#) is made to the metadata record in Durham E-Theses
- the full-text is not changed in any way

The full-text must not be sold in any format or medium without the formal permission of the copyright holders.

Please consult the [full Durham E-Theses policy](#) for further details.

# BRITISH THESIS SERVICE

**DX213261**

**Awarding Body : Durham**

**Thesis By : BIRCH Philip Michael**

**Thesis Title : LIQUID CRYSTAL DEVICES IN ADAPTIVE OPTICS**

**We have assigned this thesis the number given at the top of this sheet.**

**THE BRITISH LIBRARY  
DOCUMENT SUPPLY CENTRE**

# Liquid Crystal Devices in Adaptive Optics

by

Philip Michael Birch B.Sc. (Dunelm)

The copyright of this thesis rests with the author. No quotation from it should be published without the written consent of the author and information derived from it should be acknowledged.



19 JUL 2000

A Thesis Submitted to the University of Durham for the  
Degree of Doctor of Philosophy

School of Engineering

1999

## **Abstract**

Large aperture astronomical telescopes have a resolution that is limited by the effects of the Earth's atmosphere. The atmosphere causes incoming wavefronts to become aberrated, to correct for this adaptive optics is employed. This technique attempts to measure the incident wavefront and correct it, restoring the original image. Conventional techniques use mirrors that are deformed with piezo-electric crystals, this thesis uses an alternative technique. Two different types of liquid crystal spatial light modulators are used as the corrective elements. The advantages and disadvantages of both are assessed in an attempt to find which system is the best for astronomical adaptive optics.

## Preface

No part of the above thesis has been submitted for a degree in this or any other university. The work here is the author's own except work on the real time system in chapter 8 which was carried out in collaboration with Dr James Gourlay.

Some of the work in this thesis has been published in the following:

- Philip M. Birch, James D. Gourlay, Nathan P Doble, Alan Purvis, "Real time adaptive optics correction with a ferroelectric spatial light modulator and Shack-Hartmann wavefront sensor." *Proc. Soc. Photo-Opt. Instrum. Eng.* **3126** pp185-190 (1997)
- James Gourlay, Gordon D. Love, Philip M. Birch, Ray M. Sharples, Alan Purvis, "A real-time closed-loop liquid crystal adaptive optics system: first results." *Optics Communications* **137** pp17-21 (1997)
- Philip M. Birch, James Gourlay, Gordon D. Love, Alan Purvis, "Real time optical aberration correction with a ferroelectric liquid crystal spatial light modulator." *Applied Optics* **37** (11) pp 2164-2169 (1998)

The copyright of this thesis rests with the author. No quotation from it should be published without prior consent and information derived from it should be acknowledged.

## Acknowledgements

I would like to thank the following people for the help and support they have given me over the years.

- ◆ James Gourlay, Gordon Love and the rest of the Durham Astronomical Instrumentation group.
- ◆ My supervisor Alan Purvis.
- ◆ The staff in Engineering.
- ◆ Joanna
- ◆ The people at college who have made life fun (Cheryl, Jim, Flo, Mike, Rich, Dave, Alan, Lee, Jason, Mark, Marita, Ste, Floriane, Sarah).
- ◆ The people at college who have made life hell (no names mentioned here).
- ◆ My parents.
- ◆ Nathan Doble.
- ◆ Mischief and Cleo for their wet noses.

# Table of Contents

<b>ABSTRACT</b> .....	<b>I</b>
<b>PREFACE</b> .....	<b>II</b>
<b>ACKNOWLEDGEMENTS</b> .....	<b>III</b>
<b>TABLE OF CONTENTS</b> .....	<b>IV</b>
<b>CHAPTER 1: INTRODUCTION</b> .....	<b>1</b>
INTRODUCTION.....	1
CHAPTER CONTENT.....	2
COMMON ACRONYMS .....	3
SOME COMMONLY USED MATHEMATICAL SYMBOLS .....	4
<b>CHAPTER 2: LIQUID CRYSTAL THEORY</b> .....	<b>5</b>
INTRODUCTION .....	5
HISTORY .....	5
LIQUID CRYSTAL THEORY .....	5
<i>Types of Liquid Crystal</i> .....	7
<i>The Effect of Electric Fields on Liquid Crystals</i> .....	10
<i>The Effect on Light of Liquid Crystals</i> .....	10
<i>Phase Shifting by Nematic Liquid Crystals</i> .....	11
<i>Phase Shifting by Ferroelectric Liquid Crystals</i> .....	13
<i>FLC Operated with No Polarisers</i> .....	18
APPLICATIONS OF LIQUID CRYSTALS .....	20
<i>Multiplexing Theory</i> .....	23
SUMMARY .....	24
<b>CHAPTER 3: CONVENTIONAL ADAPTIVE OPTICS</b> .....	<b>25</b>
INTRODUCTION.....	25
<i>The Function of an Astronomical Telescope and the History of Adaptive Optics</i> .....	25
<i>Terminology</i> .....	27
WAVEFRONT DISTORTIONS CAUSED BY THE ATMOSPHERE.....	28
<i>Intensity Variations</i> .....	31
<i>Temporal Variations</i> .....	31
<i>Temporal Power Spectrum</i> .....	31
<i>Wavelength Dependence of Atmospheric Turbulence</i> .....	32
<i>Zernike Modes and the Representation of the Spatial Distortions of the Wavefront</i> .....	33
CONVENTIONAL ADAPTIVE OPTICS .....	37
<i>The Need for Adaptive Optics</i> .....	37
<i>Phase Conjugation</i> .....	38
DEFORMABLE MIRRORS .....	38
WAVEFRONT SENSORS .....	40

<i>Direct Sensing and Interferometers</i> .....	41
<i>The Smartt or Point Diffraction Interferometer</i> .....	41
THE SHACK-HARTMANN WAVEFRONT SENSOR .....	42
<i>Spot Centroiding</i> .....	43
<i>Modes from Tilts - The Interaction Matrix</i> .....	44
<i>Wavefront Curvature</i> .....	46
BINARY ADAPTIVE OPTICS .....	47
<i>Binary Adaptive Optics Theory</i> .....	47
<i>Binary Adaptive Optics and Higher Order Correction with FLCs</i> .....	48
NON-ASTRONOMICAL ADAPTIVE OPTICS APPLICATIONS .....	49
SUMMARY .....	51
<b>CHAPTER 4: A MULTIPLEXED NEMATIC LIQUID CRYSTAL</b>	
<b>SLM</b> .....	<b>52</b>
INTRODUCTION.....	52
DEVICE DESCRIPTION.....	52
EXPERIMENTAL .....	55
<i>Voltage Waveform Measurements</i> .....	55
<i>Phase Shift Measurements</i> .....	55
<i>Voltage Measurements Results</i> .....	57
<i>Phase Shift Measurement Results</i> .....	62
DISCUSSION .....	64
SUMMARY .....	66
<b>CHAPTER 5: BINARY CORRECTION WITH A POINT DIFFRACTION</b>	
<b>INTERFEROMETER</b> .....	<b>67</b>
INTRODUCTION.....	67
BACKGROUND.....	67
<i>Standard Reference Arm Interferometric Techniques</i> .....	69
THEORETICAL CONSIDERATIONS.....	69
<i>The Smartt or Point Diffraction Interferometer</i> .....	69
<i>PDI/FLC System Considerations</i> .....	73
<i>Computer Simulation</i> .....	76
<i>Computer Simulation Results</i> .....	77
EXPERIMENTAL FLC/PDI SYSTEM.....	83
<i>Set-up</i> .....	83
<i>Control Hardware</i> .....	84
<i>Control Software</i> .....	85
<i>Correction Results</i> .....	87
<i>FLC Optical Throughput</i> .....	92
DISCUSSION .....	92
<i>Photon Flux</i> .....	93
<i>Future Considerations</i> .....	96
SUMMARY .....	97
<b>CHAPTER 6: A LIQUID CRYSTAL ATMOSPHERIC TURBULENCE</b>	
<b>SIMULATOR</b> .....	<b>98</b>
INTRODUCTION.....	98
BACKGROUND.....	98

INTRODUCTION.....	98
BACKGROUND.....	98
REQUIREMENTS FOR AN ATMOSPHERIC TURBULENCE SIMULATOR (ATS).....	99
A LIQUID CRYSTAL SLM AS AN ATS .....	100
MEADOWLARK HEX69 DEVICE DESCRIPTION.....	100
<i>Driving the Hex69</i> .....	102
THE HEX69 AS AN ATS .....	103
<i>Phase Screen Generation Methods</i> .....	103
<i>Lane's Fourier Method</i> .....	103
<i>Software</i> .....	104
ATS PERFORMANCE MEASUREMENTS .....	106
<i>The Shack-Hartmann Wavefront Sensor</i> .....	106
<i>Hardware and Optical Set-Up</i> .....	107
<i>Calibration of the Hex69</i> .....	110
<i>Temporal Response of the Hex69</i> .....	110
<i>Shack-Hartmann Software</i> .....	114
<i>Calibration of System</i> .....	115
<i>System Limits</i> .....	116
EXPERIMENTAL MEASUREMENTS.....	117
<i>The Zernike Power Spectrum</i> .....	117
<i>Measurement of Temporal Characteristics</i> .....	118
<i>Strehl Ratio measurements</i> .....	120
DISCUSSION.....	121
SUMMARY .....	123
<b>CHAPTER 7: BINARY ADAPTIVE OPTICS WITH A SHACK-HARTMANN WAVEFRONT SENSOR .....</b>	<b>124</b>
INTRODUCTION.....	124
BACKGROUND.....	124
EXPERIMENTAL SYSTEM .....	125
<i>Optical Set-Up</i> .....	125
<i>Hardware Design</i> .....	126
<i>Software Design</i> .....	126
<i>Open Loop Considerations</i> .....	129
<i>Alignment</i> .....	130
<i>Predicted Performance</i> .....	130
RESULTS .....	133
<i>Static Correction</i> .....	133
<i>Real Time Correction</i> .....	135
DISCUSSION.....	137
SUMMARY .....	141
<b>CHAPTER 8: NEMATIC LIQUID CRYSTAL CORRECTION .....</b>	<b>142</b>
INTRODUCTION.....	142
BACKGROUND.....	142
DEVICE DESCRIPTION.....	143
<i>Driving Software</i> .....	143
STATIC CORRECTION.....	143

<i>The Shack-Hartmann system</i> .....	153
<i>System Alignment</i> .....	154
<i>Crosstalk Measurements</i> .....	154
<i>The Cause of the Hex69's Crosstalk</i> .....	158
<i>Laboratory Turbulence Simulation</i> .....	164
<i>Static Correction</i> .....	166
<i>Closed Loop Expectations</i> .....	167
<i>Closed Loop Correction</i> .....	168
<i>Real Telescope Trials</i> .....	169
DISCUSSION .....	169
SUMMARY .....	171
<b>CHAPTER 9: SUMMARY AND CONCLUSIONS .....</b>	<b>172</b>
INTRODUCTION.....	172
SUMMARY OF RESULTS .....	172
<i>Chapters 2 and 3</i> .....	172
<i>Chapters 4</i> .....	172
<i>Chapters 5</i> .....	173
<i>Chapters 6</i> .....	173
<i>Chapters 7</i> .....	174
<i>Chapters 8</i> .....	174
FUTURE WORK.....	176
<i>Meadowlark/ Shack-Hartmann Systems</i> .....	176
<i>FLC/ Shack-Hartmann Systems</i> .....	177
<i>Atmospheric Turbulence Simulator</i> .....	178
<b>APPENDIX 1: THE ZYGO INTERFEROMETER .....</b>	<b>179</b>
SYSTEM DESIGN.....	179
<i>The Zygo PTI Specifications</i> .....	180
<i>Zernike Mode Fitting</i> .....	181
<i>Disadvantages of Phase Shifting Interferometry</i> .....	181
<i>Additional Features</i> .....	182
<b>APPENDIX 2: THE DESIGN OF A NON-PIXELATED SLM .....</b>	<b>183</b>
BASIC DESIGN.....	183
<i>Design 1</i> .....	185
<i>Design 2</i> .....	187
<i>Design 3</i> .....	188
SUMMARY .....	190
<b>REFERENCES.....</b>	<b>191</b>

# Chapter 1: Introduction

## *1.1 Introduction*

This thesis combines two areas of research, adaptive optics and liquid crystals. Adaptive optics is currently being used in observatories to correct for aberrations in the incident wavefronts using deformable mirrors. These aberrations are caused by atmospheric turbulence in the Earth's atmosphere and inside the telescope dome. In this thesis liquid crystal spatial light modulators (SLMs) will be used instead of deformable mirrors. There will be two types of liquid crystal SLM used; both types have their individual advantages and disadvantages. These will be explored in three different adaptive optics systems. This thesis does not attempt to fully optimise each system, but to demonstrate them as proof of principles.

The concept behind adaptive optics is to have an optical component that can move, deform, or change in some way such that the incident light can be manipulated to correct for aberrations in real time. The resolution of Earth based telescopes' (without adaptive optics) is typically limited to  $\sim 1$  arcsecond. With an adaptive optics system it is theoretically possible to restore the resolution to the diffraction limit of the telescope using deformable mirrors. Compared to liquid crystal SLMs, these mirrors are very expensive, bulky and potentially have a smaller number of degrees of freedom. It would therefore be desirable to be able to use liquid crystal SLMs instead of deformable mirrors. Adaptive optics has other applications apart from astronomy, e.g., in laser welding, satellite tracking, and underwater imaging. These applications are briefly covered in chapter 3. However, this thesis is mainly concerned with astronomical adaptive optics.

This thesis contains the results of work done with two different types of liquid crystal devices and two different types of wavefront sensor. Three complete

adaptive optics systems are presented, in addition to a liquid crystal atmospheric turbulence generator. A study of a liquid crystal display device modified to produce phase only modulation is also presented.

## **1.2 Chapter Contents**

The thesis is broken down into the following chapters:

- Chapter Two describes liquid crystals. The structures of the molecules are explained and why this gives them their unusual properties when in the presence of an electric field or light.
- Chapter Three describes the cause of atmospheric turbulence. The statistics of the atmospheric turbulence are explained and the different factors affecting it are discussed. Zernike polynomials and their use are introduced. Conventional adaptive optics is also described in detail. This includes how each component of the system works and the advantages of each part are discussed. Binary adaptive optics will be explained.
- Chapter Four is the first experimental chapter. A liquid crystal SLM that was based on display technology was used. The disadvantages of this system will be demonstrated.
- Chapter Five uses 'Binary Adaptive Optics' with a self-referencing interferometer. A control algorithm for the system will be developed and computer modelling of the system will be described. Correction for an aberrated wavefront will be demonstrated.
- Chapter Six will develop an atmospheric turbulence simulator using a liquid crystal SLM. The properties of the system will be experimentally measured and compared to the theoretical models.
- Chapter Seven will use the above turbulence simulator as an aberration source for another 'binary adaptive optics' system. This system will use a liquid crystal SLM with a Shack-Hartmann wavefront sensor.

- Chapter Eight will use the same wavefront sensor as chapter seven but with a nematic liquid crystal SLM, allowing full correction of the turbulence. Crosstalk between the Zernike modes will be investigated.
- Chapter Nine summarises the results and conclusions of the above chapters. It discusses the future of liquid crystal adaptive optics in astronomy.
- Appendix 1 describes the Zygo interferometer. This device is used throughout the thesis to measure the phase shift produced by SLMs and the optical flatness of optical components.
- Appendix 2 presents a novel idea for the construction of an unpixelated liquid crystal SLM. It describes work that was done towards constructing such a device.

This thesis is in effect a study of possible liquid crystal adaptive optics systems that could be used in astronomy.

### **1.3 Common Acronyms**

ATS	Atmospheric Turbulence Simulator
DM	Deformable Mirror
DSP	Digital Signal Processor
FLC	Ferroelectric Liquid Crystal
LC	Liquid Crystal
PDI	Point Diffraction Interferometer
PSF	Point Spread Function
SLM	Spatial Light Modulator

*Table 1.1. Common acronyms.*

### 1.4 Some Commonly Used Mathematical Symbols

$\lambda$	Wavelength of light. Usually taken as 632.8nm unless otherwise stated
$\hat{n}$	Liquid crystal director
$\phi$	Phase
$\xi$	Path length
$\sigma$	Variance
<b>a</b>	Zernike amplitude matrix
<b>B</b>	Interaction matrix
<i>D</i>	Telescope diameter
$D_\phi$	Structure function
$f_0$	Greenwood frequency
$n_e$	Extraordinary refractive index
$n_o$	Ordinary refractive index
$r_0$	Fried parameter
$v_w$	Wind speed
$Z_j$	$j^{\text{th}}$ Zernike mode

Table 1.2. Some commonly used Mathematical Symbols.

## Chapter 2: Liquid Crystal Theory

### **2.1 Introduction**

In this chapter, the theory of liquid crystals will be briefly described as well as current applications, limitations, and the future potential of liquid crystals.

### **2.2 History**

The person usually credited with the discovery of liquid crystals was an Austrian botanist named Friedrich Reinitzer. In 1888, he noticed that a substance related to cholesterol appeared to have 'two melting points'. At 145°C the substance melted into a cloudy liquid and at 178°C this liquid became clear. This discovery was followed up by the German physicist Otto Lehmann. He found the cholesterol that Reinitzer had been studying had the optical properties of a crystal but flowed like a liquid when it was between the two melting points. He coined the phrase 'liquid crystal' for the new substance.

For a long time this new phase of matter was nothing but a scientific curiosity. In the late 1960's the first crude displays were built. In the 1970's, the first stable liquid crystals with transitional temperatures such that they could be used at room temperature were developed. It was this breakthrough that has started the explosion in liquid crystal technology we see today.

### **2.3 Liquid Crystal Theory**

Most people are aware of the 3 states of matter: solids, liquids, and gases. These states, or phases, come about because of the relationship between the vibrational energy of atoms and molecules, and the bonding forces holding them together.

In the solid state molecules are highly ordered and are strongly bonded. The molecules are held rigidly and in crystalline solids have a specific orientation. In a liquid, the molecules have more vibrational energy, the molecules break away

and become free to move around and re-orientate themselves randomly. The substance now has much less order, but the bonding forces are still strong enough to hold the molecules closely together. Gases have even more energy, the attractive forces are no longer strong enough to hold together the molecules and they are free to move independently to fill the entire container holding them.

However several other states of matter exist. If a gas is heated further it becomes completely ionised and is called a plasma. Between the liquid and the solid phases some molecules exhibit a liquid crystal phase.

Liquid crystals have some properties of both solids and liquids. This is because of the shape and rigidity of the molecules. The types of liquid crystal used in this thesis have “rod” shaped molecules. The rigidity often comes from benzene rings forming the backbone of the molecule (figure 2.1). A unit vector called the director,  $\hat{n}$ , is defined as being co-linear with the long axis of the molecule.

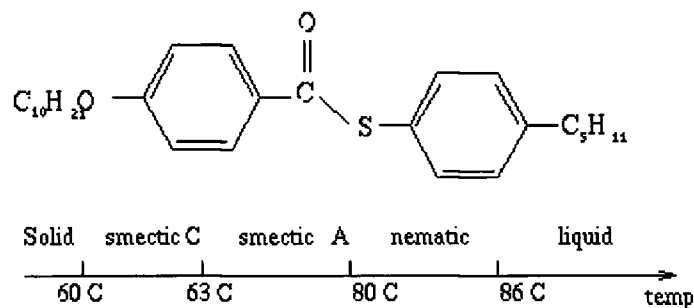


*Figure 2.1. An example liquid crystal molecule, 4-n-pentylbenzenethio-4'-n-decyloxybenzoate. The benzene rings give the molecule its rigidity. This liquid crystal exhibits several phases at different temperatures (see below).*

When the molecules are in the solid state they are held rigidly together. The molecules will be orientated such as to minimise the free energy. In the simplest case, this is when all of the directors are in the same direction. When the molecules are heated, they gain enough energy to melt into the liquid crystal

phase. The molecules lose their positional order and become free to move around. Because of the molecules rigid rod shape the molecules can not easily rotate and so they still maintain their orientation. The time averaged direction of the director is still in the same direction. If the substance is given further energy the molecules overcome this orientational order and the substance becomes a normal isotropic liquid.

### 2.3.1 TYPES OF LIQUID CRYSTAL

There are several types of liquid crystal. In the *nematic* liquid crystal phase the molecules are free to flow, but it is energetically more favourable for them to orientate themselves in the same direction (i.e., the molecules have orientational order, but no positional order) (figure 2.2). In another type of liquid crystal it is more favourable for one molecule to align itself to its neighbour with its director at a slightly different angle. This has the effect of rotating the director in a helix structure (figure 2.3). This type is known as *cholesteric* or *chiral nematic* liquid crystal.

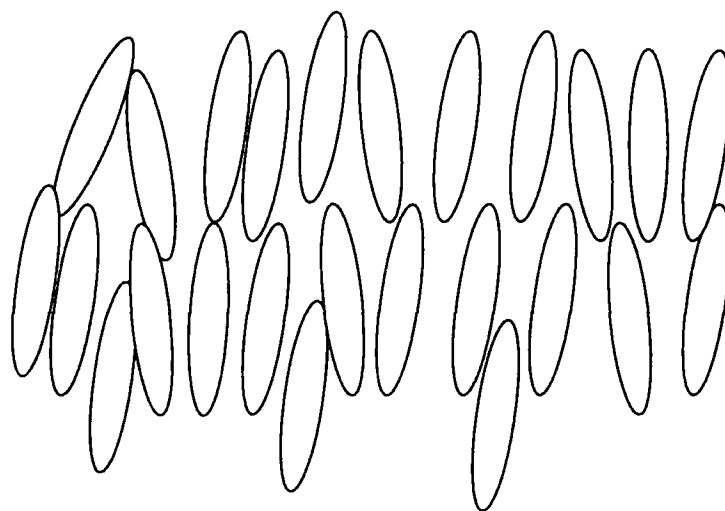


*Figure 2.2. A snap shot of the molecules in nematic liquid crystal. On average the molecules point in the same direction.*

The other type of liquid crystal based upon a rod shaped molecule is called *smectic*. There are too large a number of subsets of smectic liquid crystals to

cover here, but they are characterised by their molecules having some positional order in layers as well as orientational order (see figure 2.4). A type of smectic liquid crystal used in this thesis is known as *smectic C\** or *chiral smectic C*. The molecules are arranged into layers with their directors at some angle (other than  $90^\circ$ ) to the plane of the layer. This angle is the same in all the layers but the director outlines a cone as it rotates over a number of layers. The distance it takes the director to be rotated  $360^\circ$  is known as the pitch.

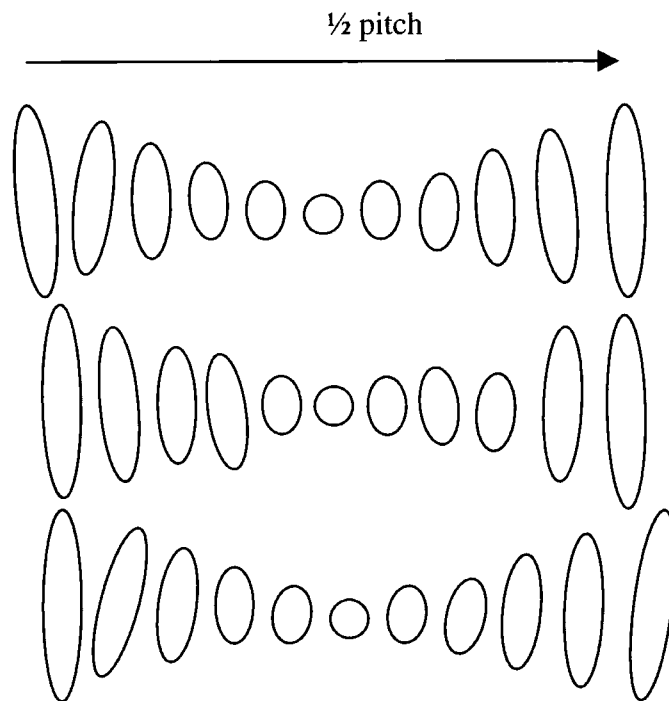


*Figure 2.3. A snap shot of the molecules in cholesteric or chiral nematic. The directors are rotated by some angle from one molecule to the next. The distance it takes for a  $360^\circ$  rotation is known as the pitch.*

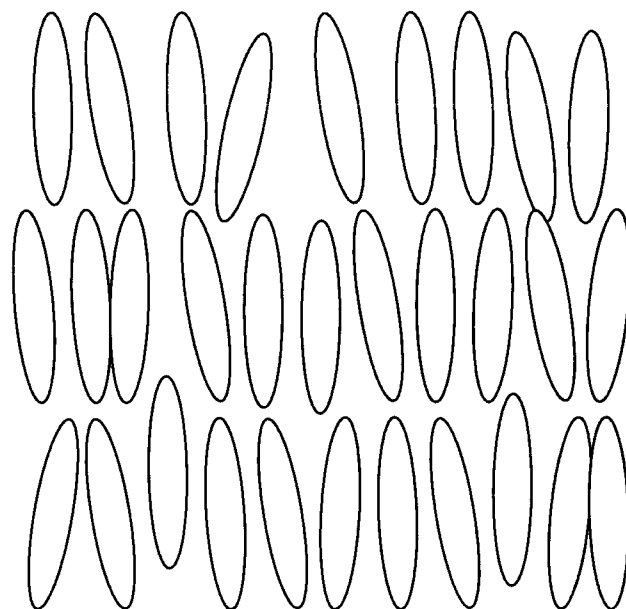


*Figure 2.4. A snap shot of smectic A. These molecules have positional order in regularly spaced layers.*

The liquid crystals described here change their states according to temperature. They can exist in more than one of the above states at different temperatures. For this reason they are known as *thermotropic* liquid crystals. An example phase diagram is given in figure 2.1 for *4-n-pentylbenzenethio-4'-n-decyloxybenzoate*. It is not possible for molecules to exhibit both the nematic and the chiral nematic state at any temperature but they can have more than one type of smectic state.

There are other types of liquid crystal based upon circular disk shaped molecules. These are known as *discotic* liquid crystals. They also exhibit nematic, chiral nematic and smectic states. Other types exist, some are based upon polymers that have display applications; *lyotropic* liquid crystals are important in biology.

In this thesis we are only concerned with nematic and smectic C\* liquid crystal based devices.

### 2.3.2 THE EFFECT OF ELECTRIC FIELDS ON LIQUID CRYSTALS

The molecules used in liquid crystal applications have an overall neutral electric charge. However, certain atoms within the molecules are more electrophilic (they attract electrons) than others. This gives the atoms a slight negative electric charge. If a liquid crystal molecule has electrophilic and electrophobic (repels electrons) atoms there will be a permanent electric dipole. If these molecules are placed in an electric field, the dipole will produce a rotational torque,  $\mathbf{T}$ ,

$$\mathbf{T} = \mathbf{P} \times \mathbf{E} \quad [2.1]$$

where  $\mathbf{E}$  is the electric field and  $\mathbf{P}$  is the dipole moment. This torque rotates the molecule, aligning it with the electric field. When the electric field is removed the molecule will return to its original orientation.

In practice, a DC field would cause the liquid crystal cell to degrade. An AC field is instead applied. When an AC electric field is applied to a molecule, the field causes electrons to be displaced within the molecule. This displacement of charge causes an *induced dipole moment*. In an AC field, equation [2.1] would have a time average of zero if the dipole was static, but because of the electron mobility within the molecule, the induced dipole can flip polarity at the same frequency as the applied AC field (~1kHz) giving a non-zero value for  $\mathbf{T}$ .

### 2.3.3 THE EFFECT ON LIGHT OF LIQUID CRYSTALS

Elongated molecules have different dielectric constants, and hence different refractive indices, for each of their axes. In an isotropic liquid the effect is averaged out so the material will be optically isotropic. In crystalline solids, such as quartz and in liquid crystals, the refractive index for the whole crystal will be different for light entering in different polarisation states. The crystal is birefringent. The long axis of the liquid crystal has what is called the

*extraordinary* refractive index, and the two shorter axes have what is called the *ordinary* refractive index (figure 2.5).

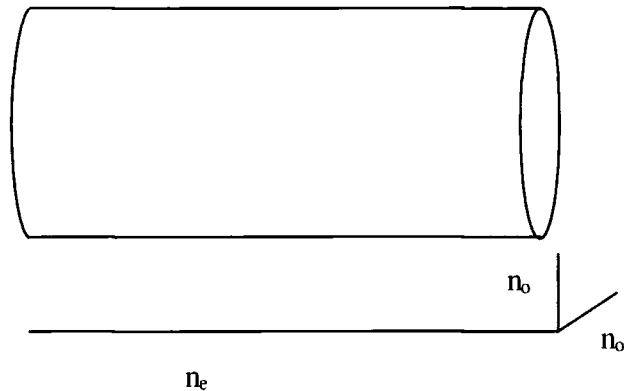


*Figure 2.5. The anisotropic rod shaped nature of the liquid crystal molecules gives rise to their isotropic refractive indices and the molecules' birefringence.*

The birefringence of the liquid crystal is defined as

$$\Delta n = n_e - n_o \quad [2.2]$$

where  $n_e$  is the extraordinary refractive index and  $n_o$  the ordinary. It is often useful to think of homogenous liquid crystals as being variable linear waveplates.

### 2.3.4 PHASE SHIFTING BY NEMATIC LIQUID CRYSTALS

Consider a glass cell of nematic liquid crystal with incident light polarised along the extraordinary axis. The phase shift,  $\phi$ , experienced by the incident light linearly polarised along the extraordinary axis compared to the phase shift along the ordinary axis as it passes through the liquid crystal of thickness  $d$ , will be

$$\phi = \frac{2\pi}{\lambda} d \cdot \Delta n \quad [2.3]$$

where  $\Delta n$  is the effective birefringence experienced by the light and  $\lambda$  is the wavelength of the light.  $\Delta n$  is a function of voltage and is at its maximum when there is no electric field across the liquid crystal cell. If an electric field is now applied across the cell, the liquid crystal molecules will be rotated. The light will experience less of the extraordinary refractive index of the material and the value of  $\Delta n$  will decrease. Hence, the phase shift caused by the liquid crystal material will be different.

Because the liquid crystal is driven by an AC field, it is only possible to drive the liquid crystal in one direction. To reset the liquid crystal the electric field is removed and the liquid crystal molecules relax to their original orientation. This is slow compared to the speed when driven by an electric field and limits the speed of nematic liquid crystals to typically 40ms for a  $\lambda$  phase shift in the visible. Nematic liquid crystal can be considered as a waveplate with a variable retardance.

The response of the liquid crystal to an applied electric field is non-linear. Figure 2.6 shows the response of the liquid crystal against potential difference across the cell. The vertical axis shows the change in phase shift (in arbitrary units) of light passing through the cell. There is a certain threshold voltage,  $V_{th}$ , below which there is no response. This is important for multiplexing SLMs (see Chapter 4).

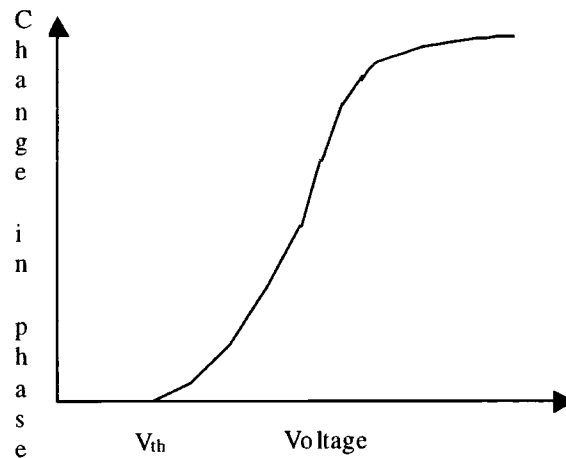


*Figure 2.6. A typical voltage response curve of nematic liquid crystal.  $V_{th}$  is the threshold voltage. The exact units will depend upon the liquid crystal material and the cell thickness.*

If the incident light is polarised in the orthogonal direction to the extraordinary axis it will not experience any of  $n_e$ , so there will be no difference in the phase of the light that passes through the liquid crystal if there is or is not an electric field applied.

### 2.3.5 PHASE SHIFTING BY FERROELECTRIC LIQUID CRYSTALS

Ferroelectric liquid crystal (FLC) SLMs use smectic  $C^*$  liquid crystals. If the cell containing the liquid crystal is made thin enough, the interaction with the surface causes the rotation of the director from layer to layer to be suppressed (see figures 2.7 and 2.8). The type of liquid crystal used in these SLMs prefer to align their directors parallel to the glass substrates (see figure 2.9). The molecules also possess a permanent electric dipole moment. A phase with a permanent dipole in the absence of an electric field is called a ferroelectric phase, so this cell is called a surface stabilised ferroelectric liquid crystal (SSFLC or just FLC). Two states are possible and are shown in figure 2.9. The molecules are arranged in layers and these are in the plane of the page. The director is in the plane of the glass cell but pointing at some *tilt angle* (usually  $22.5^\circ$ ) to the normal of the page. The

electric polarisation is aligned perpendicular to the director and is in the plane of the page. By changing the polarity of the applied electric field the molecules rotate round. Looking through the cell, this has the effect of rotating the director by twice the tilt angle. This is called the *switching angle*. This is effectively an electronically rotatable waveplate. By suitable configuration of polarisers, the FLC SLM can be made to produce either phase modulation or amplitude modulation.

Because the molecules possess a permanent dipole moment and can be driven in both directions they have a very fast switching time compared to nematic liquid crystals,  $\sim 100\mu\text{s}$ . However, they only have two possible states. The commercially available Displaytech 10x10B FLC has a frame rate of 4000Hz. Switching speeds as high as 10MHz have been demonstrated (Liu, 1993).

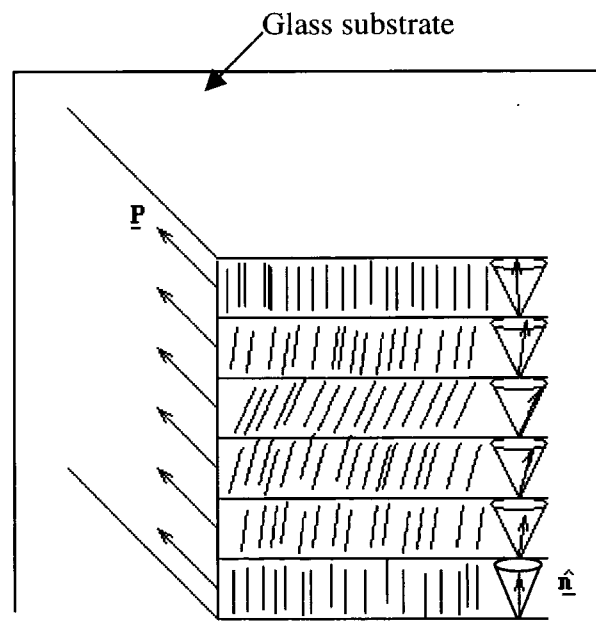
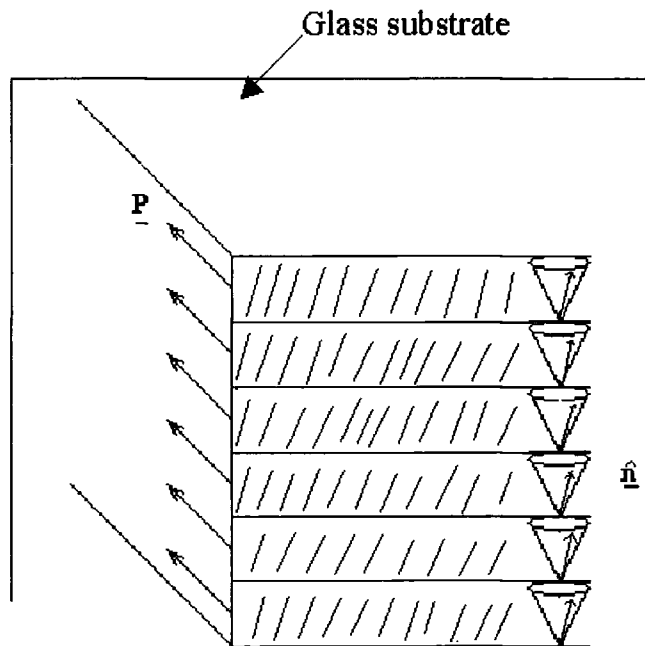


Figure 2.7. The director in Smectic C\* rotates from layer to layer when the liquid crystal is not stabilised by the glass substrate.  $\underline{P}$  is the direction of electric dipole moment.  $\hat{n}$  is the direction of the liquid crystals director.



*Figure 2.8. The director in Smectic C\* does not rotate from layer to layer when the cell is made thin enough. The glass substrate inhibits the rotation and the material becomes 'surface stabilised.'*

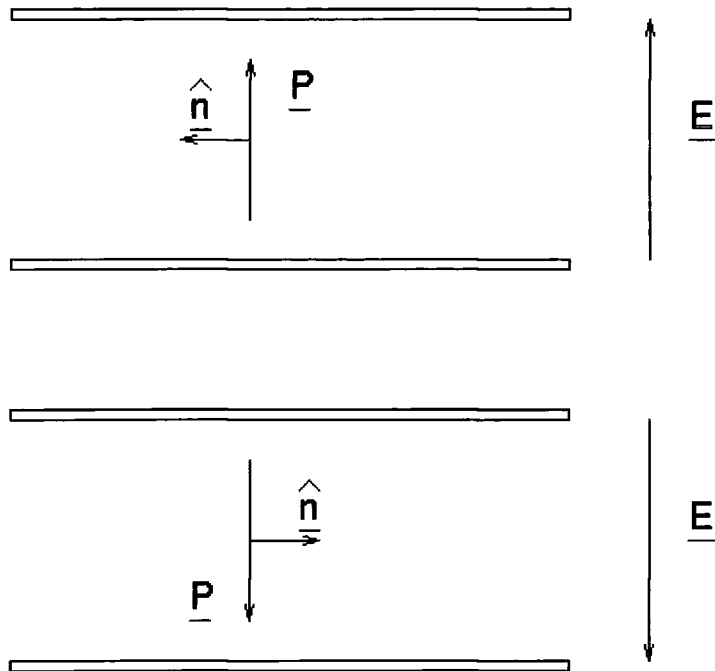


Figure 2.9 The SSFLC. The layers of smectic molecules are in the plane of the page. The director,  $\hat{n}$ , is shown as its projection onto the plane of the page. It is at an angle of  $22.5^\circ$  to the perpendicular of the page's plane. The application of an electric field causes the switching between the two states.

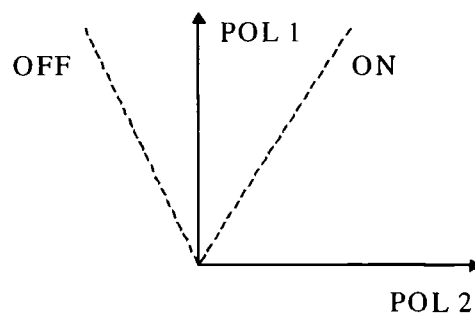


Figure 2.10. The alignment of the input and output polarisers with reference to the switching angle of the FLC needed to attain a phase shift of  $\pi$  when the retardance of the device is not  $\pi$  and the switching angle is not  $90^\circ$ . POL 1 is the input polariser and POL 2 is the output polariser. ON and OFF represent the two optical axes of the FLC.

As discussed above, FLCs are birefringent and produce a phase shift by an electrically controlled rotation of the optical axis. The device needs to be placed between two crossed polarisers, where the axis of the first bisects the two optical axes states of the FLC (see figure 2.10).

The retardance,  $\Gamma$ , of the FLC is given by

$$\Gamma = \frac{2\pi d}{\lambda} \Delta n \quad [2.4]$$

where  $d$  is the thickness of the FLC,  $\lambda$  the wavelength of light, and  $\Delta n$  the birefringence of the liquid crystal.

The phase shift produced by the FLC can be calculated using Jones calculus. There is often an absolute phase term,  $e^{i\phi}$ , in the Jones matrices. Since we are not interested in the absolute phase, only the difference between the on and off states of the FLC, this is dropped to simplify the mathematics.

The FLC can be considered as a retarder with its optical axis at angle  $\theta$  (the tilt angle) to the vertical. The FLC is then represented by  $\mathbf{W}$

$$\mathbf{W} = \begin{bmatrix} e^{-i\Gamma/2} \cos^2 \theta + e^{i\Gamma/2} \sin^2 \theta & e^{-i\Gamma/2} \sin \theta \cos \theta - e^{i\Gamma/2} \sin \theta \cos \theta \\ e^{-i\Gamma/2} \sin \theta \cos \theta - e^{i\Gamma/2} \sin \theta \cos \theta & e^{-i\Gamma/2} \sin^2 \theta + e^{i\Gamma/2} \cos^2 \theta \end{bmatrix} \quad [2.5]$$

The incident light is vertically polarised and represented by  $\mathbf{V}$

$$\mathbf{V} = \begin{bmatrix} 0 \\ 1 \end{bmatrix} \quad [2.6]$$

and the output polariser is,  $\mathbf{P}$

$$\mathbf{P} = \begin{bmatrix} 1 & 0 \\ 0 & 0 \end{bmatrix} \quad [2.7]$$

The transmitted amplitude,  $\mathbf{T}$ , is then given by

$$\mathbf{T} = \mathbf{P}\mathbf{W}\mathbf{V} \quad [2.8]$$

$$= \begin{bmatrix} e^{-i\Gamma/2} \cos\theta \sin\theta - e^{i\Gamma/2} \cos\theta \sin\theta \\ 0 \end{bmatrix} \quad [2.9]$$

for the Displaytech FLC used in this thesis,  $\Gamma=0.6\pi$  and the tilt angle,  $\theta$ , is  $\pm 22.5^\circ$ .

$$\Rightarrow \mathbf{T} = -0.572 \cdot \begin{bmatrix} e^{\pm i\frac{\pi}{2}} \\ 0 \end{bmatrix} \quad [2.10]$$

So we have a phase shift of  $\pm\pi/2$  with an amplitude of 0.572. The  $\pm$  refers to the device in either its 'on' or 'off' mode. So switching from 'on' to 'off', a change in phase of  $\pi$  is introduced. The transmission is measured in terms of intensity and is  $|0.572|^2 = 33\%$ .

### 2.3.6 FLC OPERATED WITH NO POLARISERS

If we consider the case of an ideal FLC SLM the retardance would be  $\pi$  radians and the switching angle  $90^\circ$ . In this case no polariser would be needed in the system. We can consider unpolarised light as the superposition of two incoherent linearly polarised beams.

For  $\Gamma = \pi$  and  $\theta = \pm 45^\circ$ , equation [2.5] becomes

$$\mathbf{W} = \begin{bmatrix} 0 & \pm i \\ \pm i & 0 \end{bmatrix} \quad [2.11]$$

If we first consider the vertical component of the incident light,  $\mathbf{V}$ , we get

$$\mathbf{T}_V = \mathbf{WV} \quad [2.12]$$

$$= \begin{bmatrix} e^{\pm i \frac{\pi}{2}} \\ 0 \end{bmatrix} \quad [2.13]$$

The Jones's matrix for horizontally polarised light,  $\mathbf{H}$ , is

$$\mathbf{H} = \begin{bmatrix} 1 \\ 0 \end{bmatrix} \quad [2.14]$$

so

$$\mathbf{T}_H = \mathbf{WH} \quad [2.15]$$

$$= \begin{bmatrix} 0 \\ e^{\pm i \frac{\pi}{2}} \end{bmatrix} \quad [2.16]$$

The FLC rotates the polarisation of the light by  $90^\circ$  (as expected for a half waveplate with the incident light at  $45^\circ$ ). There is still a phase shift of  $\pi$  radians between the two states.

An alternative method of improving the transmission has been proposed by Neil and Paige (Neil, 1994) using the FLC with a quarter wave plate and a mirror in the system. The system still requires a polariser but the transmission is increased. Warr *et. al.* (Warr, 1995) increased the throughput of their system by using no polarisers with a non-ideal FLC. This left a large DC peak in their diffraction pattern for a  $0/\pi$  grating. To the author's knowledge, there has not yet been any assessment of using imperfect FLCs in an adaptive optics system.

## **2.4 Applications of liquid crystal SLMs**

The most common applications of liquid crystal SLMs are displays. These are usually based upon a slightly modified type of nematic liquid crystal device called a *twisted nematic liquid crystal* (TNLC). This was invented in the late 1970's and has revolutionised many display applications. A twisted nematic cell is made by sandwiching nematic liquid crystal between two glass plates. The glass plates have rubbing directions<sup>1</sup>  $90^\circ$  to each other. This causes a gradual rotation of the director through the cell in a helical structure (see figure 2.11). Linearly polarised light entering the cell is rotated by this helix and an output polariser is placed after the cell  $90^\circ$  to the polarisation of the incident light. This gives the maximum transmission. When an electric field is applied to the cell, the molecules realign and there is no longer any rotation of the director through the cell, and hence no rotation of the polarisation. This gives extinction of light.

---

<sup>1</sup>The "rubbing direction" is the direction in which the director aligns. It can be made by rubbing a polymer alignment layer on the glass with a piece of cloth in one direction or by a placing a chemical deposit on the glass surface.

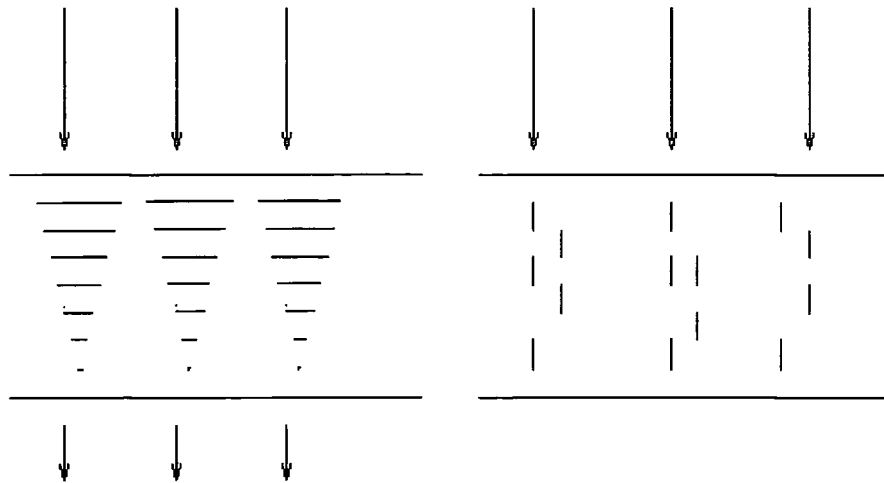


*Figure 2.11. A twisted nematic display. Light enters at the top through a polariser. When there is no electric field the molecules rotate the plane of polarisation by  $90^\circ$  and it passes through the second polariser that is orthogonal to the first. When an electric field is applied there is no rotation and hence no transmission of light.*

Colour displays are created by having either dyes in the liquid crystals or coloured filters. These produce colour images in a similar way to TVs by having red, green and blue pixels.

Problems caused by addressing large numbers of pixels have been tackled in recent years by incorporating *thin film transistors* (TFT) and other electronics into the displays to act as switches for the pixels. Another alternative is to build the SLM on a silicon back plane which also acts as the control electronics (for a review see (Clark, 1994) and (Johnson, 1993)).

FLCs are not as commonly used in displays. To generate a grey scale temporal multiplexing is used (Landreth, 1992), i.e., to get a 100 grey levels each picture frame is divided, temporally, into 100 sub-frames. To get a 25% grey level the pixel is switched on for 25 sub-frames and off for 75 sub-frames. The eye integrates this making the pixel appear grey. These devices can be made to be

very small, with a resolution in excess of 500 lines per inch (Worboys, 1993) and are used in applications such as helmet mounted displays.

Both phase modulators and intensity modulators have been constructed using *optically addressed liquid crystal SLMs* (OASLM) or *liquid crystal light valves* (LCLV) (Efron, 1985 & Moddel, 1987). The liquid crystal is placed onto a photoconductive layer. The resistance of the layer is dependent on the amount of light incident on it. This alters the electric field across the liquid crystal cell, and either gives amplitude or phase modulation (Johnson, 1990) depending upon the optical configuration of the device. By a suitable choice of photoconductor the device can be used to convert infrared images into visible images.

All of the devices in this thesis are driven electronically. This is achieved by either *direct drive* or *multiplexing*. Direct drive SLMs have an electrode connected to each individual pixel. When there is a large number of pixels, it becomes difficult to individually connect each pixel. Instead, the pixels are multiplexed. The pixels are activated by selecting the correct row and column.

## 2.4.1 MULTIPLEXING THEORY

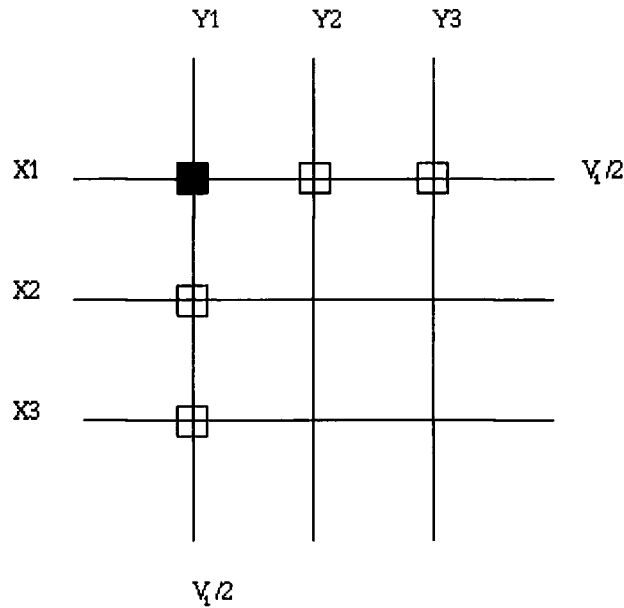


Figure 2.12. An example of a pixel driven by multiplexing. The dark square represents a fully activated pixel and the clear squares partially activated pixels.

The multiplexing driving method is designed to reduce the number of electrical connections required by a liquid crystal SLM with a large number of pixels. Consider an array of nine pixels, as shown in figure 2.12. The nine pixels are connected with three lines in the horizontal direction (X1, X2 and X3) and three lines in the vertical (Y1, Y2 and Y3). If we wished to activate pixel (1, 1) with a voltage  $V_1$  we would set row X1 to voltage  $V_1/2$  and column Y1 to  $-V_1/2$ , thus giving a potential difference of  $V_1$  across pixel (1,1). However, pixels (1,2), (1,3), (2,1), and (3,1) will also have a potential difference of  $\pm V_1/2$  across them. In the ideal case,  $V_1/2$  will be below the threshold voltage of the liquid crystal and so it will not be activated in any way. If this is not the case, crosstalk will occur. In liquid crystal displays this manifests itself as contrast reduction.

For a large number of pixels, it is too slow to access each pixel individually so instead of the “dot sequential addressing” described above, “line dumping addressing” is used. In this case, if for example, we wanted to address pixels

(1,1), (1,3), row X1 would be set to  $V_1/2$  and both columns Y1 and Y3 set to  $-V_1/2$ . Then row X2 would be set to  $V_1/2$  and the appropriate voltage placed on the columns we would wish to activate. The rows are known as the *common* and the columns as either the *segments* or simply *columns*. For a large display, such as the GEC 64x64 which will be used in chapter 4, the waveforms being applied to the liquid crystal become very complex (see (Hitachi, 1991) for more details). This method still has the same crosstalk problem as the dot sequential address technique.

## **2.5 Summary**

This chapter has covered the basics of liquid crystal theory. The two types of liquid crystal, nematic and FLC, that are to be used in this thesis have been described. The effects of an electric field and the effects the liquid crystal molecules have on light have been described. The next chapter will give a brief review of atmospheric turbulence and conventional adaptive optics.

## Chapter 3: Atmospheric Turbulence and Conventional Adaptive Optics

### 3.1 Introduction

In the previous chapter, the essential characteristics of liquid crystals were described. In this chapter, there will be a review of conventional adaptive optics and the causes of atmospheric turbulence. Adaptive optics in non-astronomical applications and other sources of aberrations that potentially require adaptive optics are discussed.

#### 3.1.1 THE FUNCTION OF AN ASTRONOMICAL TELESCOPE AND HISTORY OF ADAPTIVE OPTICS

The purpose of an imaging telescope is to collect as much celestial radiation as possible and focus this into an image with the highest resolution as possible. The diameter of the telescope is the fundamental limit of both of these. The light gathering power is dictated by the collecting area of the primary mirror. The resolution of any optical imaging device is limited by diffraction. The so called Rayleigh criterion defined when two points, separated by an angle  $\theta_R$ , can be resolved, is given by

$$\theta_R = 1.22 \frac{\lambda}{D} \quad [3.1]$$

where  $D$  is the diameter of the imaging device, in this case the diameter of the telescope's aperture, and  $\lambda$  is the wavelength of the incident light.

Increasing  $D$  increases the resolution of the telescope. However, turbulence in the Earth's atmosphere limits the resolution to about 1'' which is equivalent to  $D \approx 10\text{-}20\text{cm}$  in the visible. This was noticed as far back as Newton, (Newton, 1704) who in his book *Opticks* could see no possible solution to the problem:

*“If the Theory of making Telescopes could at length be fully brought into Practice, yet there would be certain Bounds beyond which Telescopes could not perform. For the Air through which we look upon the Stars, is in a perpetual Tremor; as may be seen by the tremulous Motion of Shadows cast from high Towers, and by the twinkling of the fix’d Stars. But these Stars do not twinkle when viewed through Telescopes which have large apertures. For the Rays of Light which pass through divers parts of the aperture, tremble each of them apart, and by means of their various and sometimes contrary Tremors, fall at one and the same time upon different points of the Eye, and their trembling Motions are quick and confused to be perceived severally. And all these illuminated Points constitute one broad lucid Point, composed of those many trembling Points confusedly and insensibly mixed with one another by very short and swift Tremors, and thereby cause the Star to appear broader than it is, and without any trembling of the whole...*

*The only Remedy is a most serene and quiet Air, such as may perhaps be found on the tops of the highest Mountains above the grosser Clouds.”*

In 1953 Babcock (Babcock, 1953) first proposed using what is now called *adaptive optics* to compensate for the atmosphere and restore the resolution to the diffraction limit

*“If we had a means of continually measuring the deviation of rays from all parts of the mirror, and of amplifying and feeding back this information so as to correct locally the figure of the mirror to the schlieren pattern, we could expect to compensate both for the seeing and any inherent imperfections of optical figure.”*

Babcock’s attempts to implement his idea were thwarted by the technology limitations of the time. Adaptive optics was neglected until the 1970’s when, the

idea was resurrected with limited success (Buffington, 1976; Buffington, 1977; Hardy, 1976). A large input to adaptive optics technology occurred at the end of the cold war when US military adaptive optics systems became de-classified. These systems were designed for observing satellites, as well as focusing laser beam direct energy weapons as part of the strategic defence initiative (SDI) or “*Star Wars.*”

In 1989 one of the first civilian astronomical adaptive optics system was constructed called COME-ON. This provided correction for a small telescope (Rousset, 1990) and later a 3.6m telescope (Rigaut, 1991). Since then a number of other systems have been constructed. The upsurge in interest has come about because of an improvement in wavefront sensing technology; a shift into the infra-red as the wavelength of interest where the aberrations are easier to correct; and the use of laser guide stars (Foy, 1985).

### **3.1.2 TERMINOLOGY**

It is important to distinguish between adaptive optics and the closely related field of active optics. Adaptive optics is used to compensate for rapidly varying aberrations ( $>\approx 10\text{Hz}$ ), whilst active optics is used to correct for deformations in the actual telescope. These deformations can arise from thermal expansions, mechanical strains, etc. in the telescope’s optics and structure. They typically have a frequency of  $<1\text{Hz}$ . Active optics sometimes uses the telescope’s primary mirror as a deformable mirror such as in the ESO-NTT and the 10 metre Keck telescope. Adaptive optics usually uses a small deformable mirror.

If a system employs any feedback it will be called *closed loop*. If there is no feedback it will be called *open loop*.

### 3.2 Wavefront Distortions Caused by the Atmosphere

The Earth's atmosphere is approximately 20km thick. At sea level the atmospheric pressure is approximately  $10^5$ Pa and tends towards zero as height is increased. The change in pressure effects the refractive index of the air. This is 1.0003 at sea levels and tends toward unity with height. As the sun rises and sets, turbulence is created in the atmosphere. This comes from the differences in the heating rates of the Earth's different surfaces (such as water, soil, and rock) causing convection currents which mix with air of different regions causing eddies. This turbulence is in several layers. If the turbulence were absent, incident light with a plane wave would propagate through the atmosphere unaberrated. However, the turbulence causes changes in pressure and hence refractive index. These changes in refractive index cause the optical path length of light passing through to change (see figure 3.1). Although the changes in refractive index are small, the fact that light passes through several kilometres of air means that the change in path length is of the order of micrometres when it reaches the Earth's surface.

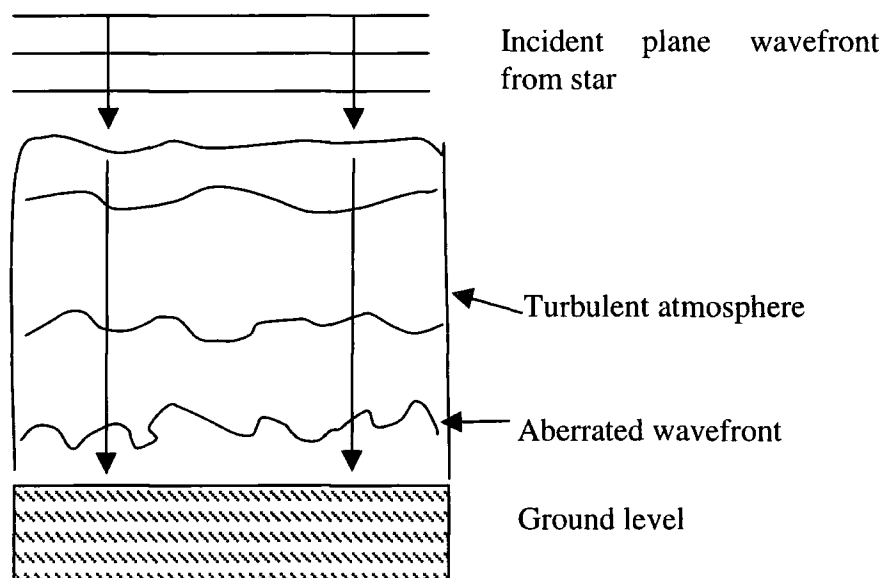


*Figure 3.1. As the plane wavefront from the star enters the atmosphere, it becomes aberrated.*

The atmosphere can be characterised by eddy sizes. For the Kolmogorov model of turbulence the largest eddies, of size  $L$  (the *upper turbulence scale*), contain smaller eddies. The smaller eddies are produced by the larger eddies transferring energy into smaller and smaller eddies. The smallest eddy size is  $l$ , the *lower turbulence scale*. The size of  $l$  is of the order of a few millimetres and is set by molecular friction between air molecules. The upper turbulence scale is set by the size of the atmosphere and the surrounding geography. There is substantial disagreement over the size of  $L$ . It ranges from a few metres to several kilometres (Beckers, 1992). It is likely that the size of  $L$  varies from one telescope location to another.

The propagation of light through the atmosphere can not be easily modelled. The effects are too complex for any numerical or deterministic predictions so statistical analysis is used.

Kolmogorov (Kolmogorov, 1961) studied the statistical rms velocity differences between two points in the atmosphere. From this, a velocity structure function can be derived. This can be related to the phase structure function which is more relevant and is defined as the mean squared phase difference between all points in the wavefront which are distance  $r$  apart, that is,

$$D_{\phi}(r) = \langle [\phi(r'+r) - \phi(r')]^2 \rangle \quad [3.2]$$

where  $\phi$  is phase,  $r$  and  $r+r'$  are positions. It was shown that (Fried, 1965b)

$$D_{\phi}(r) = 6.88 \cdot \left( \frac{r}{r_0} \right)^{5/3} \text{rad}^2 \quad [3.3]$$

where  $r_0$ , the coherence length, is a normalising scale. [3.3] is valid over the range

$$l < r < L \quad [3.4]$$

Fried's coherence length,  $r_0$ , is an important parameter in adaptive optics; it is a measure of the severity of the atmospheric turbulence. Fried found that the maximum diameter of a telescope before atmospheric turbulence limited the performance is given by (Fried, 1965a)

$$r_0 = \left[ 0.423 k^2 \sec(\beta) \int_0^\xi C_n^2(h) dh \right]^{-3/5} \quad [3.5]$$

where  $\xi$  is the total path length through the atmosphere,  $\beta$  is the zenith angle,  $h$  is the height,  $C_n^2(h)$  is known as the refractive index structure constant and  $k=2\pi/\lambda$ , where  $\lambda$  is wavelength. This is a measure of the strength of the turbulence.  $C_n^2(h)$  varies with height, geographical location and time (with a period of hours). There is no accurate model of  $C_n^2(h)$  at present although several authors have developed approximate models (Hufnagel, 1974; Ulrich, 1988). If however,  $C_n^2(h)$  is approximated to a constant and  $\beta=0$ , it can be related to  $r_0$  via

$$r_0 = 1.68 \left( C_n^2 \xi \left( \frac{2\pi}{\lambda} \right)^2 \right)^{-3/5} \quad [3.6]$$

$r_0$  can also be defined as the diameter of an aperture over which the wavefront phase variance is equal to 1 radians<sup>2</sup>.

In this thesis  $r_0$  will be taken at  $\beta=0^\circ$  and  $\lambda=0.5\mu\text{m}$  unless otherwise stated. With these parameters it equals approximately 10 - 20cm. This means that, with no correction for the atmospheric turbulence, the 10 metre Keck telescope has the same resolution as a 10cm telescope. The atmosphere limits the Keck telescope to a 100<sup>th</sup> of its diffraction performance.

### 3.2.1 INTENSITY VARIATIONS

As Sir Isaac Newton pointed out (see §3.1.1) intensity variations, or scintillations, can be seen with the naked eye as star twinkling. In a telescope with a larger aperture, this effect is averaged out and it becomes of secondary importance. There has been little study of intensity variations for adaptive optics and it is usually ignored. It has been suggested that intensity correction may be required to image extra-solar planetary systems where the brightness of the scintillations of the stars drown out the planet orbiting its barycentre. Love and Gourlay (Love, 1996) describe a method using liquid crystals to do this. For large telescopes, the phase aberrations are of more importance.

### 3.2.2 TEMPORAL VARIATIONS

The rate of change of the wavefront distortion depends predominantly upon the wind velocity. Since the wind is moving with different velocities (magnitude and direction) depending upon height, a typical value for  $v_w$  is hard to define. It is usually taken to be between 5 and 20ms<sup>-1</sup>.

For a closed loop system to correct turbulence Greenwood (Greenwood, 1977) calculated the system must work at frequency of  $f_0$  or higher.  $f_0$  is known as the Greenwood frequency and is given by

$$f_0 = \frac{0.4 v_w}{\sqrt{\lambda \xi}} \quad [3.7]$$

### 3.2.3 TEMPORAL POWER SPECTRUM

The temporal power spectrum of atmospheric turbulence is given by (Conan, 1995)

$$F_{\phi}(f) \propto C_n^2 \frac{dh}{v_w} \left( \frac{f}{v_w} \right)^{-8/3} \quad [3.8]$$

where  $f$  is the frequency and the atmosphere has been approximated to a single rigid layer. This model is not valid as  $f$  tends towards zero.

### 3.2.4 WAVELENGTH DEPENDENCE OF ATMOSPHERIC TURBULENCE

It can be seen from [3.5] that  $r_0$ , and hence atmospheric turbulence, has a wavelength dependence ( $r_0 \propto \lambda^{6/5}$ ). In the visible,  $r_0$  is approximately 10-20cm but this increases with increasing wavelength. Table 3.1 shows typical values for  $r_0$  and  $f_0$  for various wavelengths.

Wavelength / $\mu\text{m}$	$r_0$ /cm	$f_0$ /Hz
0.5	20	28
1.6	81	16
2.2	118	13
5.0	317	9

*Table 3.1. Typical values for  $r_0$  and  $f_0$  at various wavelengths. The values chosen for [3.7] were  $v_w=5\text{ms}^{-1}$  and  $\xi=10\text{km}$ . The wavelengths chosen are viable transmission windows in the atmosphere.*

Because of the increase in  $r_0$  and decrease in  $f_0$  with  $\lambda$ , it is easier to construct an adaptive optics system that works in the infrared.

### 3.2.5 ZERNIKE MODES AND THE REPRESENTATION OF THE SPATIAL DISTORTIONS OF THE WAVEFRONTS

It is often useful to describe the phase aberrations in the atmosphere in terms of Zernike polynomials,  $Z_j(\rho, \theta)$ , where  $j$  denotes the  $j^{\text{th}}$  polynomial,  $\rho$  is the radial co-ordinate in units of the aperture radius, and  $\theta$  is the angular co-ordinate. Zernike polynomials are an orthogonal set of basis functions that can be used to describe monochromatic aberrations found in optics. The phase aberration is then

$$\phi(\rho, \theta) = \sum_{j=1}^{\infty} a_j Z_j(\rho, \theta) \quad [3.9]$$

where  $a_j$  is the amplitude of the  $j^{\text{th}}$  Zernike mode.

The polynomials were originally used to describe the aberrations in standard optics where most of the aberrations occur towards the edge. The means that to describe the atmosphere, where the aberrations are not at the edge of the telescope but uniformly spread over the whole aperture, a large number of terms are required. However, most of the power is contained in the low order modes.

The individual polynomials can be derived from an expansion of

$$Z_{\text{even } j}(\rho, \theta) = \sqrt{n+1} R_n^m(\rho) \sqrt{2} \cos(m\theta) \quad m \neq 0 \quad [3.10]$$

$$Z_{\text{odd } j}(\rho, \theta) = \sqrt{n+1} R_n^m(\rho) \sqrt{2} \sin(m\theta) \quad m \neq 0 \quad [3.11]$$

$$Z_j(\rho, \theta) = \sqrt{n+1} R_n^0(\rho) \quad m = 0 \quad [3.12]$$

where

$$R_n^m(\rho) = \sum_{s=0}^{\frac{n-m}{2}} \frac{(-1)^s (n-s)!}{s! \left[ \left( \frac{n+m}{2} - s \right)! \right] \left[ \left( \frac{n-m}{2} - s \right)! \right]} \rho^{n-2s} \quad [3.13]$$

$n$  and  $m$  are integers,  $m \leq n$  and  $n-|m| = \text{even}$ .  $j$  is the mode ordering number and is a function of  $n$  and  $m$ . The first few terms are shown in table 3.2.

Depending upon the exact definition of  $j$  the order of the Zernike polynomials changes from author to author. In this thesis  $Z_8$  is spherical aberration and the modes for  $m=3, n=3$  come after this.

Azimuthal frequency m			
Radial Degree n	0	1	2
0	$Z_0=1$ Piston		
1		$Z_1=2\rho\cos(\theta)$ $Z_2=2\rho\sin(\theta)$ Tip/tilt	
2	$Z_3 = \sqrt{3}(2\rho^2 - 1)$ Defocus		$Z_4 = \sqrt{6}\rho^2 \sin(2\theta)$ $Z_5 = \sqrt{6}\rho^2 \cos(2\theta)$ Astigmatism
3		$Z_6 = \sqrt{8}(3\rho^3 - 2\rho)\sin(\theta)$ $Z_7 = \sqrt{8}(3\rho^3 - 2\rho)\cos(\theta)$ Coma	
4	$Z_8 = \sqrt{5}(6\rho^4 - 6\rho^2 + 1)$ Spherical		

Table 3.2. Zernike polynomials

For the  $j^{\text{th}}$  mode corrected by an adaptive optics system, Noll (Noll, 1976) calculated the residual variance,  $\sigma^2$ , and these are shown in table 3.3.

Mode	Residual Error /radians <sup>2</sup>
0	$1.0299(D/r_0)^{5/3}$
1	$0.582(D/r_0)^{5/3}$
2	$0.134(D/r_0)^{5/3}$ Tip/tilt removed
3	$0.111(D/r_0)^{5/3}$ Defocus removed
4	$0.0880(D/r_0)^{5/3}$
5	$0.0648(D/r_0)^{5/3}$ Astigmatism removed
6	$0.0587(D/r_0)^{5/3}$
7	$0.0525(D/r_0)^{5/3}$ Coma removed
8	$0.0463(D/r_0)^{5/3}$ Spherical removed

Table 3.3 Residual wavefront errors after correction of Zernike modes. Mode 0 is the wavefront error before correction.

For a large  $j$

$$\sigma^2 \approx 0.2944 j^{-\sqrt{3}/2} \left( \frac{D}{r_0} \right)^{5/3} \quad [3.14]$$

From table 3.3 and equation [3.14] it is clear that most of the turbulence power is concentrated in the first few modes.

In this thesis, the Strehl ratio is defined as the ratio of the peak intensity of the image of a point source to the peak intensity of the diffraction limited image of the same point source. For a  $\sigma^2 \ll 1$  it can be approximated to

$$SR = e^{-\sigma^2} \quad [3.15]$$

### 3.3 Conventional Adaptive Optics

#### 3.3.1 THE NEED FOR ADAPTIVE OPTICS

The need for adaptive optics can be seen when the imaging of an object,  $O(x,y)$ , is imaged through the atmosphere's instantaneous phase function  $\phi(x,y)$ . The complex amplitude of the atmosphere function is

$$A(x, y) = A_0 e^{i\phi(x,y)} \quad [3.16]$$

where  $A_0$  is the modulus of amplitude (and is assumed to be constant here). The point spread function is then the square modulus of the Fourier transform (FT) of  $A$

$$P(p, q) = |FT(A(x, y))|^2 \quad [3.17]$$

$p$  and  $q$  are the spatial frequency co-ordinates. The intensity in the image plane is then

$$I(p, q) = O(p, q) \otimes P(p, q) \quad [3.18]$$

$$= FT(FT(O(p, q)) \cdot FT(P(p, q))) \quad [3.19]$$

where  $\otimes$  indicates the convolution operator.

Because the intensity is the square of the modulus of the complex amplitude information about the phase is lost and so the atmospheric phase function can not be determined from the intensity pattern alone.

### 3.3.2 PHASE CONJUGATION

Conventional and liquid crystal adaptive optics, both use the principle of phase conjugation to perform the correction of the aberrated wavefront. If we consider an incident wavefront with a phase error of  $\sigma$  that has been introduced by the atmosphere, then the wavefront is represented by

$$ae^{-i\sigma} \quad [3.20]$$

where  $a$  is the amplitude. If the conjugate of the phase,  $e^{+i\sigma}$ , is multiplied by [3.20] the phase error is now zero. This phase conjugate is applied to the wavefront by changing the optical path length through which the light travels. This can be by either deforming a mirror or, for example, by using liquid crystals. Using a deformable mirror is the conventional method in adaptive optics. In order to apply the phase conjugate it is necessary to have a wavefront sensor to measure the phase error.

### 3.4 Deformable Mirrors

Corrective elements for modern telescopes usually fall into two groups of deformable mirrors (DMs):

- Segmented mirrors such as MARTINI (Doel, 1990), ELECTRA (Buscher, 1997)
- Continuous face plate mirrors such as COME-ON (Rigaut, 1991)

The simplest design is the piston only segmented mirror. Each mirror segment is driven with one degree of freedom, usually by piezo-electric crystals. The more complex variety have 3 degrees of freedom: piston, tip and tilt. These mirrors more closely fit the incident wavefront. Both types suffer from diffraction and energy loss caused by the gaps between each mirror segment.

Continuous face plate mirrors consist of a continuous deformable mirror placed over driving actuators. There are several different methods of driving such a mirror:

1. Discrete positional actuators. Piezo-electric crystals are placed behind the mirror and push or pull the mirror into the desired shape.
2. Discrete force actuators. These are like the discrete positional actuators but a non-contact force such as an electric field drives the mirror.
3. Bimorph mirrors. A sheet of piezo-electric crystal is bonded to the rear of the mirror. Application of an electric field causes the piezo-electric sheet to bend.
4. Micro-mirrors. These mirrors are semiconductor devices. They are manufactured by etching a silicon wafer. They are similar to type 2 above but are only ~1cm across. To the author's knowledge they have not yet been implemented in an astronomical adaptive optics system.

Although there is no optical power loss because there are no segmented elements causing diffraction and absorption, these mirrors have a complex *influence function* when an actuator deforms the mirror. This needs to be accurately measured. They are also more difficult to maintain than segmented mirrors where a damaged section can easily be replaced.

Most types of DM are driven by piezo-electric crystals. These require large voltages ( $\approx 500\text{V}$ ) to drive them and consume a lot of power (except in the case of micro mirrors). This makes the drive electronics difficult to design and introduces an unwanted heating effect inside the telescope. The heating effect can act as a source of aberrations.

### 3.5 Wavefront Sensors

Adaptive optics requires a measurement of the wavefront aberration in order to apply the conjugate to the phase error. There are two basic methods: *direct* or *indirect* wavefront sensing.

Indirect wavefront sensors make no explicit measure of the phase but use some other measure that is related to it such as image sharpness (Muller, 1974). It is possible to use a trial and error method with the corrector. Examples are hill climbing, evolutionary programming and genetic algorithms. In these cases random variations are introduced into the corrective element by various methods (see (Fogel, 1994) and (Srinivas, 1994) for an overview of evolutionary programming and genetic algorithms). The use of such techniques has not yet been fully addressed for adaptive optics although similar work has been done using these techniques to design diffractive optical elements (Yoshikawa, 1997). The major drawback is that it can take several hundred *generations* of solutions to reach the optimum. The measurement of how well the device is correcting can be assessed, for example, by measuring the peak intensity of the corrected image.

In *multi-dithering* techniques, the corrective elements track a temporally varying phase delay (O'Meara, 1977). This requires the corrective element to sweep through its range, to maximise the intensity of the image, faster than the turbulence. By filtering out the high frequency sweeps, the corrector can be made to follow the time varying phase variations and keep the image intensity at a maximum.

*Image sharpening* techniques monitor some sharpness criteria in the image (Muller, 1974). They usually vary the phase shift of the corrective element to maximise this criterion. Because of the high speed required for both image sharpening and multi-dithering they both suffer from limited bandwidth and limited photons forming the image.

### **3.5.1 DIRECT SENSING AND INTERFEROMETERS**

Direct wavefront sensing techniques will be used in the work of this thesis. These techniques are usually either interferometric or tilt/focus sensing. One of the simplest interferometers is the Michelson interferometer. This type of interferometer requires the aberrated beam to be interfered with an unaberrated reference beam. This means that the aberration has to be placed inside an arm of the interferometer and so it can not be used for atmospheric measurements.

A modified type is the shearing interferometer. This is based upon a Mach-Zehnder interferometer with one mirror slightly tilted. Tyson (Tyson, 1991) gives a detailed analysis of how shearing interferometers work. Self-referencing interferometers offer an alternative. An example of such a device is the point diffraction interferometer that will be used in chapter 5 and the theory behind it is covered next.

### **3.5.2 THE SMARTT OR POINT DIFFRACTION INTERFEROMETER**

The Point Diffraction Interferometer (PDI) is from a class of interferometers called common path interferometers. Unlike a Michelson interferometer, where a separate unaberrated beam is interfered with the test beam, the PDI uses part of the test beam to generate its own reference beam.

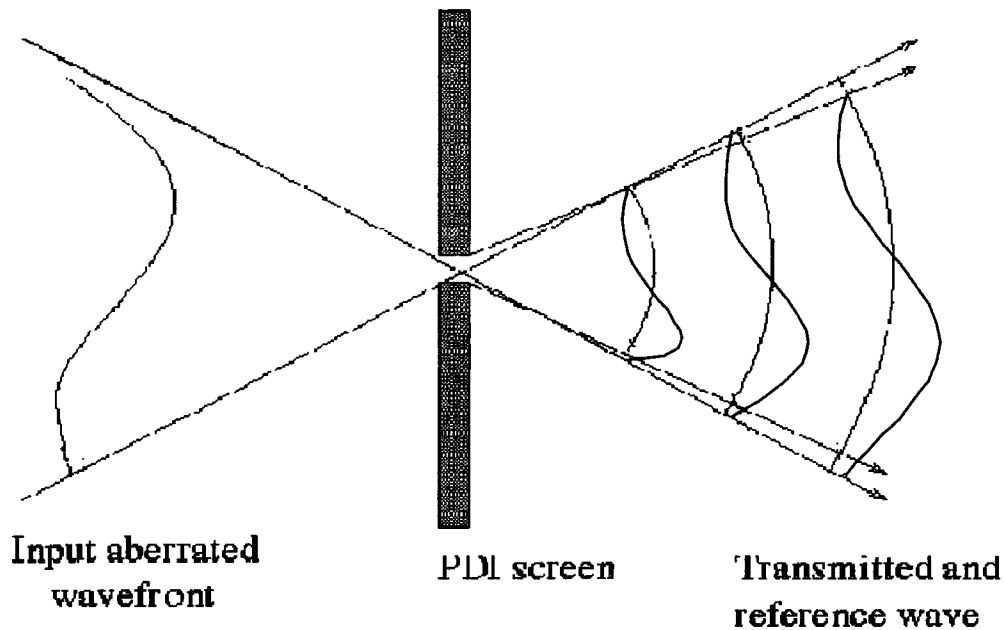


*Figure 3.2. A detail of the PDI aperture. The incident light is focused on to the pinhole with a lens. The zeroth order light passes through the pinhole creating a reference beam for the higher orders to interfere with.*

The basic design is shown in figure 3.2. The device is similar to a spatial filter. Incident light is focused onto a semitransparent mask. The mask consists of a transparent pinhole, about the size of the Airy disk of the beam, and this is surrounded by a semitransparent screen (transmission  $\sim 0.1\%$ ). A lens behind the mask images the resultant interferogram onto a camera. The light from the zeroth order passes through the pinhole. This has no high frequencies and so produces an unaberrated beam. The rest of the light that passed through the semitransparent screen now interferes with the unaberrated beam.

### **3.6 The Shack-Hartmann Wavefront Sensor**

A Shack-Hartmann wavefront sensor is another type of direct sensor. It consists of an array of lenses (or *lenslets*) focused onto a CCD camera. The local tilt of the wavefront across each of the lens subapertures can be determined from the position of the image on the CCD camera.

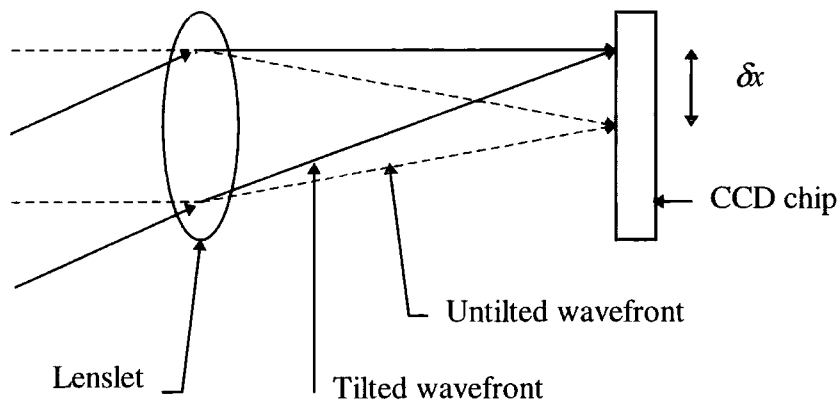


*Figure 3.3. A single lenslet of the Shack-Hartmann array. An unaberrated beam is represented by the dotted line. The beam with a tilt across it is represented by the solid line. The amount of tilt can be calculated from  $\delta x$ , the displacement of the spot on the CCD chip.*

Consider one lenslet (see figure 3.3). When there is no aberration in the incident beam, the focus will be exactly on axis with the centre of lens. When a tilt is introduced the spot will move off axis. From the measurement of the change in position, the tilt of the wavefront over the lenslet can be calculated. Any Zernike wavefront aberration can be approximated to a set of discrete tilts. By sampling the wavefront with an array of lenslets, all of these tilts can be measured and the complete wavefront calculated from this. Because the positions of the spots on the CCD camera do not change with the piston term of the wavefront, this term can not be measured. Fortunately, global piston is generally not important in adaptive optics.

### 3.6.1 SPOT CENTROIDING

To find the centre of the spots on the CCD camera a simple algorithm is used. In one dimension, if  $I_n$  is the intensity at pixel  $n$ , the position of the spot,  $P$ , is given by

$$P = \frac{\sum_{n=1}^m I_n \cdot n}{\sum_{n=1}^m I_n} \quad [3.21]$$

over  $m$  pixels. The CCD camera image is divided up into a number of search squares. The centre of each square corresponds to the unaberrated spot position of a lenslet. The position of each spot is calculated and the deviation from the centre stored in an array. [3.21] is prone to error in low signal to noise situations. A high background noise will cause  $P$  to tend towards the edge of the search square. The signal to noise ratio in a laboratory can be quite high if a laser is used as the light source, minimising this source of error. In a situation with a lower signal to noise ratio this algorithm would have to be modified. A simple thresholding of all the data improves the accuracy of the system.

### 3.6.2 MODES FROM TILTS - THE INTERACTION MATRIX

The basis functions to be used in this thesis are Zernike polynomials. The total number of modes that can be used is limited to  $J$ , so the phase,  $\phi(x,y)$ , at point  $x,y$  is approximated to

$$\phi(x, y) = \sum_{j=1}^J a_j Z_j(x, y) \quad [3.22]$$

$j$  is the mode number and  $a_j$  is Zernike mode amplitude. The Shack-Hartmann measures  $M$  spot positions at various discrete points  $m$ . The spot centroiding algorithm provides the positions of  $m$  in the  $x$  direction and the  $y$  direction. The tilt across each aperture is given by

$$\left. \frac{\partial \phi}{\partial x} \right|_m = \sum_{j=1}^J a_j \left. \frac{\partial Z_j(x_m, y_m)}{\partial x} \right|_m \quad [3.23]$$

$$\left. \frac{\partial \phi}{\partial y} \right|_m = \sum_{j=1}^J a_j \left. \frac{\partial Z_j(x_m, y_m)}{\partial y} \right|_m \quad [3.24]$$

We can represent [3.23] and [3.24] for all  $m$  with a matrix.

$$\mathbf{s} = \mathbf{B}\mathbf{a} \quad [3.25]$$

where

$$\mathbf{s} = \begin{pmatrix} \left. \frac{\partial \phi}{\partial x} \right|_1 \\ \left. \frac{\partial \phi}{\partial x} \right|_2 \\ \vdots \\ \left. \frac{\partial \phi}{\partial x} \right|_M \\ \left. \frac{\partial \phi}{\partial y} \right|_1 \\ \left. \frac{\partial \phi}{\partial y} \right|_2 \\ \vdots \\ \left. \frac{\partial \phi}{\partial y} \right|_M \end{pmatrix} \quad [3.26]$$

$$\mathbf{a} = \begin{pmatrix} a_1 \\ a_2 \\ a_3 \\ \vdots \\ a_J \end{pmatrix} \quad [3.27]$$

and

$$\mathbf{B} = \begin{pmatrix} \left. \frac{\partial Z(x, y)_1}{\partial x} \right|_1 & \left. \frac{\partial Z(x, y)_2}{\partial x} \right|_1 & \dots & \left. \frac{\partial Z(x, y)_j}{\partial x} \right|_1 \\ \left. \frac{\partial Z(x, y)_1}{\partial x} \right|_2 & \left. \frac{\partial Z(x, y)_2}{\partial x} \right|_2 & \dots & \left. \frac{\partial Z(x, y)_j}{\partial x} \right|_2 \\ \vdots & \vdots & & \vdots \\ \left. \frac{\partial Z(x, y)_1}{\partial x} \right|_M & \left. \frac{\partial Z(x, y)_2}{\partial x} \right|_M & \dots & \left. \frac{\partial Z(x, y)_j}{\partial x} \right|_M \\ \left. \frac{\partial Z(x, y)_1}{\partial y} \right|_1 & \left. \frac{\partial Z(x, y)_2}{\partial y} \right|_1 & \dots & \left. \frac{\partial Z(x, y)_j}{\partial y} \right|_1 \\ \vdots & \vdots & & \vdots \\ \left. \frac{\partial Z(x, y)_1}{\partial y} \right|_M & \left. \frac{\partial Z(x, y)_2}{\partial y} \right|_M & \dots & \left. \frac{\partial Z(x, y)_j}{\partial y} \right|_M \end{pmatrix} \quad [3.28]$$

$\mathbf{B}$  can be calculated off line by calculating the differential for each mode in each axis for all of the theoretical spot centres. The actual values of element of  $\mathbf{B}$  depend upon the size and shape of the lenslet array.

The amplitudes of the Zernike modes can be calculated by rearranging [3.25] with the pseudoinverse of  $\mathbf{B}$ .

$$\mathbf{a} = \left[ (\mathbf{B}^T \mathbf{B})^{-1} \mathbf{B}^T \right] \mathbf{s} \quad [3.29]$$

The T indicates the matrix transpose. The pseudoinverse of  $\mathbf{B}$  is also calculated off line.

### 3.6.3 WAVEFRONT CURVATURE

Wavefront curvature sensors are similar in nature to Shack-Hartmann wavefront sensors except they measure the defocus of a wavefront instead of tilt. Two measurements of the image are taken, one each axial side of the lens's focus. By comparing the intensities of the two images, the defocus can be calculated. Again see Tyson (Tyson, 1991) for a full description. These devices are best

used with continuous face plate mirrors because the deformation of the mirror closely matches the response of the sensor.

### **3.7 Binary Adaptive Optics**

Binary (or half-wave) adaptive optics offers a simpler alternative to conventional adaptive optics. Binary adaptive optics was first proposed by Kim *et al.* (Kim, 1988) for correcting the distortions introduced into the optical system by the SLM itself. They were using an LCTV as a phase-only SLM to write binary holograms. The LCTV was not optically flat so they added a binary phase pattern to the hologram to partially remove the aberration introduced. A Mach-Zehnder interferometer was used as the wavefront sensor. This was also later repeated by Tam *et al.* (Tam, 1990) who used a PDI as their wavefront sensor. This system also used LCTVs. The draw back with these systems was that LCTVs are based upon nematic liquid crystals that are slower than FLCs, and both systems only attempt to correct for static aberrations. The idea of binary adaptive optics was later re-invented by Love *et al.* (Love, 1993 & 1995) who proposed using a FLC SLM as the corrective element in a real-time adaptive optics system. Love's theoretical models were for an atmospheric adaptive optics system using a FLC SLM.

#### **3.7.1 BINARY ADAPTIVE OPTICS THEORY**

When a plane wavefront, sampled by a circular aperture, is focused the resulting intensity pattern, the PSF, is the well-known Airy disk. When the plane wavefront becomes aberrated, say by passing through the atmosphere, the PSF is no longer a perfect Airy disk. Destructive interference reduces the PSF peak intensity and spreads the light out thereby blurring the image. The concept behind binary adaptive optics correction is not to completely flatten out the wavefront to its original form, as in conventional adaptive optics, but to merely add half a wave to any part of the light that is out of phase. This reduces the

amount of light destructively interfering at the focus and thus partially corrects the PSF.

The algorithm for binary correction is simple:

*When the wavefronts error (modulus  $\lambda$ ) is greater than half a wavelength apply a wavefront correction of half a wave.*

FLCs are well suited to binary adaptive optics because of their bistable nature. It has been shown by Love *et al.* (Love, 1995) that despite only partially correcting the wavefront an increase in the Strehl ratio from ~0% to 40.5% is achievable.

### **3.7.2 BINARY ADAPTIVE OPTICS AND HIGHER ORDER CORRECTION WITH FLCs**

Unless several devices are cascaded together in an optical system, it is currently only possible to achieve a two state or bistable SLM with FLCs. With the suitable configuration of polarisers, FLCs can act as amplitude or phase modulators. We are only interested in phase modulation at present.

The two states required for binary adaptive optics are  $-\pi/2$  and  $\pi/2$ , which is equivalent to saying  $0/\pi$  phase shift because we are not interested in the absolute phase (nor can it be determined). Up to four cascaded devices have been demonstrated by (Biernacki, 1991), (Freeman, 1992) and (Broomfield, 1995a&b), giving phase shifts of  $0$ ,  $\pi/8$ ,  $\pi/4$ ,  $3\pi/8$ ,  $\pi/2$ ,  $5\pi/8$ ,  $3\pi/4$ , and  $7\pi/8$ . Because polarisers need to be incorporated around each device, the transmission of such a system is prohibitively low (Broomfield quotes a 16dB loss).

### **3.8 Non-Astronomical Adaptive Optics Applications**

Non-conventional Earth based non-astronomical applications for adaptive optics has so far been limited. This is mainly because of the high cost of such systems. There are the possibilities of many more applications. Some of these are summarised below. Liquid crystals offer the potential for low cost adaptive optics, although they are not suitable for all applications.

- **Space Based Astronomy:** Although still an astronomical application this is included here because it is not an Earth based system and has different requirements. There is some interest in using some sort of adaptive optics in the Next Generation Space Telescope (NGST) and in other future space telescopes (Kuo, 1994). The Hubble space telescope is diffraction limited but it is limited by the relatively small diameter of its primary mirror (2.4m) compared to many Earth based telescopes. Placing a larger conventional mirror into space would be extremely expensive and maybe technically impossible with the current fleet of Space Shuttles. Some of the current NGST designs use a primary mirror that folds out like an umbrella. These mirrors are generally lower quality and so some sort of adaptive optics will need to be incorporated into the system to compensate for this. There is the potential of using liquid crystal SLMs for this application. Their lightweight and robustness makes them potentially suitable for space applications. The system would be an *active* optics system, so the liquid crystals slow speed would not be a disadvantage.
- **Military Applications:** A large part of the early work on adaptive optics was done by the US military as part of the Strategic Defence Initiative. These systems were for ground based satellite observations and laser weapon beam propagation through the atmosphere.
- **Laser welding:** There is a need to maintain a fine focus of the beam on the surface.

- **Laser Cavity Applications:** An adaptive mirror in a laser cavity echelon can be used to maintain the correct alignment in the cavity. This is important for high power applications where the heating of the laser causes the mirrors to warp. In both this application and the previous, the high power nature would mean the only corrective device that could be used would be a conventional deformable mirror.
- **Under water imaging:** The majority of image degradation when imaging objects under water comes from scattering from particles in the water. Adaptive optics may have some applications when imaging in ultra pure water (e.g. in nuclear power stations).
- **Retinal Scanning:** When imaging the retina, the resolution is approximately that of a cone. To image at finer resolutions adaptive optics will be needed.
- **Optical Storage Devices:** CD based systems already use an adaptive optics system to maintain focus. It is possible in the future that there will be a need to use a complete adaptive system, correcting for several Zernike modes. This may be important in next generation systems, post DVD, where the beam will have to propagate through several layers to reach the desired information, i.e., the information is stored in 3 D.
- **Hostile Environment Imaging:** There is a potential for using adaptive optics in situations where the environment effects the performance of optics such as in furnaces. Furnace walls have to be continuously monitored to ensure there is no soot build up which reduces the heat transfer efficiency. Normal optics will become stressed when exposed to high temperatures; adaptive optics could correct for this.

The following chapters will however concentrate on astronomical applications.

### **3.9 Summary**

In this chapter we have reviewed the sources of aberrations from the atmosphere and conventional adaptive optics. The statistical Kolmogorov structure of atmospheric turbulence has been described. The current state of deformable mirrors and the different types of wavefront sensor have also been reviewed. Some non-astronomical applications of adaptive optics have been mentioned although the application of liquid crystal adaptive optics in this thesis will be towards astronomy.

In the next chapters, the knowledge from the previous two chapters will be used when constructing liquid crystal adaptive optics systems. The next chapter will first study a custom built nematic SLM and the possibilities of using this in adaptive optics.

## **Chapter 4: A Multiplexed Nematic Liquid Crystal SLM**

### ***4.1 Introduction***

In this chapter there will be a description of a purpose built 64x64 pixel nematic liquid crystal SLM. This device was built by GEC, for Durham University and the Defence Evaluation Research Agency (DERA) for a first attempt at liquid crystal adaptive optics. This section describes the device, its calibration, and its performance. Experimental evidence shows there was a major problem when using the device as a phase only SLM because of its drive electronics.

There are at present several methods used for controlling liquid crystal SLMs. These include multiplexing, direct drive, active matrix and optical addressing. Most of the current technological drive behind liquid crystal SLMs is for display applications. In principle, display technology should be easy to convert to phase modulating SLMs. Displays such as LCTVs (liquid crystal televisions) and computer monitors require a large number of pixels. Directly driving each pixel becomes impossible because of the need to have electrodes going to each individual pixel. Multiplexing and active matrix are currently used in large displays. Active matrix displays are currently not suitable to be used as phase only SLMs for adaptive optics because of their very small fill factor (typically can be as low as ~25%). Multiplexing offers a simple driving technique and so this following section sets out to characterise a custom built device.

### ***4.2 Device Description***

The device was based upon standard display technology. It used a 64x64 pixel glass substrate designed for a twisted nematic liquid crystal display. The drive electronics are based around the Hitachi HD61203 dot matrix liquid crystal column driver and the Hitachi HD61203 dot matrix common driver chips. The device was controlled by a Viglen 80386 IBM compatible PC and software

written in Microsoft C. To simplify the device's electronics only the column voltage could be altered, all the row voltages were identical so in effect the device only worked in one dimension. To control the device an array of voltages was sent to the computer's *digital to analogue converter* (DAC) where this was converted into a serial signal. This signal was amplified and converted back into a digital signal by the liquid crystal drive electronics and fed into the two Hitachi liquid crystal driver chips (see figure 4.1).

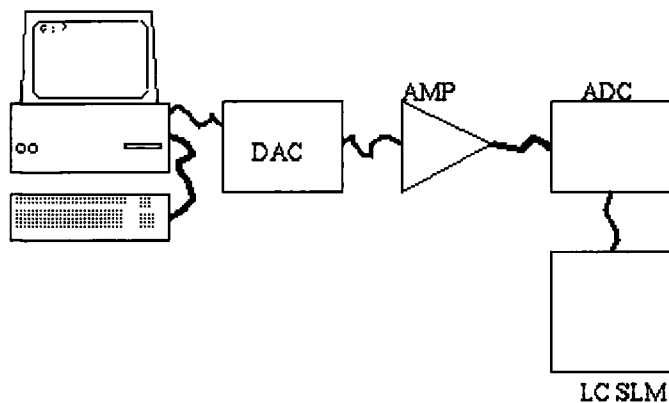


*Figure 4.1. The 64x64 SLM's drive electronics block diagram.*

The liquid crystal used in the device was E7 produced by Merck (formerly BDH Ltd.). The main difference between this device and commercially available devices was that the liquid crystal was not twisted nematic, but parallel aligned. This enables phase modulation of light without any rotation of its polarisation state. The device specifications are given in table 4.1.

Specification	Value
Liquid crystal	Merck E7
Threshold voltage	1.50V
Birefringence	$\Delta n=0.22$
Cell thickness	25 $\mu\text{m}$
Controllable optical path length	5.5 $\mu\text{m}$
Total theoretical retardance	$\sim 7\lambda^1$
Theoretical resolution	7 bit, $\sim \lambda/18^2$
Pixel size	400 $\mu\text{m}$
Inter-pixel spacing	40 $\mu\text{m}$
Pixel fill factor	90%
RMS optical flatness (Love, 1994)	$\lambda/2^3$
Effective number of pixels	64x1
Pixel refresh rate	15ms <sup>4</sup>
Operating temperature	-10°C to +60.5°C
Response time , for $\lambda/2$ decay (Purvis, 1993)	40ms <sup>5</sup>

Table 4.1. The specifications of the 64x64 SLM

Although this device is limited in only being able to be driven in one dimension, it is still useful to assess the capabilities of a multiplexed driven liquid crystal SLMs for adaptive optics. Multiplexed liquid crystal displays suffer from low contrast. A similar problem occurs in phase-only modulation. An experiment was set up to investigate this and to calibrate the liquid crystal for phase versus voltage applied. The contrast reduction is because of voltage “*crosstalk*”

<sup>1</sup> $\lambda=638.2\text{nm}$  He-Ne

<sup>2</sup> $\lambda=638.2\text{nm}$  He-Ne. This assumes that the response is uniform over the whole dynamic range, which it is not.

<sup>3</sup>Measured with a Zygo interferometer, 638.2nm He-Ne

<sup>4</sup>This is the speed at which the drive electronics refreshes the SLM. The actual liquid crystal does not work at this speed, to relax from  $7\lambda$  to  $0\lambda$  phase shift took several seconds

<sup>5</sup> $\lambda=543\text{nm}$  He-Ne

between pixels with high applied voltage and pixels with a lower applied voltage.

### **4.3 Experimental**

#### **4.3.1 VOLTAGE WAVEFORM MEASUREMENTS**

The exact voltages being applied to the liquid crystal were investigated. Three wires were soldered onto the electrical connections of the liquid crystal array on columns 22 and 42, and row 32. These were then connected to a cathode ray oscilloscope (CRO). The voltage waveform applied to the liquid crystal could be measured. By subtracting the voltage waveform from either column 22 or 42 from that of row 32, the potential difference applied across pixels (32,22) or (32,42) could be measured. Several different voltage waveforms were recorded: completely off, completely on, half the array on and half the array off, and a ramp function across the whole array. The individual traces being applied to each particular row and column were also recorded.

#### **4.3.2 PHASE SHIFT MEASUREMENTS**

In order to quantify the crosstalk, the actual phase shifts were measured. It was assumed that if all of the pixels had the same voltage applied, there would be no crosstalk between them. Using this assumption a calibration curve for phase shift versus voltage could be measured.

Nematic liquid crystals are birefringent and so can be treated as normal linear waveplates but with a variable retardance. When placed between crossed polarisers, at an angle that bisects the extraordinary and ordinary axis, the SLM modulates intensity. Using this, the phase shift can be measured indirectly. When there is a phase shift of  $(2n+1)\pi$  the transmitted intensity is at a maximum, and a minimum when the phase shift is  $2n\pi$ , where  $n=0,1,2,\dots$ . It was assumed that the retardance of the liquid crystal would always decrease with increased potential across the liquid crystal.

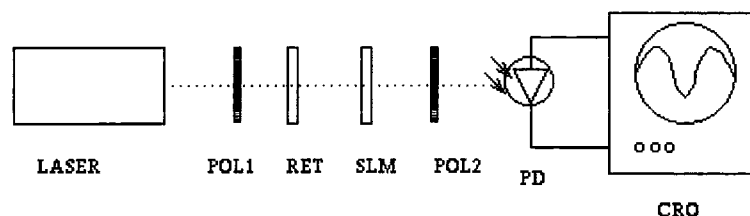


*Figure 4.2. The experimental set-up to measure the phase shift induced by the 64x64 SLM. POL1 and POL2 are both polarisers at  $45^\circ$  and  $135^\circ$  respectively compared to the optical axis of the SLM, RET is a liquid crystal retarder, SLM is the 64x64 SLM, PD is a photodiode which measures the transmitted intensity, and CRO is an oscilloscope.*

The experimental set-up is shown in figure 4.2. An additional liquid crystal cell retarder was required and the voltage across it was altered until there was a minimum transmission. This was necessary because the retardance of the GEC 64x64 in its 'off state' was not necessarily  $n\pi$ , where  $n$  is an integer. The light source was a 5mW 638.2nm He-Ne laser.

A calibration curve for the SLM was calculated by increasing the voltage applied across the liquid crystal and recording the minimum and maximum intensity throughput against voltage.

Once the device was calibrated, the crosstalk could be measured. A fixed voltage was applied to one half of the device (columns 1-32) whilst the other half (33-64) had its voltage varied. First of all a voltage that should have induced a  $\pi$  phase shift according to the calibration curve was imposed on columns 1-32. The phase shift produced by columns 33-64 was measured as before. This was repeated for the voltages equivalent to all possible integer values of  $\pi$  phase shift on columns 1-32. If there was no crosstalk between the two halves, the new phase/voltage curves generated for columns 33-64 should be identical to the calibration curve.

Next, a known phase shift was imposed on columns 1-32 and the voltage was increased on columns 33-64 while measuring the phase shift on columns 1-32. If there was no crosstalk there should be no change in the phase shift of columns 1-32.

### 4.3.3 VOLTAGE MEASUREMENTS RESULTS

Figures 4.3 to 4.10 show photographs of oscilloscope traces showing the voltages applied to the individual pixels. Note the oscilloscope was set to 5ms per division on the time base and 5V per division on the y deflection.

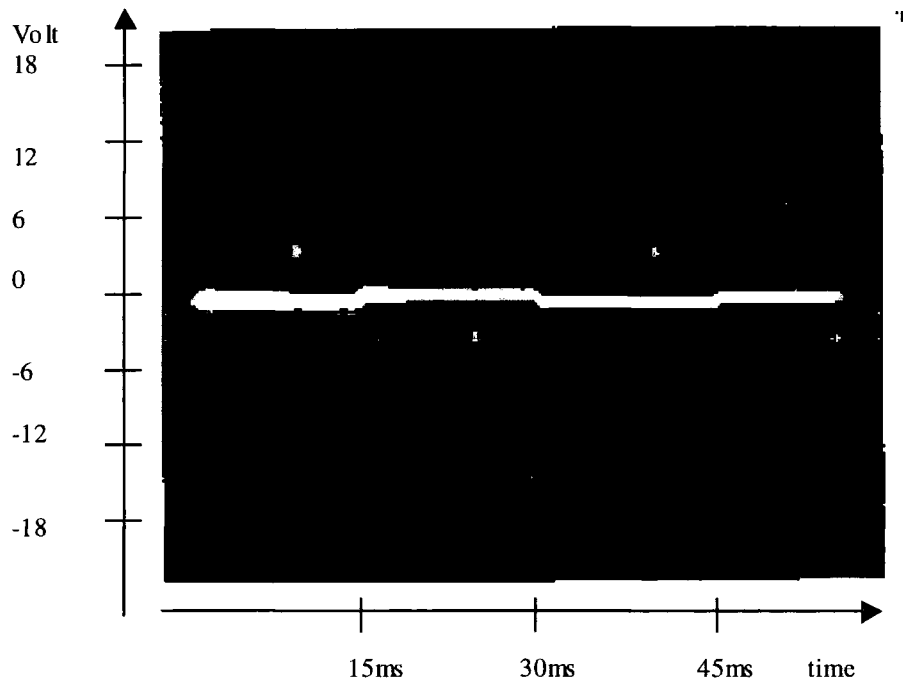


*Figure 4.3. CRO trace showing the voltage across an individual pixel (32,42) of the SLM in the off state. The square wave has an amplitude of -0.1V to -0.5V and the spikes are at 3.8V and -3.6V. The period is 30ms. Note the spikes are the writing pulses and these correspond to the position of the column that is being measured.*

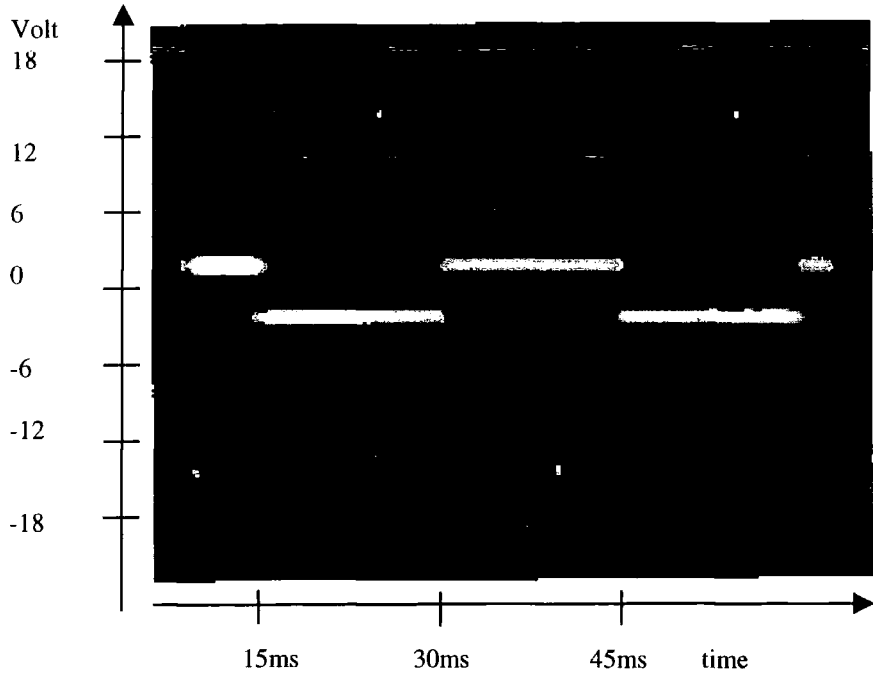


Figure 4.4. CRO trace showing the voltage across an individual pixel when the whole device is switched fully on. The square wave is  $\pm 2V$  and the spikes (only seen as dots on this plot) are  $\pm 15V$ . The period is 30ms.

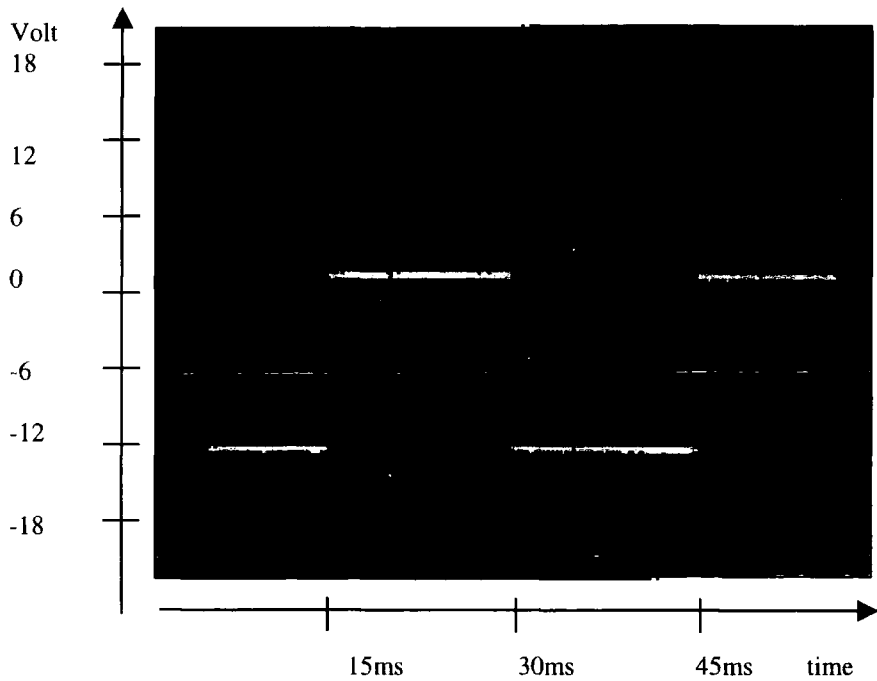


Figure 4.5. CRO trace showing the voltage applied to a pixel's column electrode. The device is switched fully on. The square wave is +2.1V to -13V, the spikes are +4V and -15V, and the period is 30ms.

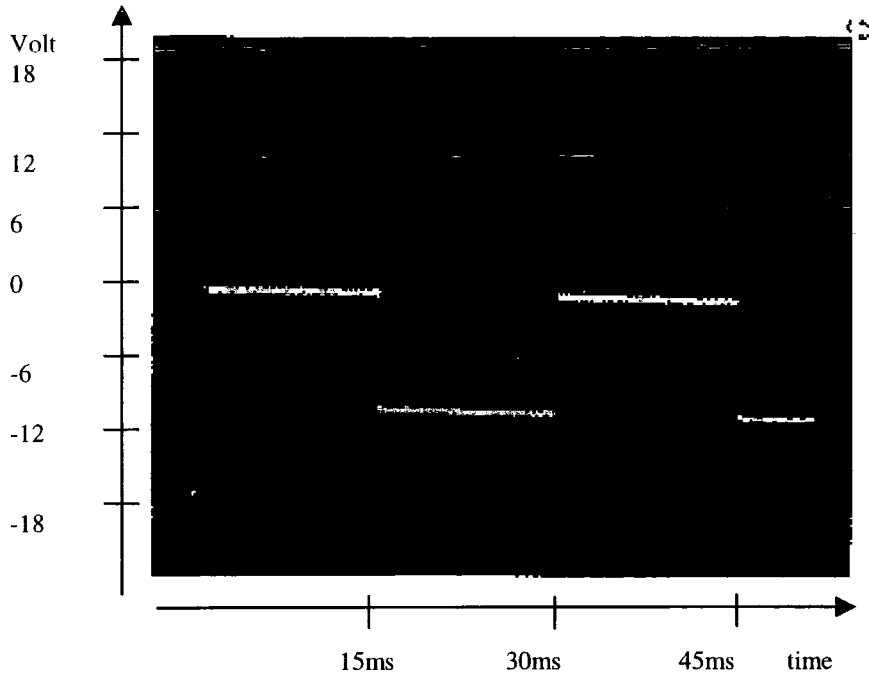


Figure 4.6. The same as figure 4.5 but showing the row voltage only (row 32).

The square wave is 0V to -11V. Note that there are no spikes on this plot.

Subtracting figure 4.5 gives us figure 4.4.

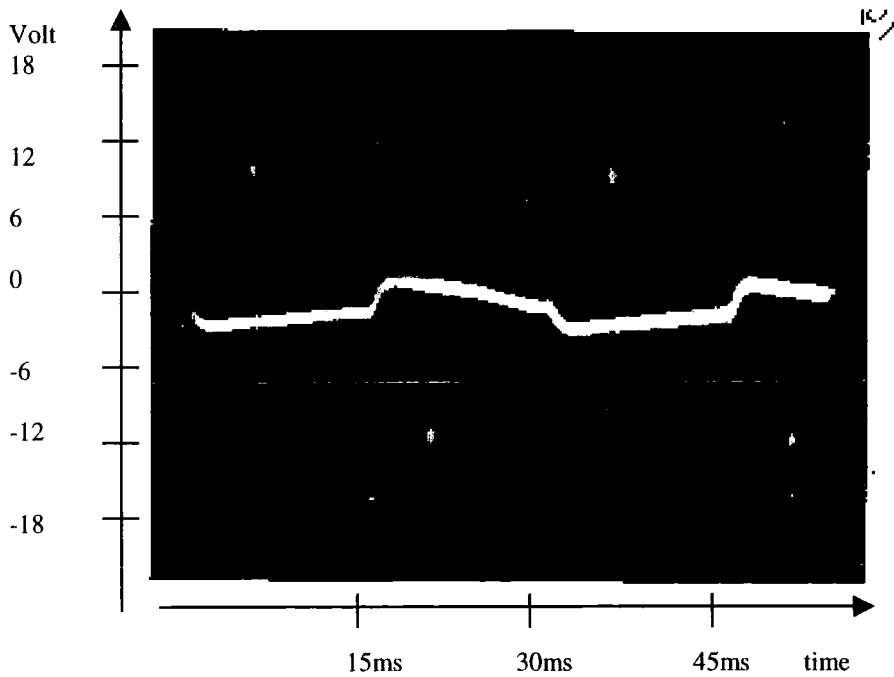


Figure 4.7. CRO trace showing the voltage across pixel (32,22) with a ramp function applied across the whole array. The ramp goes from 0V to  $\pm 2V$  and the spikes are +10.9V and -11V. The waveform is an image of what has been applied to the whole array.

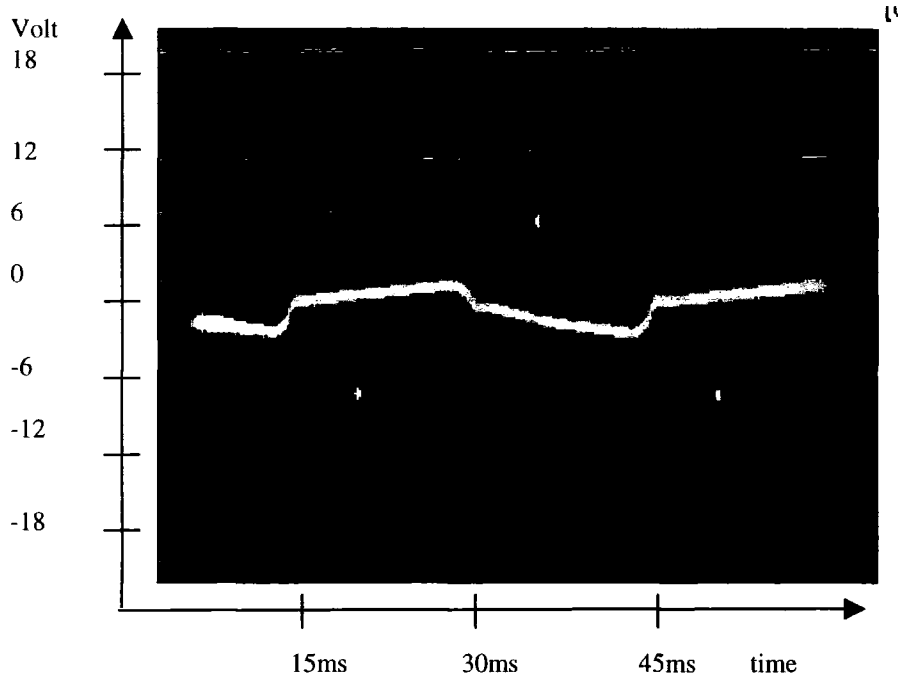


Figure 4.8. The same as figure 4.7 but measured from pixel (32,42). The spikes now have values +6.9V and -7.0V. The spike's position corresponds to the position of the column that is been measured.

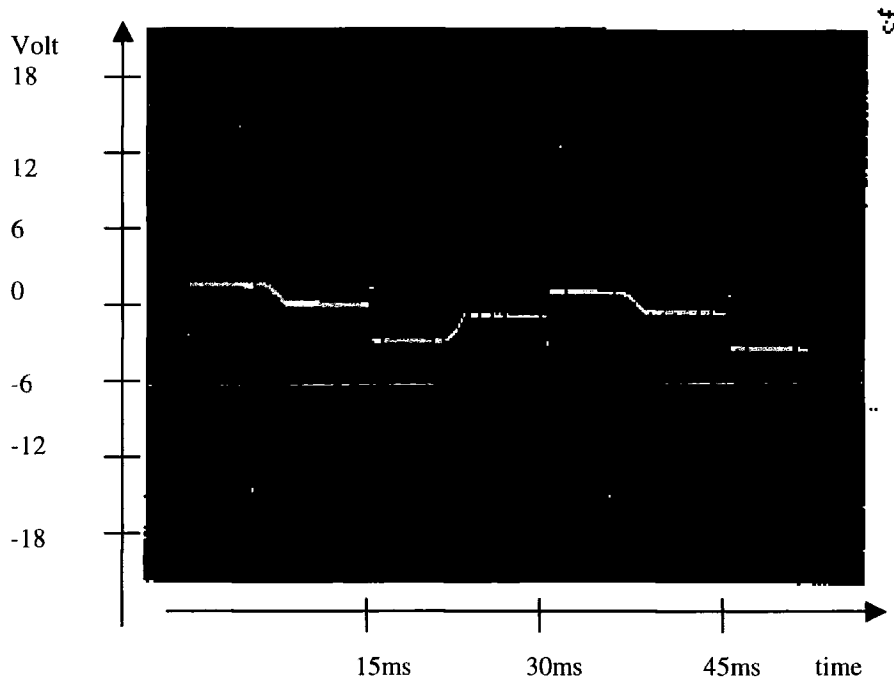
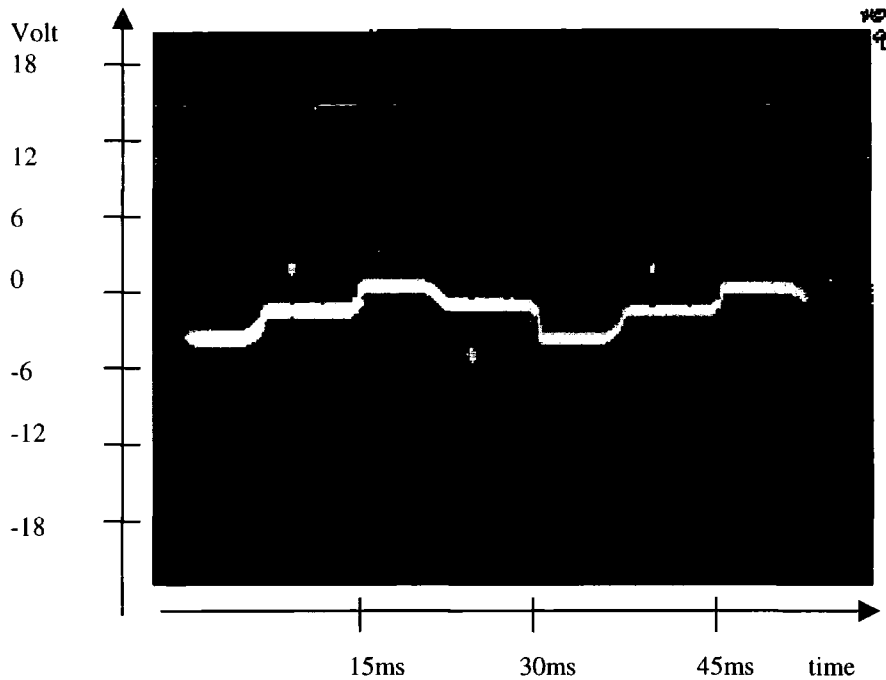


Figure 4.9. CRO trace showing the voltage measured from pixel (32,22). A step function is been applied to the SLM. Columns 1-32 are fully on and columns 33-64 are off. The waveform goes from +2V to -0.1V to -2.2V to -0.2V. The spikes are +15V and -15V.



*Figure 4.10. The same as figure 4.9 but measured from (32,42). The waveform is identical but the spikes are at  $\pm 3.8V$ .*

The figures show how the device was been driven. The position of the spikes on the column waveforms correspond to the position of the pixels being driven. They are only on the column voltages because this is the signal channel whilst the row is the scan. The waveform seen was a result of multiplexing, it was a scaled down image of the actual voltage function applied across the whole array.

The 30ms period of the traces was expected. The frame rate of the device was known to be 15ms. The liquid crystal is driven in AC so one frame is positive and the next is negative giving a total of 30ms. The spikes are also present when the device has 0V applied across it (figure 4.3).

In conclusion, it can be seen from figures 4.3 to 4.10 that the device was being driven by a complex waveform. There was a writing spike corresponding to the driven pixel and a large underlying waveform that was produced by the

multiplexing. The effect this waveform has on the liquid crystal will be discussed in §4.4.4. The next section will show the results of the phase shift measurement experiment.

#### 4.3.4 PHASE SHIFT MEASUREMENT RESULTS

The calibration curve is shown in figure 4.11. The y axis is the value of the spike voltage applied to the liquid crystal. It can be seen that there is a  $14\pi$  phase shift when the device is turned from fully on to off. This compares well to the theoretical total phase shift mentioned in table 4.1.

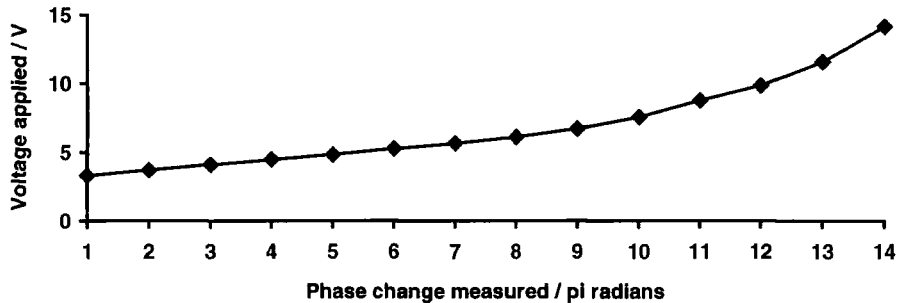


*Figure 4.11. The calibration graph of the nematic liquid crystal SLM.*

Figure 4.12 demonstrates crosstalk. It shows the phase change measured on columns 33-64, whilst the applied voltage on columns 1-32 was kept constant. The y axis shows the expected phase shift and the x axis shows the measured phase shift. If there was no crosstalk between the two halves of the SLM the lines will be identical to the calibration curve.

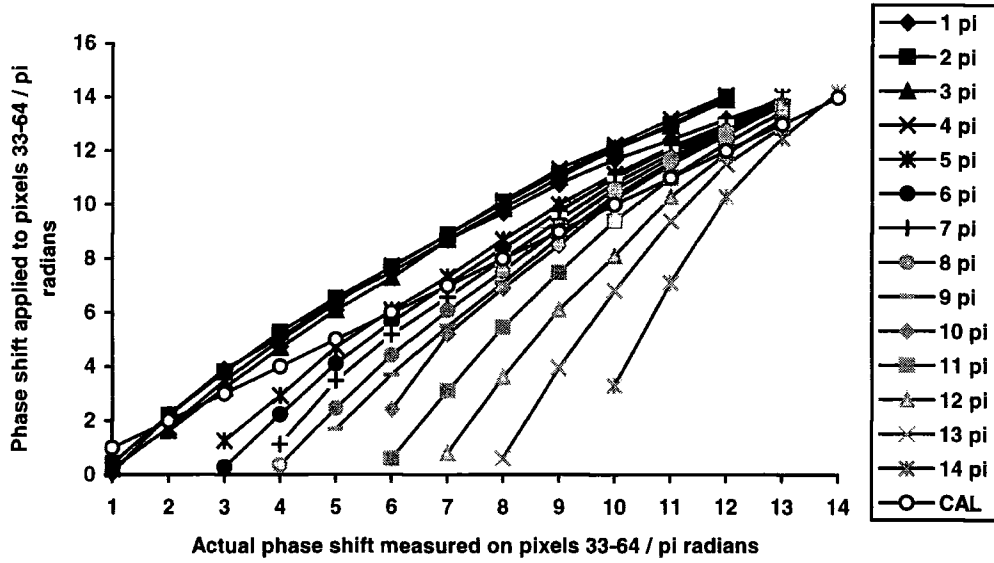


Figure 4.12. This shows the measured phase shifts produced in columns 33-64 of the SLM. A fixed phase shift is applied to columns 1-32 (see the legend). The graph shows the expected phase shift on the vertical axis versus the measured phase shift on the horizontal axis. The calibration line (CAL in legend) is also shown.

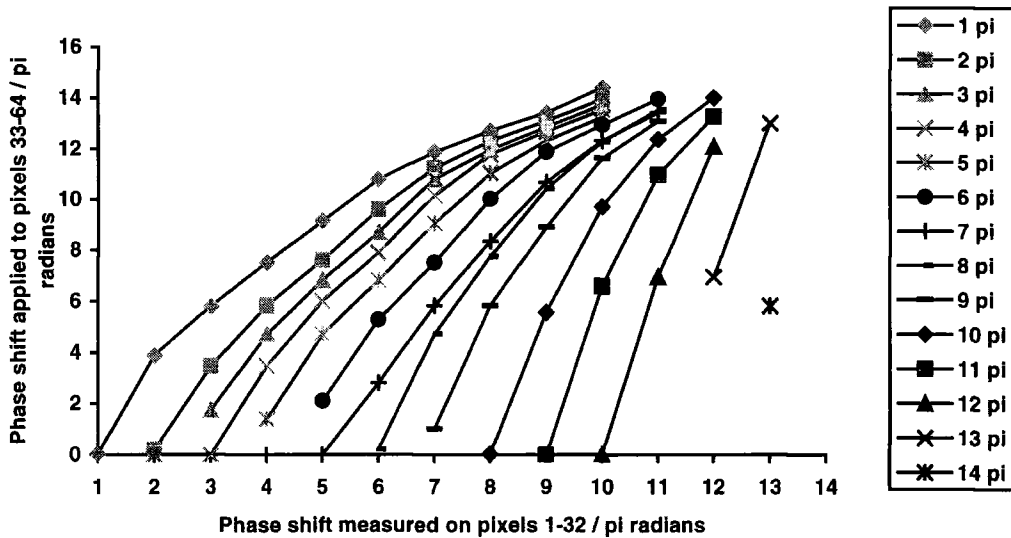


Figure 4.13. The measured phase shift produced in columns 1-32 of the SLM. Columns 1-32 has the expected phase shift applied that is indicated by the legend. The phase shift produced by columns 1-32 is shown (x-axis) as the voltage is varied across columns 33-64 (y-axis).

Figure 4.13 shows a similar experiment but the phase shift was measured on columns 1-32 whilst the voltages on columns 33-64 were varied. If there was no crosstalk between the two halves of the SLM the lines should be vertical.

It should be noted that the response time of the system was very slow. It took several seconds to reach a stable state.

For the two graphs in figures 4.12 and 4.13 it is clear that there is significant crosstalk present between pixels. For example, if a phase shift of  $\pi$  radians is required on columns 1-32 and a phase shift of  $14\pi$  is required on columns 33-64, the actual applied phase shift is  $10\pi$  on columns 1-32 and  $12\pi$  on columns 33-64. The actual measured phase shift tends towards some value between the two theoretically applied values.

#### **4.4 Discussion**

The reason for such a large amount of crosstalk error can be seen in figures 4.3 to 4.10. The spikes seen are the writing pulses that activate the individual liquid crystal pixels. The underlying waveform comes from the multiplex process. There is a contribution from each pixel to the overall waveform. Only the writing spike is above the threshold voltage of the liquid crystal. Ideally only the writing spike should effect the liquid crystal, but the underlying waveform contributes to the RMS voltage that the liquid crystal experiences and this is large enough to switch on other liquid crystal pixels partially and produce crosstalk. Because the waveform models the total pattern applied to the whole SLM, this waveform has an effect on each pixel. When only a small voltage is applied to half of the SLM this will lower the RMS voltage across the other half of the SLM and lower the applied voltage to each pixel.

The writing spike is only  $234\mu\text{s}$  long and so for  $14.766\text{ms}$  the liquid crystal pixel is undriven and will start to relax. As the number of rows is increased, the writing spike will become shorter and so the actual RMS phase shift of the

device over one frame will decrease. This limits the number of rows that can be driven in a multiplexed display because the contrast of the display decreases. This will be similar in phase only SLMs.

The effect of this partial pixel activation is common to all multiplexed displays (Pankove, 1980). If  $14\pi$  phase shift is applied to one half of the SLM and  $0\pi$  phase shift applied to the other half, there will be an induced unwanted phase shift in the  $0\pi$  half, and  $14\pi$  half will have a reduced phase shift.

This experiment only looks at the crosstalk between two halves of a 64 pixel device. It seems logical to assume that a more complex function on the SLM will also have crosstalk effects. This crosstalk reduces the potential use of the device as an adaptive optics component when the full dynamic range of the device is required. It has however been successfully demonstrated by Love *et al.* (Love, 1994) correcting a tilt in a wavefront when the device was placed in a Zygo interferometer. He only produced a phase shift of the order of  $\sim 1\lambda$ . At this level the crosstalk will be very small. Love did not investigate any effects of crosstalk in his paper.

Although multiplexing offers an easy way to drive large numbers of pixels it should be clear that the current display technology used in this device is not adequate to be adapted to phase only modulation. Other driving techniques for devices with large number of pixels suffer from poor fill factors because of the required electrical circuitry, except for optical addressing techniques. Unless optical addressing techniques are employed, it means other authors claims of liquid crystal offering a large number of pixels are brought into doubt. By careful design Meadowlark has produced a 69 pixel direct drive SLM with a high fill factor. This device is reviewed in chapter 6.

## **4.5 Summary**

In this chapter a multiplexed nematic liquid crystal SLM has been assessed for its potential as a phase modulator. The device was only a prototype and was only driven in one dimension. The device was not intended for use in astronomical applications and has not been optimised for speed. The important point that this chapter has shown is that the multiplexed driven liquid crystal SLM could not accurately cause a desired phase shift over there whole dynamic range and so was not very suitable for adaptive optics. For this reason it was decided not to continue with the GEC device, but to use standard commercially available SLMs. The simplest to use is the FLC device built by Displaytech. This is a direct drive device and so does not have the problems associated with a multiplexed device. It is the subject of the next chapter.

## Chapter 5: Binary Correction with a Point Diffraction Interferometer

### 5.1 Introduction

This chapter is concerned with using an FLC SLM as a corrective element in an adaptive optics system. An FLC SLM is capable of '*binary adaptive optics*'. This is the simplest method of providing correction with a liquid crystal device. The wavefront sensor is a Smartt or point diffraction interferometer (PDI). The PDI has been chosen in an attempt to reduce the computational overheads that are commonly found in wavefront sensors, e.g. the Shack-Hartmann, and shearing interferometer.

A simple phase unwrapping algorithm is developed and the validity of this is confirmed with computer modelling of the PDI/FLC system. The possibilities of future improvements are also explored which could make the system into a viable high speed adaptive optics system with astronomical applications among others.

### 5.2 Background

Binary adaptive optics aims to provide correction for an aberrated wavefront where conventional adaptive optics can not. This may be because of the high cost of conventional adaptive optics or other factors such as its bulky size and computational power requirements. Conventional adaptive optics can be broken down into three areas:

1. Wavefront sensing
2. Computer/control hardware
3. Deformable mirrors

To produce a low cost system, it is important to carefully balance each part of the system. It has already been said that liquid crystals offer a lower cost alternative to deformable mirrors. The price of the wavefront sensor and computer hardware must also be taken into account. In this thesis all of the real time computation will be on an IBM compatible PC with a C40 DSP image processor.

Currently, the most commonly used wavefront sensor in the adaptive optics community is the Shack-Hartmann wavefront sensor. Conceptually, this is one of the simplest designs, which may partly be the cause of its current popularity. However, the optical and conceptual simplicities are offset by the computational burden of calculating the phase. In chapters 5 and 6 we will demonstrate that a simplified Shack-Hartmann system can be run at a reasonably high speed on a single C40 and an IBM compatible PC if several criteria are relaxed. This system is still complex and slow compared to that which could be achieved with a conventional interferometer. However the need for a reference arm prohibits the use of such a sensor.

The other wavefront sensor commonly used is the shearing interferometer. These devices are still, however, computationally expensive and require two measurements to calculate the phase. Other more novel sensors exist such as wavefront inversion interferometers (Spektor, 1995), but these still require complex calculations to determine the wavefronts.

An example of a conventional Shack-Hartmann system's computational requirements is the ELECTRA system at Durham. This uses 9 TMS320C40 DSPs on a VME bus, a SUN Sparcstation 10 and a Silicon Graphics Indigo-2 workstation to decode the information from a Shack-Hartmann wavefront sensor and to control a 76 element tip/tilt/piston segmented mirror. The price of this system will clearly be more expensive than a liquid crystal SLM and so would not fulfil the criterion of a low cost adaptive optics system that this thesis sets

out to demonstrate. The PDI offers a low cost alternative to the above systems. It does not completely determine the phase but this is not important in binary adaptive optics.

### **5.2.1 STANDARD REFERENCE ARM INTERFEROMETRIC TECHNIQUES**

The potential performance of an FLC SLM in binary adaptive optics systems has been demonstrated using conventional interferometers for static correction. Thomas (Thomas, 1993) used a 128 by 128 device in a Mach-Zehnder interferometer to statically correct for an aberrated piece of glass. Thomas also cascades two devices together producing a higher order correction (quarter wave correction). This was followed up by Broomfield *et al.* (Broomfield, 1995a & b) with a four level system (eighth wave correction). Both of these systems have transmissions that are too low for astronomical purposes. The nematic LCTVs system of Kim *et al.* (Kim, 1988) also worked with a conventional interferometer.

None of the above authors have demonstrated any real time capabilities. They only corrected for static aberrations.

## **5.3 Theoretical Considerations**

### **5.3.1 THE SMARTT OR POINT DIFFRACTION INTERFEROMETER**

The theory behind the PDI was described in chapter 3. Because it is a self referencing interferometer it is suitable to use in binary adaptive optics with astronomical sources. Figure 5.1 shows an example interferogram produced by the PDI. The aberration was produced by using a singlet lens that introduced spherical aberration into the system, shown in figure 5.2. The square pattern is the FLC. Figure 5.3 shows the same interferogram but with some of the FLC pixels activated to remove the dark fringe. Figure 5.4 shows an interferogram

with no spherical aberration but a chequered pattern on the FLC (i.e., half the pixels are on and half are off, like a chess board.)

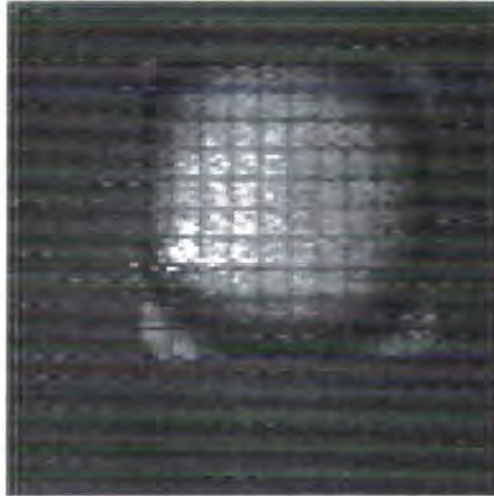


*Figure 5.1. An example of the PDI's interferogram. The FLC SLM has been placed in front of the PDI, hence the square aperture. The FLC's interpixel gaps are clearly visible as the dark cross pattern. The dark fringe is produced by an aberration introduced into the system to demonstrate the PDI. If there were no aberrations present there would be no fringes visible.*

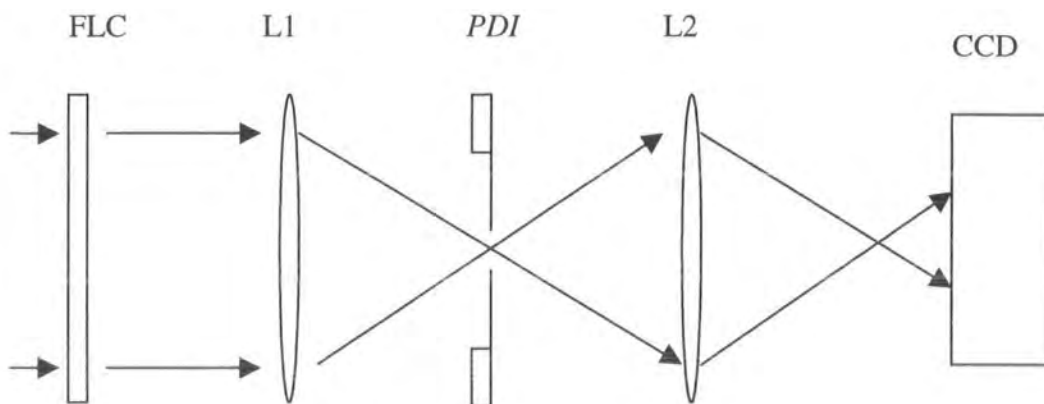


*Figure 5.2. The experimental set-up to produce the sample interferogram in figure 5.1. L1 and L2 are lenses, FLC is the FLC SLM, PDI is the Smartt PDI and CCD is a CCD camera.*

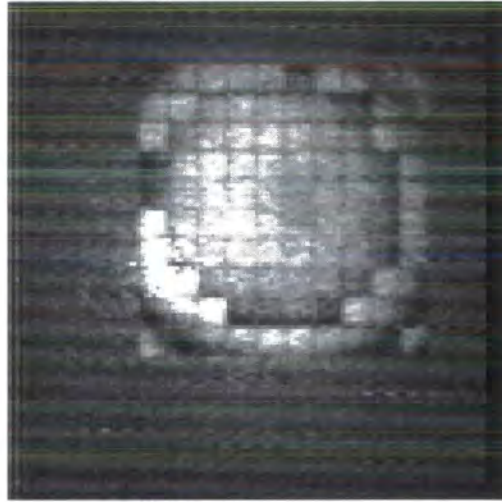


*Figure 5.3. This is the same set-up as in figure 5.1 but with some of the FLC pixels activated to remove the dark fringe.*

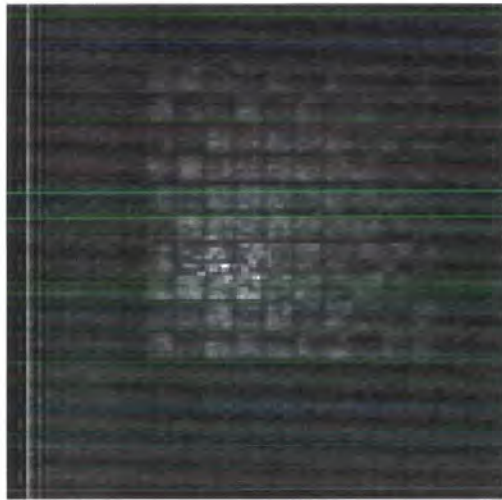


*Figure 5.4. The PDI interferogram of the FLC displaying a chess board pattern. This diffracts light out of the central maximum resulting in no reference wave, and hence no fringe contrast with the PDI.*

This type of interferometer is potentially useful in astronomy as well as high noise environments because of its lack of a reference arm. Smartt *et al.* (Smartt, 1975; 1979) proposed several applications for the PDI including the testing of telescopes. He used an  $m=0$  star as the light source and placed the PDI at the Cassegrain focus. The interferogram could be recorded with normal photography. There was no need for image intensifiers despite the PDI's low optical transmission.

There are several variations of the PDI that are of interest for wavefront sensing applications. These can be classed as conventional PDIs and phase shifting PDIs. The conventional PDI can be divided into 4 types:

1. Central field absorption. In this class the transmission function,  $T(\rho, \theta)$ , of the filter is give by

$$\begin{aligned} T(\rho, \theta) &= 1, & \rho > R \\ &= \alpha, & \rho \leq R \end{aligned} \quad [5.1]$$

where  $\rho$  and  $\theta$  are the circular co-ordinates,  $R$  is the desired radius of the central obstruction, and  $\alpha$  is the transmission of this obstruction and usually  $\alpha=0$  in this case.

2. Phase contrast. In this filter the transmission function is

$$\begin{aligned} T(\rho, \theta) &= 1, & \rho > R \\ &= e^{i\phi}, & \rho \leq R \end{aligned} \quad [5.2]$$

where  $\phi$  is some phase shift between 0 and  $2\pi$ .

3. Field absorption. (Smartt PDI type)

$$\begin{aligned} T &= \alpha, & \rho > R \\ &= 1, & \rho \leq R \end{aligned} \quad [5.3]$$

4. Field absorption and phase contrast combination

$$\begin{aligned} T &= \alpha, & \rho > R \\ &= e^{i\phi}, & \rho \leq R \end{aligned} \quad [5.4]$$

Anderson (Anderson, 1995) considers all four types of PDI and compares their fringe visibility, fringe brightness and accuracy. He concludes that the phase contrast PDI, with  $\phi=\pi$ , performs best when the incident wavefront has a variance of  $>(2\pi)^2$  and little light loss can be tolerated. However, the field

absorption PDI has the advantage of been easier to construct and are commercially available and so this type has been selected.

The wavefront can not be completely calculated with any of the above PDIs. Phase shifting PDIs have been developed by Kadono *et al.* (Kadono, 1994) and Mercer *et al.* (Mercer, 1996). Both of these systems use nematic liquid crystals to vary the phase of light passing through the field area of the PDI. Although the phase can be unwrapped the devices are too slow to be used in astronomical applications because of the need to take up to 5 interferograms to unwrap the phase. A modified PDI that diffracts light into three separate interferograms has been developed (Kwon, 1984) enabling fast unwrapping. It does however need three detector arrays and is not light efficient, making it unsuitable for astronomy. Completely unwrapping the phase is not needed in binary adaptive optics. We are only concerned in finding if part of the wavefront is out of phase with the rest.

### 5.3.2 PDI/FLC SYSTEM CONSIDERATIONS

When the PDI is used in conjunction with the FLC the basic algorithm was:

***If a region of the interferogram is dark add  $\pi$  radians phase shift with the FLC pixel that corresponds to that region.***

Several algorithms to determine the threshold value for the intensity have been considered. The major difficulty is that both the mean intensity and the fringe contrast change depending on the aberrations. An aberration in the incoming wavefront will cause the PSF to spread out so less light enters the pinhole. This reduces the fringe contrast ratio. This light then passes through the semitransparent aperture, but because this has a lower transmission than the pinhole the overall intensity of the interferogram drops. We take the familiar equation for the intensity of two interfering wavefronts of unequal amplitude  $A_0$  and  $\alpha A_0$ , where  $\alpha \leq 1$ ,

$$I(\mathbf{r}) = (1 + \alpha^2) I_0 [1 + \gamma \cos(\phi(\mathbf{r}))] \quad [5.5]$$

Here  $I_0$  corresponds to the intensity associated with  $A_0$  alone. The fringe contrast, or modulation, is given by

$$\gamma = \frac{2\alpha^2}{1 + \alpha^2} \quad [5.6]$$

and  $\phi(\mathbf{r})$  is the phase difference between the wavefronts. The maximum intensity in the interferogram is  $I_{\max} = (1 + \alpha)^2 I_0$  and the minimum is  $I_{\min} = (1 - \alpha)^2 I_0$ , the overall average is  $(I_{\max} + I_{\min})/2 = (1 + \alpha^2) I_0$ . This value would be the ideal threshold, but because the original intensity and the fringe visibility are unknown, half of the mean intensity of the interferogram was used instead. From our experience this gave the best results. This value has to be calculated for each interferogram. Several other values for the threshold were tried but these all failed for the reasons to be discussed below:

1. Consider the case when a fixed threshold is used. In a non-aberrated incident wavefront, a  $\pi$  phase shift could be added with the FLC to a number of FLC pixels. However, the intensities of the FLC pixels will be dependent on the number of pixels activated. If all of the pixels are on, the interferogram will look identical to the all off state. This is because both the reference wave and the test wavefront have been shifted by  $\pi$ . If half of the pixels are on and half are off, there will be zero contrast between the two halves because light will have been diffracted away from the pinhole of the PDI. There will be a large contrast between the on and off pixels when only one pixel is flipped. Ninety-nine of the pixels will be bright on the interferogram and the out of phase pixel will be dark. However if the intensity halfway between the on and off pixels is chosen as the threshold value and a large aberration is introduced (atmospheric turbulence for example) the total intensity of the interferogram

will be reduced. For certain aberrations the total intensity of the interferogram will drop below this threshold value and all of the FLC pixels will flip continuously and perform no correction. From experimental observations this continuous flipping between states happened most of the time.

2. The next value of the threshold to be considered was taking  $4I_0$  as the maximum intensity of the interferogram,  $I_{max}$ . This would be the brightest part of the interferogram and therefore  $4I_0$  could be taken to equal  $I_{max}$  if  $\alpha$  is close to 1. In this case, the threshold would be  $I_{max}/2$ . This does however not work in practice because of the non-uniform intensity pattern produced by the PDI. The interferogram is in fact brighter in the centre and becomes dimmer towards the edge. This is because the reference wave of the PDI is not from a point source, but a pinhole, so it does not produce a perfectly spherical wave, but some other function produced by the diffraction from the pinhole. (This effect is further compounded by the Gaussian beam profile of the He-Ne laser source.) This means that the FLC pixels around the edge of the SLM will be flipped more readily than the ones in the centre. This complication is also applicable to model 1. In practice the outer pixels of the FLC were permanently flipped. This introduced aberrations in to the beam. The assumption that  $\alpha$  is close to one also may not hold.
  
3. Consider taking the threshold as  $\beta I_{max}$ , where  $\beta$  is some real number in the range  $0 \leq \beta \leq 1$ . In this case, the above problem of pixels flipping around the edge of the FLC is reduced by choosing a low value of  $\beta$ , but this method does not work when the fringe contrast is low. If this is the case, the mean intensity,  $\bar{I}$ , will tend towards  $I_{max}$ , and so all of the interferogram may be above the threshold value if  $\alpha$  is small and no pixels will be flipped. No value of  $\alpha$  could be found that was low enough to stop the edge FLC pixels flipping and high enough to work in a low fringe contrast situation.

4. Consider taking the mean intensity,  $\bar{I}$ , or halfway between the minimum and maximum, as the threshold (the argument is similar for both). This algorithm will correct for any dark fringes no matter what the fringe contrast is like. If we consider an incident wavefront with a 0 and  $\pi$  phase shift in it, there will be a dark and light region on the interferogram. The threshold value will be between the two intensities. The FLC will correct the area that is  $\pi$  out of phase. The algorithm works in this case. However, if we now consider a  $\pi/10$  phase shift instead of  $\pi$  in the incident wavefront, we can see that this algorithm will set the threshold to be between the two intensities again. The FLC will add  $\pi$  phase shift to the  $\pi/10$  region and thus aberrate the beam, so this algorithm fails.
  
5. We used half of the mean intensity and so the threshold value is  $\bar{I}/2$ . Although this model does not reach a solution in the first frame of correction in the author's experience this produced the best correction.

To validate this assumption and get a clearer understanding, computer simulations of the PDI were performed.

### **5.3.3 COMPUTER SIMULATION**

Unlike a Michelson type reference arm interferometer, calculating the interferogram from the PDI is non-trivial. The total intensity of the interferogram and the fringe contrast depend upon the incident wavefront. A highly aberrated wavefront will produce a lower fringe contrast and lower total intensity. In our system, the correction element is placed in front of the PDI for closed loop operation and so diffraction effects from the pixels may further complicate matters.

When the system was run in a feedback loop, the system did not behave as originally expected. The device did not correct for a given aberration in the first

frame, but it took several frames to converge towards the best solution. A computer simulation was carried out to gain a better understanding of how the PDI/FLC system was performing the correction.

The simulation was carried out using Mathcad™. A phase aberration was written to an array, representing the incident wavefront. The data was then fast Fourier transformed (FFT) to give the amplitude and phase pattern in the PDI plane. An amplitude aperture mask representing the PDI was then applied to this and the array was again fast Fourier transformed to give an amplitude pattern in the interferogram plane. The intensity pattern was calculated from this. From this the intensity threshold switching value could be calculated. The array was divided into ten sections to represent the FLC pixels. If the mean pixel intensity was below the threshold intensity,  $\pi$  radians were added to the initial incident wavefront and the simulation re-run.

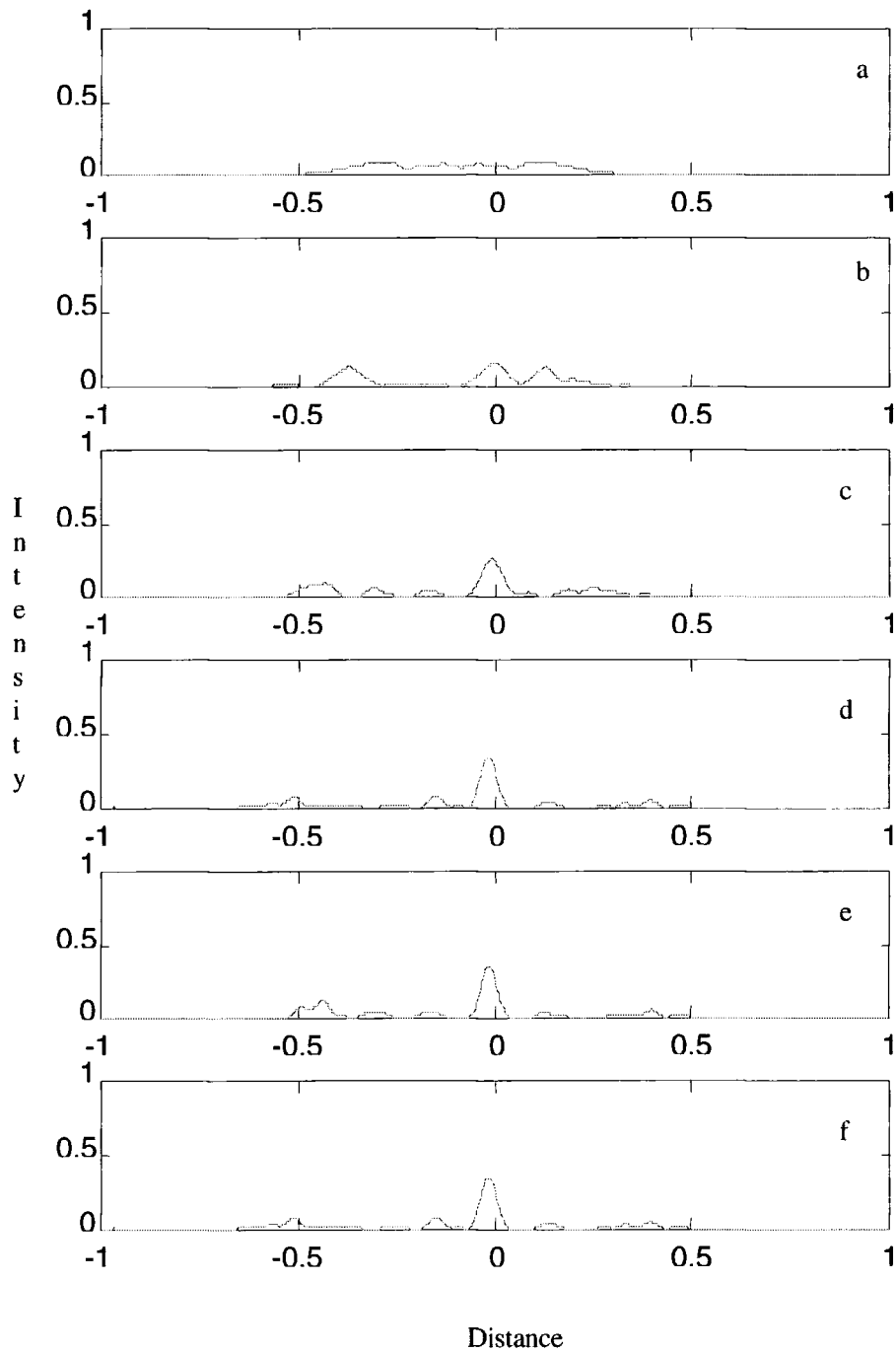
### 5.3.4 COMPUTER SIMULATION RESULTS

Figures 5.5 show the 1D simulation results of the correction of 1 wave of defocus with some global tilt. Figure 5.5 a(i) shows the initial PSF, figure 5.5 a(ii), the simulated PDI interferogram, and figure 5.5 a(iii) the wavefront incident on the PDI. Figure 5.5 a(iv) shows the reference wave produced by the pinhole. This is generated by setting the transmission of the opaque screen surrounding the pinhole to zero. In figures 5.5 b(i-iv) the first correction is made, in figures 5.5 c(i-iv) the second is made. After the fourth correction (figures 5.5 e(i-iv)) the simulation returns to the same state as that in figures 5.5 d(i-iv). The simulation oscillates between figures 5.5 e(i-iv) and 5.5 d(i-iv) indefinitely.

The PSFs shown in figures 5.5 a), b), c), and d) (i) are identical to the intensity pattern focused onto the PDI's aperture. Ideally, in the case of a non-aberrated incident wavefront, the intensity of the light that has passed through the pinhole should be equal to the intensity of the light that has passed through the opaque screen. This gives the best fringe contrast ( $\gamma=1$  in equation [5.5]). When an

aberrated beam, such as in figure 5.5 a (iii) is incident, the PSF spreads out over the PDI filter. Because the pinhole and aperture attenuation's are different, the total amount of light passing through the PDI will be different to the non-aberrated case. The contrast ratio will decrease because a different amount of light passes through the pinhole and semi-transparent screen. From these figures it can be seen that, because of the low fringe contrast in the first frame it is only possible for the system to perform a partial correction. The reference wave produced by the PDI is severely attenuated. After the first approximate correction is made by flipping the correct FLC pixels, the PSF is partially corrected (figure 5.5 b (i)) and the reference wave is restored (figure 5.5 b (iv)). This continues until the reference wave and PSF are as fully corrected as possible.

It can also be seen from figures 5.5 that under certain circumstances oscillations may occur. This happens when there is an intensity slope on the interferogram across a region corresponding to an FLC pixel with slightly more than half of the intensity under the threshold value. This causes the FLC pixel to flip, correcting the phase of that region and so raising the total intensity of the interferogram, and hence the threshold value. The intensity slope across the pixel means that the mean intensity of the pixel is under the new threshold and the FLC flips again back into its original state, and hence the correction oscillates. This is in agreement with experimental observations.



*Figures 5.5 a, b, c, d, e, f(i). The top (a) is the aberrated PSF. The one below (b) is the first correction and the next 4 are the following corrections. Figure (d) is identical to (f). The vertical scale is normalised intensity, the horizontal is distance in arbitrary units.*

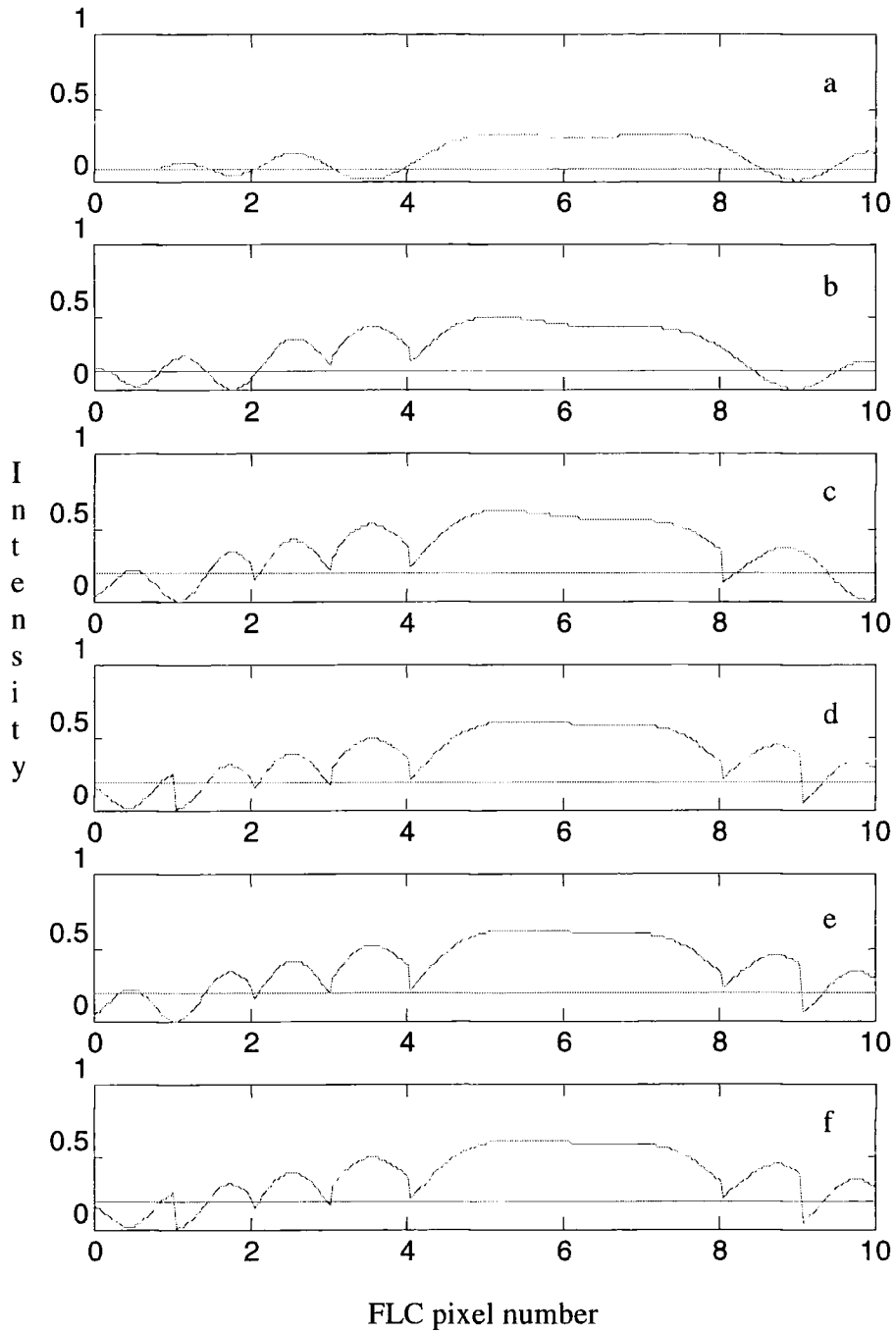


Figure 5.5 a, b, c, d, e, f (ii). The simulated interferograms. The top one (a) is the uncorrected interferogram. The horizontal line is the threshold value. The vertical scale is the intensity, the horizontal is the FLC pixel number.

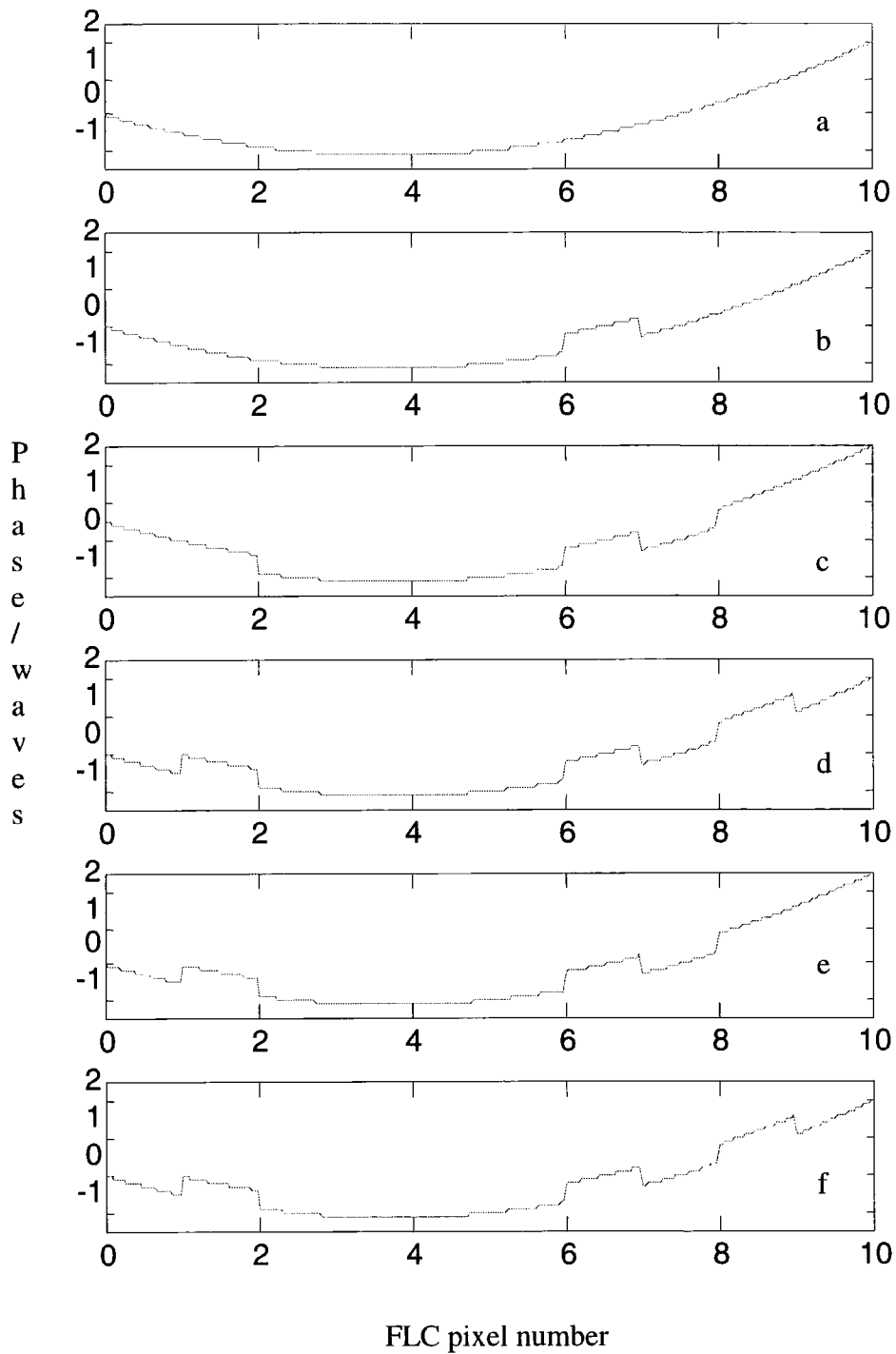


Figure 5.5 a, b, c, d, e, f (iii). The incident phase screens. The vertical scale is in units of waves. The horizontal scale is the simulated FLC pixel number.

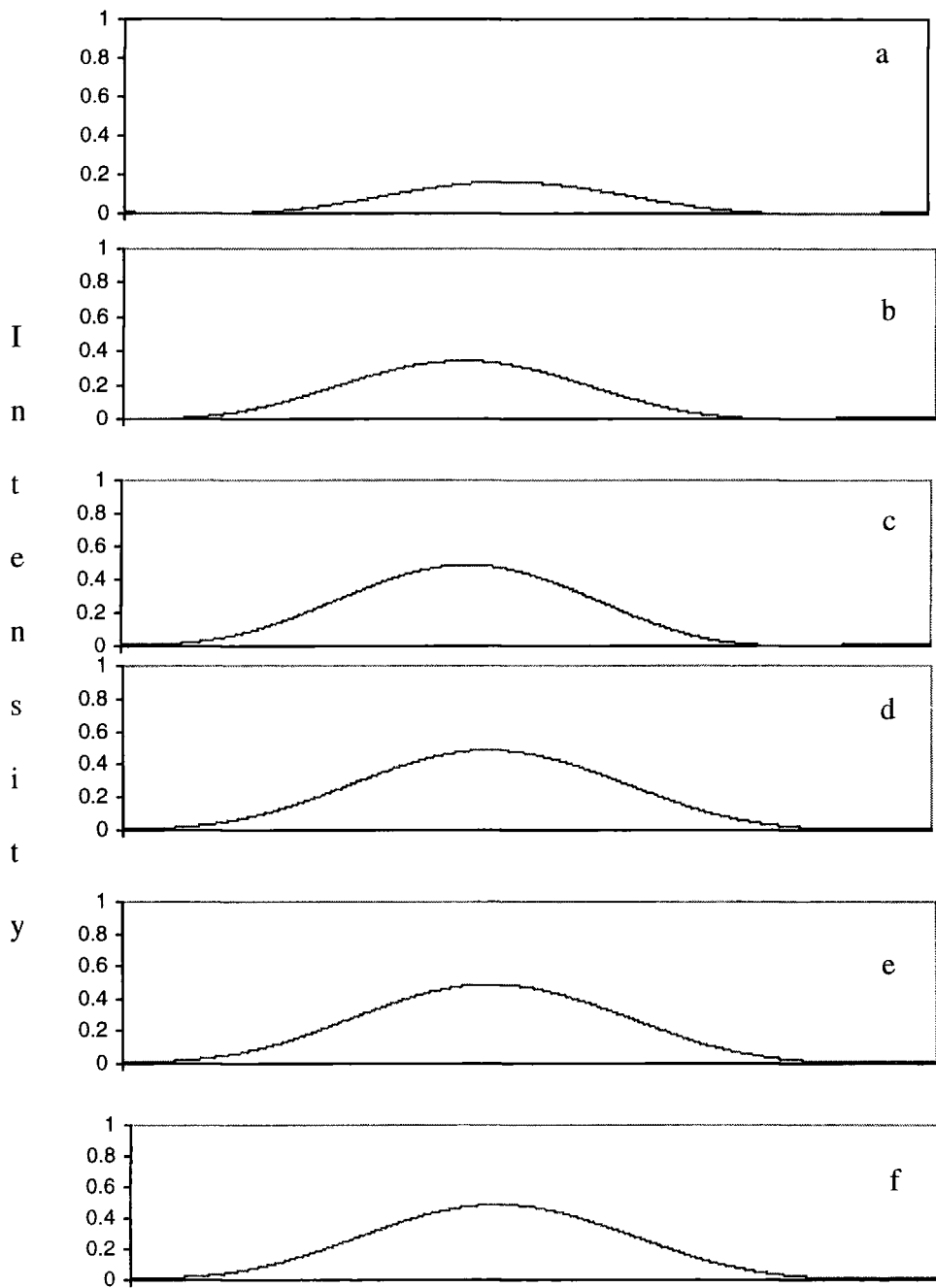
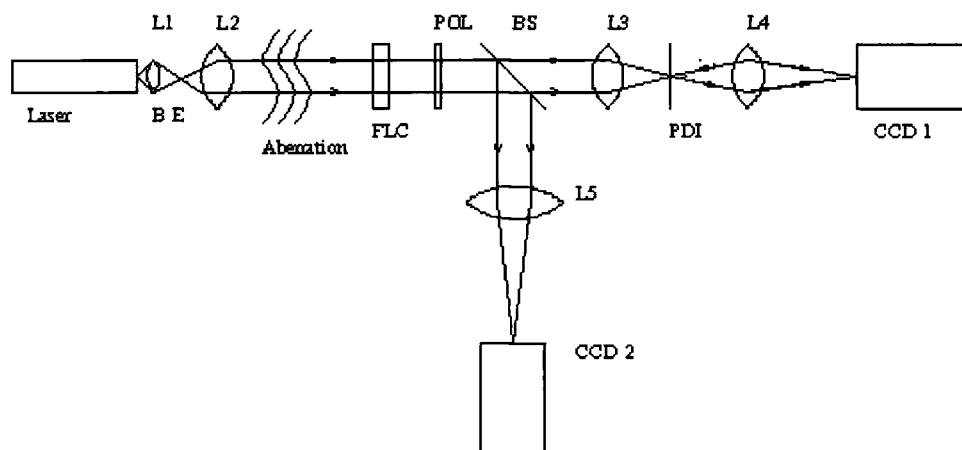


Figure 5.5 a, b, c, d, e, f (iv). The reference wave created by the PDI.

## 5.4 Experimental FLC/PDI System

### 5.4.1 SET-UP

Figure 5.6 shows the experimental set-up. The FLC was a 10x10 pixel direct drive device constructed by Displaytech with 0.885mm x 0.885mm pixels and 0.115mm inter-pixel spacing. The device was controlled by an 80486 PC with a Texas Instrument's C40 parallel processor mounted on a Coreco F/64-DSP frame grabber.



*Figure 5.6. The experimental set up. L1-L5 lenses, BS beam splitter, POL polariser, BE beam expander and spatial filter, FLC ferroelectric liquid crystal SLM, PDI point diffraction interferometer. The aberration was generated with a Meadowlark Hex69.*

A collimated 10mW polarised He-Ne laser was used for illumination. A polariser was placed after the FLC. A beam splitter was used to split half of the light to the science camera (CCD2) which measures the PSF of the system. A lens focuses the other half onto the PDI's aperture. Doublet lenses were used throughout the system to minimise spherical aberrations.

Aberrations were introduced into the system by placing the Meadowlark Hex69 nematic liquid crystal SLM in front of the FLC SLM.

### 5.4.2 CONTROL HARDWARE

A Coreco F/64-DSP board was used for the image processing. Its specifications are shown in table 5.1

Specification	Value
Video memory (VRAM)	2Mbytes
Digitisation accuracy	8 bit
Dynamic Memory (DRAM)	1 Mbyte
Camera *	Standard CCIR
Frame rate *	25 Hz
Frame size *	768 x 575 (8-bit)
Image processor	TMS320C40
Display	VGA monitor

*Table 5.1. The image acquisition equipment and processor. The frame board was capable of interfacing with many different types of CCD camera, values indicated by \* are user settings and depend on the type of camera.*

The PC was an 80486 DX2 66MHz with 16Mbytes of RAM. See figure 5.7 for the systems design.

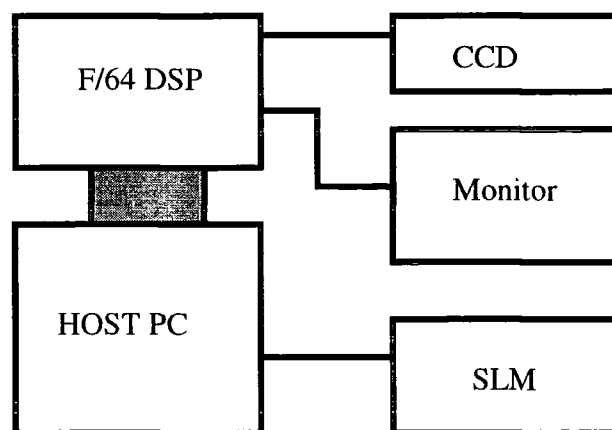


*Figure 5.7. The image processing and control hardware system.*

### 5.4.3 CONTROL SOFTWARE

Two programs were required to control the system: one for the DSP and one for the PC. The DSP software was loaded from the PC's MS-DOS command line and could only be executed by a function call from the PC software. The image processing was performed on the C40. Its results were passed to the PC over the computer's ISA bus. The C40 has direct access to the frame grabber's video RAM area over the F/64's high speed 32 bit internal bus. Because the image is stored in 8 bits, it was necessary for four pixel values to be read every time only one is required. This 32 bit word had to be separated into four 8 bit words to get the required pixel value. This process took up a considerable amount of C40 processor time because several functions had to be called and there were a large number of pixels on the camera to be processed.

The system was aligned by writing 100 10x10-pixel squares to the video monitor. At the same time, the CCD1 camera was acquiring the image of the interferogram and the FLC was slowly flipping each single pixel consecutively. The CCD camera was moved until the squares drawn on the screen were perfectly aligned with the FLC pixels.

Once the FLC and camera were aligned, the correction routine could be run. The alignment squares were no longer drawn because of the slowness of the routine. The PC software then called the DSP routine. The mean intensity was calculated by the C40 of each of the regions corresponding to the FLC pixels. This data was stored in a one hundred element array and this array was passed to the PC over the ISA bus. The PC then calculated the mean intensity and used half of this value as the threshold. The threshold value was then compared to the mean intensity of each FLC pixel area and a 10 by 10 one bit array was generated corresponding to which pixels should be flipped. This array had then to be exclusively ORed (XOR) bitwise with the previous screen to calculate the array to send to the FLC. To see why we XOR the data with the previous screen

consider just one FLC pixel. Initially the FLC pixel is set to zero. If the interferogram region corresponding to that FLC pixel becomes darker than the threshold value the FLC pixel will be flipped. However, in the next frame this pixel must not be turned off just because interferogram is now above the threshold. It must be left on until the interferogram area of the pixel becomes darker than the threshold again. Table 5.2 contains the logic table of the XOR function.

P	D	R
0	1	1
1	0	1
1	1	0
0	0	0

*Table 5.2. P represents the previous pixel value; D is the current thresholded result from the interferogram and equals 1 for a dark pixel and 0 for a light pixel.  $P \text{ XOR } D$  gives R which was then applied to the FLC array. In the next frame P will be set equal to R.*

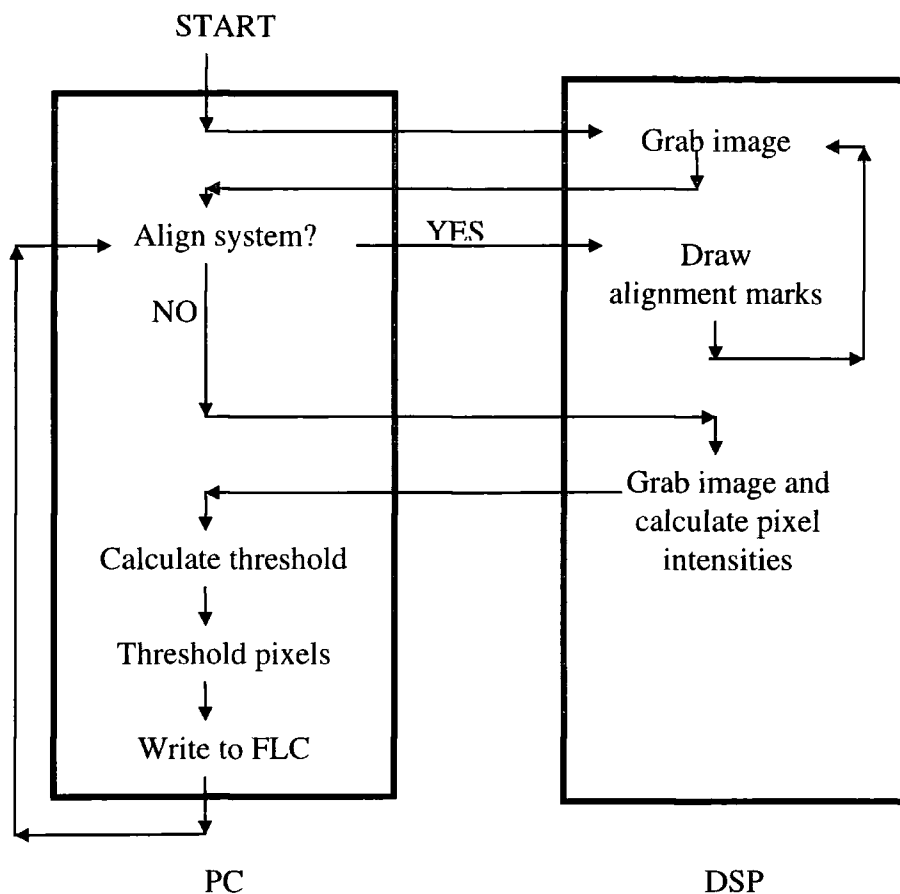


Figure 5.8. The flow chart of the control software for the FLC/PDI system. The PC and DSP sections are linked via the ISA bus.

Once the correct array was calculated it was sent to the PC's printer port which was connected to the FLC drive electronics. The next frame of the CCD camera was then taken and the process repeated (see figure 5.8).

#### 5.4.4 CORRECTION RESULTS

Figures 5.9 show the resultant PSFs taken with CCD2. Figure 5.9 a) shows the unaberrated PSF. The Strehl ratio is taken as 100% of the maximum intensity of the unaberrated PSF. Figure 5.9 b) shows the PSF with an aberration introduced into the system. The aberration was a defocus Zernike function with a peak to valley amplitude of  $0.44\lambda$  (632.8 nm) and gave a Strehl ratio of 5%. Figure 5.9 c) shows a typical corrected PSF. Figure 5.10 shows the actual images of the

PSFs. The corrected Strehl ratio was 26%, a five-fold increase. When the aberration was removed, the system returned to its initial state (i.e., the FLC pixels turned off and the Strehl ratio returned to 100%).

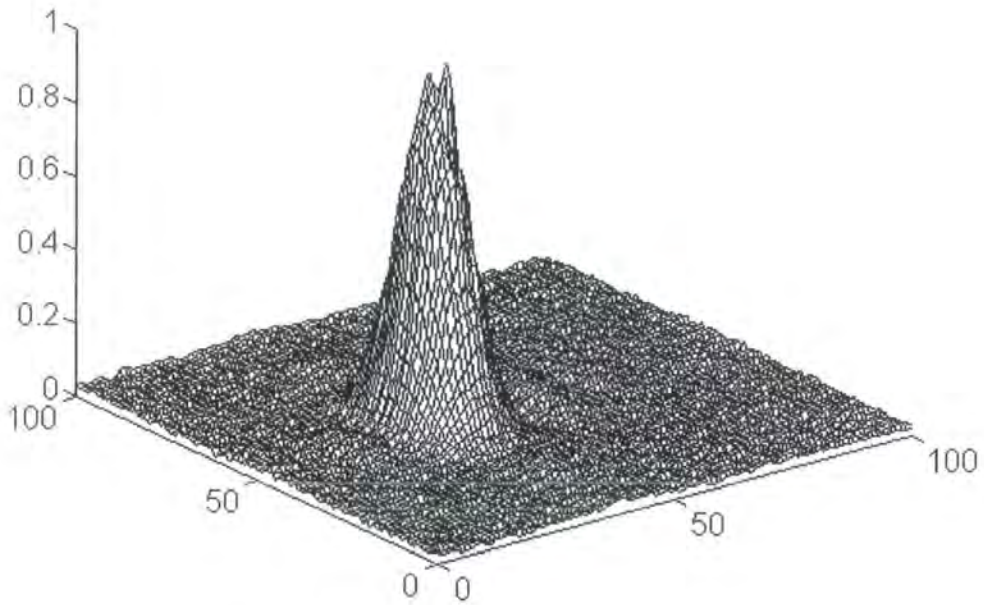


*Figure 5.9 (a). The unaberrated PSF. The Strehl ratio is defined as being 100% at the peak intensity.*

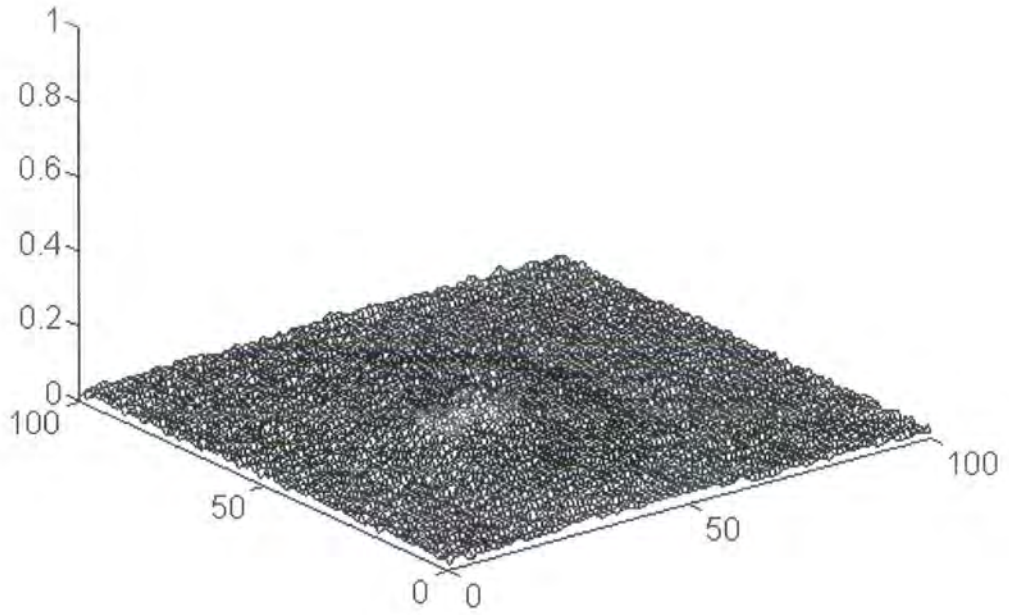


*Figure 5.9 (b). The aberrated PSF. The Strehl ratio was 5%.*

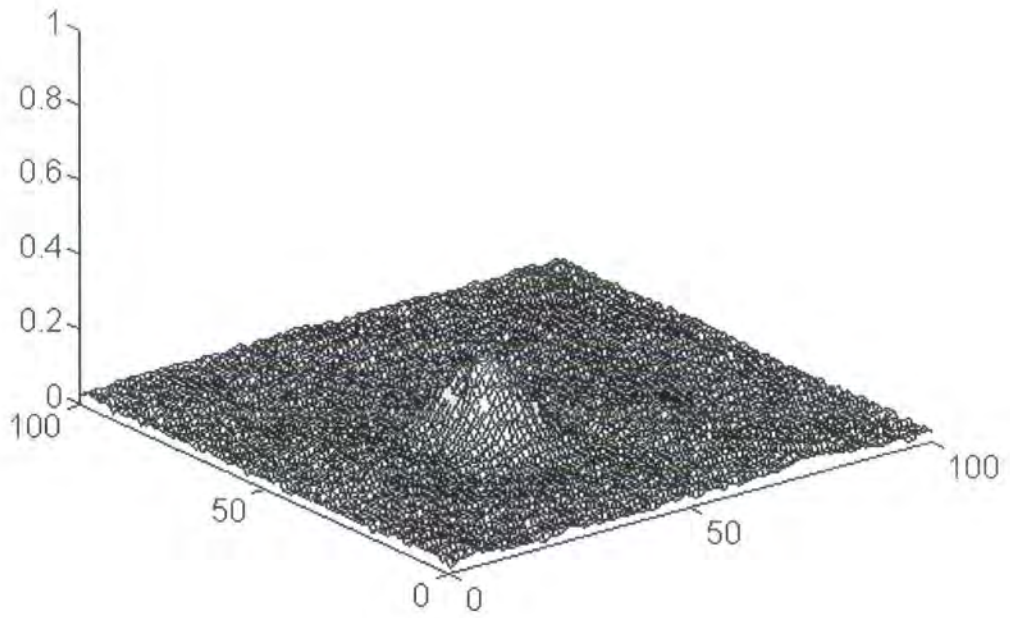


*Figure 5.9 (c). The corrected PSF. The Strehl ratio was 26%.*

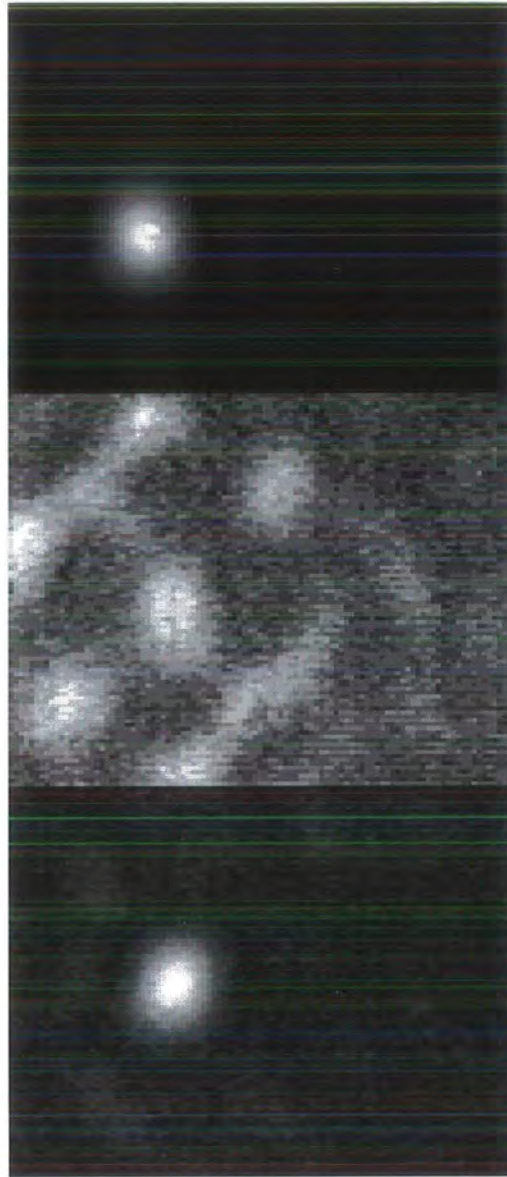


*Figure 5.10. The PSF images. The top image is the unaberrated, the middle is the aberrated, and the bottom is the corrected. Each image has a renormalised intensity.*

The frame rate was 10Hz. It took the system an average of 4 frames to produce the best correction. Oscillations of the pixels were sometimes observed.

### 5.4.5 FLC OPTICAL THROUGHPUT

The optical throughput of the FLC was measured using a non-polarised laser. The intensity was measured with a CCD camera. The transmission of the FLC with no polarisers was  $(78\pm 4)\%$ . The throughput of a single polariser was  $(32\pm 2)\%$  and the throughput of the FLC with the two polarisers in place was  $(2\pm 0.5)\%$ . This compares reasonably with the calculated transmission above if the transmissions of each component are taken into account. From [2.10] the theoretical transmission is 33%, correcting this with the optical transmission of each component, the total transmission is reduced to 2.6%. It should be noted that the polarisers used to calculate the throughput were of lower quality than the polariser in the main experiment which had a quoted transmission of 42%.

## 5.5 Discussion

With the system in a closed loop, it was not possible to stop FLC pixel oscillations with our simple algorithm. However, the system still produces a five-fold improvement in the Strehl ratio. One way round the oscillations would be to run the device in an open loop system. In this configuration, the FLC would not be in the same optical arm as the PDI but in front of the science camera (see figure 5.6). Since our system has to work towards the best solution it is not known how well the FLC SLM would perform in open loop. It would also not correct any systematic errors such as optical non-uniformities in the FLC SLM.

Despite the low number of pixels (100) the FLC device has still managed to partially correct for an aberration that is typically associated with a telescope of size  $12r_0 \sim 1-2$  metres (Wang, 1978), where  $r_0$  is the Fried parameter (typically 10-20cm). Love *et al.* (Love, 1995) have shown that a  $128 \times 128$  pixel device would be capable of correcting atmospheric aberrations across a telescope of up to  $40 r_0$  in diameter. Such devices are currently available commercially, although their suitability has not been fully investigated.

The corrected Strehl ratio of 26% is somewhat lower than the quoted theoretical limit of 40.5%. This is to be expected because of the large residual wavefront errors caused by the finite size, and the finite number of FLC SLM pixels.

A major limitation of the FLC SLM used in this experiment was that its retardance was neither  $\pi$  nor was its switching angle  $90^\circ$ . This would be needed if such a device were to be used for light starved astronomical purposes where a high transmission is required. The retardance of our system was  $0.6\pi$  and it had a switching angle of  $45^\circ$  giving a maximum theoretical transmission of 33%, and an experimentally measure transmission of 2% (including polarisers). Although no company to date has produced a high switching angle FLC SLM, it should be easier to control the retardance of future devices by fine tuning the cell thickness. If a device with  $\pi$  retardance could be produced, the theoretical transmission would be improved to 50% even with a switching angle of only  $45^\circ$ .

Tip/tilt has not been corrected in this experiment. The PDI could not measure large amounts of tip/tilt since the focused beam moved away from the aperture in the centre of the PDI mask. Tip/tilt would need to be removed with a mirror before the light was corrected by the FLC. This would require an additional sensor (such as a quad cell) and so the light throughput of the total system would be further reduced.

### 5.5.1 PHOTON FLUX

Liquid crystal devices offer the possibility of a very large number of pixels. Monitors in laptop computers have typically  $640 \times 480$  pixels, although their low pixel fill factor and low optical flatness makes them unsuitable for astronomical adaptive optics. Displaytech currently offer a  $256 \times 256$  device with a high fill factor (87%) and a frame rate of 3kHz (Ref. Displaytech). This gives a much greater number of degrees of freedom than a standard deformable mirror.

Increasing the number of pixels to a much larger extent will, however, slow down the operating speed of the system. Computation time aside, the number of photons from an astronomical source is limited and fixed. If the number of pixels is doubled the integration time required is also doubled. The number of photons detected per FLC pixel,  $N_{det}$ , in integration time,  $\tau$ , is given by

$$N_{det} = \frac{Q \cdot N_i \cdot \eta \cdot F \cdot \tau}{n} \quad [5.7]$$

where  $n$  is the number of pixels,  $Q$  is the quantum efficiency of the detector,  $N_i$  is the incident number of photons into the interferometer,  $\eta$  is the efficiency of the PDI, and  $F$  is the fill factor of the device.  $N_i$  is (Schroeder, 1987)

$$N_i = N \cdot D^2 \cdot \Delta\lambda \cdot 10^{-0.4m} \epsilon \quad [5.8]$$

where  $N=10^8$  is the number of photons per second per metre squared per nanometre for a zeroth order A0 star at 550nm,  $\Delta\lambda$  is the bandwidth and is 40nm,  $m$  is the stellar magnitude, and  $\epsilon=50\%$  is the efficiency of the system to the front end of the interferometer. For a 1m telescope, imaging a magnitude 7.7 star,  $N_i$  is approximately  $1.6 \times 10^6$  photons per second. The value of  $\eta$  depends on the incident wavefront and is typically as low as 5% (Love, 1995). Assuming a quantum efficiency of 0.8,  $F=100\%$ , and  $n=100$ ;  $N_{det}=0.166$  photons per frame per pixel at the maximum frame rate of 4000Hz. Clearly, the device could not be operated at such speed. If we limit the frame rate to that required to correct for typical atmospheric aberrations, about 100Hz, we find for at least one photon per frame per pixel the maximum number of pixels is 665 or about  $25 \times 25$ . This assumes that the transmission of the FLC is 100%. If the current Displaytech device is used, the transmission becomes substantially worse. With only 2% transmission, the maximum number of FLC pixels for one photon per frame is only 13 (or  $\sim 3 \times 3$ ).

Because the number of photons entering the telescope is proportional to the diameter of the telescope squared, we can rearrange equation [5.7] to calculate the maximum number of FLC SLM pixels usable in a telescope of diameter  $D$

$$n \leq Q \cdot N_{i \text{ 1 metre}} \cdot \eta \cdot F \cdot D^2 \cdot \tau \quad [5.9]$$

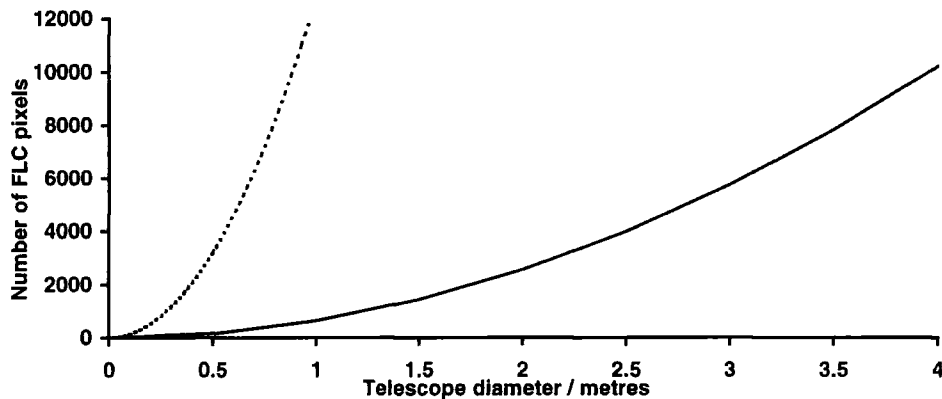


Figure 5.11. The maximum number of pixels that could be used in a telescope versus the diameter of the telescope. The solid line is for  $\eta=5\%$ , the dotted line is for  $\eta=100\%$ .

$N_{i \text{ 1 metre}}$  is the photon flux for a 1 metre telescope. If  $\tau = 10\text{ms}$ , the number of pixels versus telescope diameter is shown in figure 5.11 for both  $\eta=5\%$  and  $\eta=100\%$ . It is important to maximise the number of FLC SLM pixels in order to reduce the residual wavefront error after correction in order to get as close as possible to the maximum corrected Strehl ratio of 40.5%.

To improve the photon flux the most obvious solution is to increase  $\eta$ . It should be noted that  $\eta$  depends on the aberration. For a well corrected aberration  $\eta$  will increase. If the PDI was replaced by a phase contrast PDI the value of  $\eta$  would increase to  $\sim 100\%$ , increasing the number of photons 20 fold.

The above calculation does not take into account the absorption of the optical components in the telescope and any real system would require more than one photon to operate. It does show that to run a pixelated adaptive optics system in a telescope it is necessary to carefully balance the number of pixels with the available light.

The system could be tested on a telescope system providing the following criteria can be achieved:

- An FLC with  $0-\pi$  phase shift can be developed with a high transmission.
- The speed of the system can be increased.
- The transmission of the PDI can be increased.

### 5.5.2 FUTURE CONSIDERATIONS

The system is currently limited to 10Hz. This is because of the large amount of image data from CCD 1 (figure 5.6) that has to be processed by the C40 processor chip (768 x 575 bytes of data per frame). If a higher speed camera, such as the DALSA used in chapter 7 replaced the CCD camera used, the system bandwidth should be improved. This camera has a maximum frame rate of 838Hz and 128x128 pixels. It should be possible to operate this system at speeds in excess of 100Hz, which would be adequate for most astronomical applications. This does not however take into account the efficiency of the camera, which is quite low, but other similar cameras are available with higher efficiencies.

Because the system takes more than one frame to reach the optimum solution, the system will have to be operated several times faster than an aberration. The precise speed needed is yet to be determined. The system took four frames to reach the optimum correction in §5.4. However, it did partially correct in the

first frame. It is unclear how the system will operate in a time evolving situation. It is possible that once the system has achieved the correction, any small perturbations made to the aberration will be corrected in the next frame.

If a larger FLC SLMs were to be used in the future this would again slow down the system because of the large amount of data. The Coreco F/46 board used in this experiment has the capabilities of mounting more C40 chips and so increasing its computing power. A cheaper alternative would be to use an array of photodiodes instead of a CCD camera to image the interferogram. The position of each photodiode would correspond to each FLC pixel. If each photodiode was connected to a simple thresholding circuit, the whole system could be built to work at the maximum speed of the FLC SLM (4000Hz). In reality, for astronomical purposes the limit would be the number of photons entering the telescope needed to trigger the photodiodes.

## **5.6 Summary**

In this chapter a binary adaptive optics system has been demonstrated using a PDI and 10x10 FLC SLM. The technique does not attempt to fully correct an aberrated wavefront but still an improvement in Strehl ratio from 5% to 26% was achieved. The frame speed of the system was 10Hz and this is currently limited by the computer power. A model of the PDI was also developed with a suitable threshold value.

The potential for an FLC SLM with a Shack-Hartmann wavefront sensor is discussed in the next chapter. This wavefront sensor is commonly used for adaptive optics and does not have many of the problems that have been found with the PDI such as the low through-put or the oscillations caused by the PDI's unusual characteristics.

## **Chapter 6: A Liquid Crystal Atmospheric Turbulence Simulator**

### ***6.1 Introduction***

There is a need to test all adaptive optics systems by introducing aberrations into the optical beam. This can be achieved in one of three ways: try the system on a telescope; use a deformable mirror to introduce known aberrations; or introduce unknown aberrations such as turbulence generated by a heating element, a fan or a rotating piece of aberrated glass. The first option is naturally the best for an astronomical adaptive optics system, but it requires shipping the device to a telescope and allocating telescope time which can be difficult and expensive. The use of deformable mirrors is very expensive. The third option uses non-ideal statistics and is not very controllable. In this chapter we develop a liquid crystal based atmospheric turbulence simulator (ATS). This will be used to generate aberrations with scaleable Kolmogorov statistics for testing the adaptive optics system in chapter 7. It will also be of potential use to the whole of the adaptive optics community.

### ***6.2 Background***

Previous adaptive optics systems using liquid crystals have only concentrated on static correction. To introduce an aberration into a system such as this is trivial: a piece of non-flat glass can be inserted into the optics, or even the aberration introduced by the SLM itself when the SLM is of low optical quality.

When an adaptive optics system is to work in real time the situation becomes more difficult. A method of producing variable aberrations of the correct amplitude, phase, and speed is required. A mechanical system could be constructed such as a piece of aberrated glass rotated with an electrical motor. Although simple this technique would have several problems. The aberrations would be cyclic, i.e., they would be repeated after the glass has rotated  $360^\circ$ . The

motor could introduce large amounts of tip/tilt from mechanical vibrations; a problem for liquid crystal correction where tip/tilt stroke is limited. It also will not have the correct power spectrum of the desired aberration to be modelled unless the glass is specifically made that way.

A device that could be used to generate a time varying aberration with the correct statistics would clearly be useful for testing the performance of an adaptive optics system. The statistics to be used in the case of atmospheric turbulence are Kolmogorov. To the author's knowledge there has been little work on producing simulated turbulence. Most groups use either heater/fan type arrangements or expensive deformable mirrors. A second deformable mirror only used for laboratory simulation is prohibitively expensive. This chapter presents an alternative method using liquid crystal SLMs.

### ***6.3 Requirements for an Atmospheric Turbulence Simulator (ATS)***

Any ATS must fulfil the following criteria:

1. It obeys Kolmogorov statistics.
2. It needs to be relatively small. The whole point is that it fits on the optical bench.
3. It should be able to simulate various wind speeds.
4. It should be able to simulate various values of  $D/r_0$ .
5. It should not be cyclic, i.e., the phase screens should not repeat for at least a reasonably long time.
6. It needs to produce the correct Strehl ratio and PSF.
7. The aberrations should be continuous and have no sharp discontinuities.

Points 3 and 4 are so that different sized telescope diameters and wind speeds can be modelled.

## **6.4 A Liquid Crystal SLM as an ATS**

Of the two possible liquid crystal materials that could be used for an ATS, only a nematic device is really suitable. An FLC is considerably faster but will only introduce  $0/\pi$  aberrations into a wavefront. This will not fully test any system that provides analogue correction. Nor will it introduce aberrations with the correct statistics. It was shown in chapter 4 that the multiplexed 64x64 SLM will not produce the correct phase pattern. For this reason a Meadowlark Hex69 nematic liquid crystal SLM was used. This device is now an 'off the shelf' package, but it was originally designed for the University of Durham's adaptive optics program.

The concept behind the Hex69 design was for correcting aberrations. Therefore, in principle, it should be equally as good at generating aberrations. It is a nematic device and capable of giving an analogue response. Love (1997) has shown the device does introduce Zernike aberrations into collimated beams well ( $\sim\lambda/10$  error), but he did not assess the performance with either a real time aberration, or more than one mode. The following sections will attempt to do that. The basic principle behind the ATS is to generate simulated phase screens off-line and then map them onto the SLM in real time.

## **6.5 Meadowlark Hex69 Device Description**

The pixels are in a hexagonal format which is shown in figure 6.1. This format allows either a circular aperture or a square aperture. There is total of 69 pixels; each is directly driven, i.e., there is an individual electrode to each pixel. The liquid crystal material is sandwiched between two layers of optically flat quartz with the indium tin oxide (ITO) electrodes deposited and then the pattern lithographically etched on the inside surface. The liquid crystal was controlled by an AC electric field that could be varied from 0 to 10V in divisions of 1mV. The potential across each pixel was controlled by a PC. The specifications are given in table 6.1.

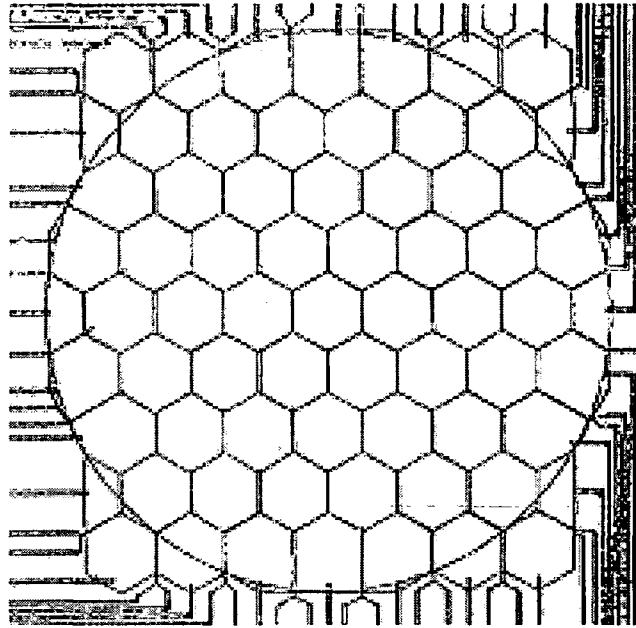


*Figure 6.1. The pixel layout of the Hex69. The hexagonals are the liquid crystal pixels. The lines coming out of them are the ITO connections. The circle is the active area. Note it can also be configured with a square aperture.*



Specification	Value
Active area	14.7 mm diameter circle or 12.5 mm x 12.5 mm square
Pixel size	Hexagonal with a maximum diameter of 2.08mm
Number of pixels	69
Transmitted wavefront distortion	0.038 $\lambda$ peak to valley or 0.007 $\lambda$ RMS <sup>1</sup>
Substrate	Fused quartz
Inter-pixel spacing	20 $\mu$ m
Pixel fill factor	~97%
Total stroke	1.1 $\mu$ m ~2 $\lambda$ in the visible
Drive electronics bandwidth	26Hz
Liquid crystal material	Merck E44
Liquid crystal cell thickness	5.5 $\mu$ m
Birefringence	$\Delta n = 0.262$

Table 6.1. Hex69 Specifications.

### 6.5.1 DRIVING THE HEX69

The Hex69 could be controlled by most IBM compatible PCs. The voltage waveforms that were applied to the liquid crystal material were generated by a Meadowlark SLM2256 *Shape-Shifter* SLM controller. This could be controlled from a PC by two methods. The simplest was via the computer's printer port. The second method was to use a digital output board on the PC (N.B. it should also be possible to interface the device with a UNIX workstation using this method). The printer port provided the simplest method of controlling the device and was used for the laboratory based work in this thesis. The drawback was this method limits the speed of the device to 38ms per frame. This speed has been

---

<sup>1</sup> $\lambda=638.2$  nm He-Ne laser.

measured using a 33MHz 80386 and a 66MHz 80486 PC and appears to be machine independent. Using a digital output board would enable the device to be run at higher speeds, however the speed of the liquid crystal would not increase so an improvement in speed would only be noticed for small differences in the phase shift between each frame.

## **6.6 The Hex69 as an ATS**

### **6.6.1 PHASE SCREEN GENERATION METHODS**

There are currently several methods of generating atmospheric phase screens. Roddier (Roddier, 1990) used a method involving Zernike modes. Although the major advantage of this was the high calculation speed of each mode and the fact that it produced a circular phase screen that would map onto the Hex69 well. It was necessary to produce 400 Zernike modes to obtain an accurate representation of the atmosphere. It is also unresolved how to generate a time varying phase screen with this method.

### **6.6.2 LANE'S FOURIER METHOD**

Lane and Glindemann (Lane, 1992) (Glindemann, 1993) produced phase screens using a Fourier convolution method. The basic technique can be summarised as follows. A square array is filled with random numbers. The array is then scaled by the power spectrum of the Kolmogorov turbulence. This is then fast Fourier transformed (FFT) into real space to produce the simulated phase screen. To achieve the correct statistics for the lower order modes a very large amount of data needs to be modelled (>several times the telescope diameter). To reduce the need for such large amounts of data to be calculated, lower order Zernike modes are added in instead. This technique can be used to generate time evolving phase screens. By generating a large rectangular array, an aperture can be moved across the array to give the effect of temporal variation.

### 6.6.3 SOFTWARE

Software written in FORTRAN 77 was provided by Glindemann to calculate the phase screens. The data was generated on a SUN SPARC STATION IPC. Two thousand frames were generated, taking several hours. To avoid aliasing, the data arrays were twice as big as the telescope diameter. Each frame was a 128x128 floating point array, requiring a total of 125Mb of disk space. The data parameters used to generate the screens are shown in table 6.2.

Parameter	Value
$D/r_0$	1
Total array size	128x128 4 byte floating point
Size of aperture data	64x64 4 byte floating point
Number of elements moved per frame <sup>2</sup>	2
Number of lower order modes added	7
Total number of frames	2000

*Table 6.2. The specifications for the atmospheric turbulence screens to be generated.*

A value of  $D/r_0=1$  was chosen so that the raw phase could be scaled by a factor of  $(D/r_0)^{5/3}$  to simulate any telescope diameter. The wind speed is related to  $D$ , the number of elements moved per frame  $N_m$ , the number of elements in the array  $N_e$  and the frame speed of the SLM,  $F$ . The wind velocity,  $v_x$ , is the distance travel per frame divided by the frame speed. So

$$v_x = \frac{N_m}{N_e} D \frac{1}{F} \quad [6.1]$$

$$= \frac{2}{64} \cdot 1 \cdot \frac{1}{38 \cdot 10^{-3}}$$

---

<sup>2</sup>I.e., the frame is shunted to the left of the previous frame by two element/pixels.

$$= 0.822 \text{ ms}^{-1}$$

or about  $3\text{km hr}^{-1}$ , for a 1m telescope. This is a very still day but it can be increased by increasing the value of  $N_m$  up to maximum of 64, giving  $v_x = 95\text{km hr}^{-1}$ , although at the expense of the correlation between consecutive frames.

The liquid crystal in the Hex69 SLM is too slow to accurately produce the large phase shifts required by the tip/tilt terms when the SLM is running at full speed. It has been assumed that a real liquid crystal adaptive optics system would have a separate tip/tilt mirror, for this reason tip/tilt was not modelled. The generated data was separated into individual files and the tip/tilt and piston was removed by a least squares fitting program. The mean phase over each of the Hex69 pixels was then calculated and this was written to a file containing the  $69 \times 2000$  pixel values.

The software supplied with the Hex69 could only handle a maximum of 96 frames. This would only give 3-4 seconds of turbulence. To use all 2000 frames generated new software was developed by the author. This was written in C and compiled with a Semantec C++ compiler. This compiler has a 32-bit DOS extender option, and unlike ordinary compilers it allows full access the PC's RAM instead of the usual 640kb limit imposed by MS-DOS.

The program had several command line options: the number of frames skipped,  $\Delta$ ; the frame speed,  $\tau$ ; the scale,  $\alpha$ ; and the data file name. The data file was read into an array and scaled by the amount  $\alpha$ .  $\Delta$  was to make the wind speed variable, changing it to be more than unity reduced the total number of frames available but it was more convenient than regenerating all of the data from scratch. The frame speed was limited to a minimum of 38ms.

The data was converted into voltages by the polynomial measured in §6.7.3. Once the data was in the correct format it was sent to the SLM via the

computer's printer port. Using this method the only limit on the number of screens that can be used was the amount of RAM of the PC. The ATS took 76 seconds to completely run through all 2000 frames. Once the end of the data was reached, the data was run through backwards so that there was no sharp discontinuity between frame 2000 and frame 1.

Zernike modes could also be applied to the device using pre-existing software modified for this device by the author. The software calculated the phase over each pixel by using the Zernike modes of table 3.2. The phase was then converted to voltages using the calibration polynomial.

## **6.7 ATS Performance Measurements**

To characterise the performance of the Hex69 as an ATS, both the spatial and temporal characteristics of the system need to be measured. This performance was measured in three ways: the temporal power spectrum of the phase, the Zernike power spectrum and the Strehl ratio. Ideally, the measurements should be taken over as many phase screens as possible. To measure the power spectrums a Shack-Hartmann wavefront sensor was used.

### **6.7.1 THE SHACK-HARTMANN WAVEFRONT SENSOR**

A Shack-Hartmann wavefront sensor measures Zernike modes in the incident wavefront. Because it can completely determine the wavefront (except for the piston term) in real time and from one measurement, it is ideal for measuring the performance of an ATS. The Shack-Hartmann is also used in many adaptive optics systems and will be the wavefront sensor for the systems described in the next two chapters.

The interaction matrix,  $\mathbf{B}$ , (equation [3.28]) was calculated off line by calculating the differential for each mode in each axis for all of the theoretical spot centres. The actual values of the elements of  $\mathbf{B}$  depend upon the size and

shape of the lenslet array. Then the pseudoinverse of  $\mathbf{B}$  was calculated off line. These calculations were done with MATLAB™.

### 6.7.2 HARDWARE AND OPTICAL SET-UP

The computer hardware set-up was similar to that described in chapter 5. A C40 processor was mounted on a frame grabber and hosted in a 486 PC, the set-up is shown in figure 5.7. The camera used for the Shack-Hartmann was a DALSA CA-D1-0128 with a data rate of 16MHz. The camera had 128x128 pixels and a frame rate of 838Hz. The pixels were arranged in a square array, 2.048x2.048mm in size. This camera was not optimised for low light environments, however since a laser was the source there was no shortage of photons.

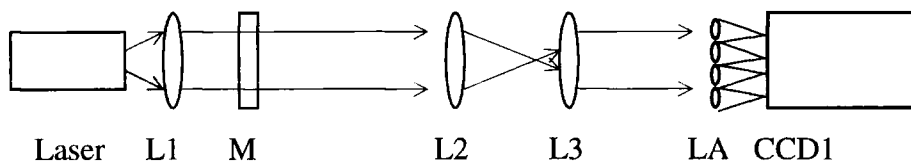


*Figure 6.2. The optical set-up of the Shack-Hartmann/Hex69 system. L1, L2, L3 are doublet lenses, LA is the lenslet array, M is the Hex69 SLM, and CCD1 is the DALSA CCD camera. The laser is spatially filtered, beam expanded and then re-collimated by L1.*

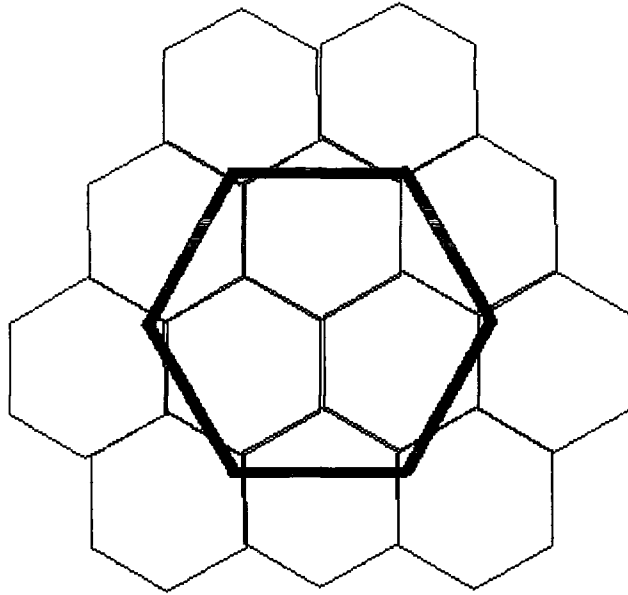


*Figure 6.3. The approximate sampling of the Hex69 pixels (thin lines) by a Shack-Hartmann lenslet (dark line).*

The optical set-up is shown in figure 6.2. A 10mW He-Ne laser was the light source. This was collimated and beam expanded to  $\sim 2$ cm diameter. The two lenses L2 and L3 demagnify the beam so that at least 3 Hex69 pixels are sampled by a lenslet (see figure 6.3). If there were only 2 pixels sampled by the Shack-Hartmann it could have only measured tilt in one direction. If there were only one pixel there would be no measurement because only the piston of the phase would change. 19 lenslets are used to sample the wavefront. The image of the spots for an unaberrated beam is shown in figure 6.4. Figure 6.5 shows the same spots with  $0.5\lambda$  of defocus added by the Hex69.

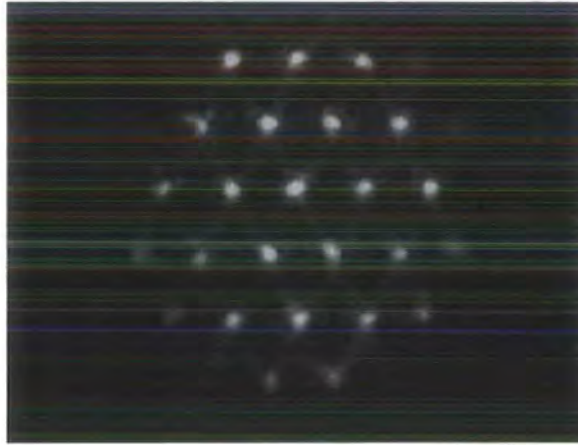


Figure 6.4. The Shack-Hartmann spots with no aberrations in the system present.

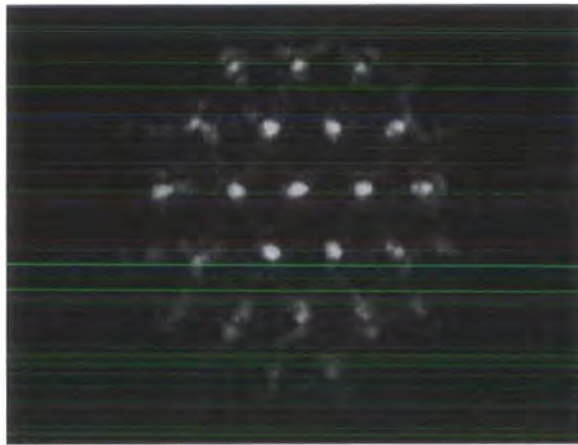


Figure 6.5. The Shack-Hartmann spots with  $0.5\lambda$  of defocus introduced by the Hex69.

The specifications of the lenslet array are given in table 6.3.

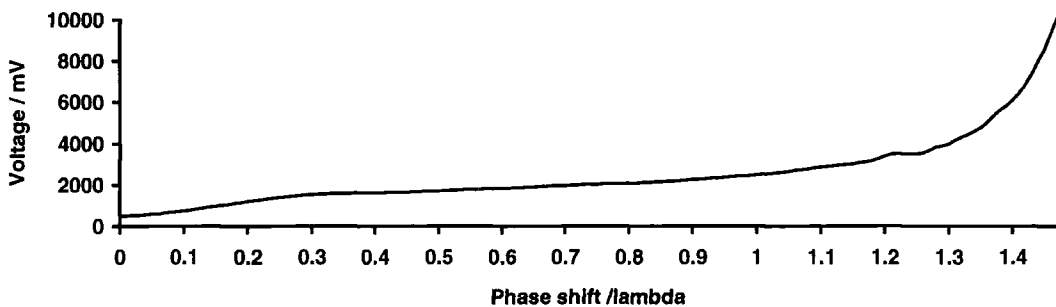
Specification	Value
Manufacturer	Adaptive Optics Associates (AOA)
Lenslet Aperture	497 $\mu$ m
Focal length	97.0mm
Number of lenses	60x52
Pixel shape	Hexagonal
Fill factor	>99%

Table 6.3. The specifications of the lenslet array used in the Shack-Hartmann.

The alignment of the system was very critical since the Shack-Hartmann typically measured Zernike mode amplitudes with an error of  $\lambda/100$ . High quality doublets were used for all of the lenses. Any misalignment becomes obvious when the Zernike modes are measured although several features of the software described below help minimise the problem.

### 6.7.3 CALIBRATION OF HEX69

The calibration of the SLM was made using a Zygo interferometer. Half the Hex69 pixels were held at zero volts and the other half were increased over 10 frames by 1V. The Zygo was used to measure the phase shift between the on and off pixels. It was assumed that the phase shift would always increase with voltage, this assumption removed the  $2\pi$  ambiguity associated with the Zygo. To minimise any error that may be caused by non-uniformities in the Hex69 the phase shifts were an average of all the pixels activated. A 6th degree polynomial was then fitted to the data using a FORTRAN 77 routine and is shown in figure 6.6.



*Figure 6.6. The voltage versus phase shift response of the Hex69. The polynomial fitted is a 6<sup>th</sup> order with a correlation coefficient,  $r$ , of 0.998776*

### 6.7.4 TEMPORAL RESPONSE OF THE HEX69

The temporal response of the Hex69 was measured by taking into account the birefringent nature of liquid crystals. If the incident light is polarised such that its

axis of polarisation bisects the ordinary and extraordinary axis of the liquid crystal, the SLM will modulate intensity instead of phase. The usual phase shift  $\Delta$  then appears as a modulation term and the intensity is

$$I = I_0 \sin^2\left(\frac{\Delta}{2}\right) \quad [6.2]$$

From figure 6.6, the value of  $\Delta$  moves through about 1.5 wavelengths, i.e., through about  $3\pi$  radians. Whenever  $\Delta$  is an odd multiple of  $\pi$  the intensity is maximised, whenever it is an even number of  $\pi$  the intensity is zero. This can be seen in figure 6.7.

A photodiode was connected to a digital storage oscilloscope (DSO) to measure the temporal response. The SLM pixels were modulated between two voltages at the maximum speed. These voltages corresponded to a known phase shift calculated from the calibration curve. The response times are shown in table 6.4. The rise time of the liquid crystal was approximately the same for all applied voltages (2-3.5ms).

Phase shift	Time /ms
0- $\lambda/2$ (rise time)	2
0- $\lambda$ (rise time)	2
$\lambda/2$ -0 (relaxation time)	20
$\lambda$ -0 (relaxation time)	40
Fully on to fully off (relaxation time)	600
Fully off to fully on (rise time)	3.5

*Table 6.4. The response time of the Hex69.*

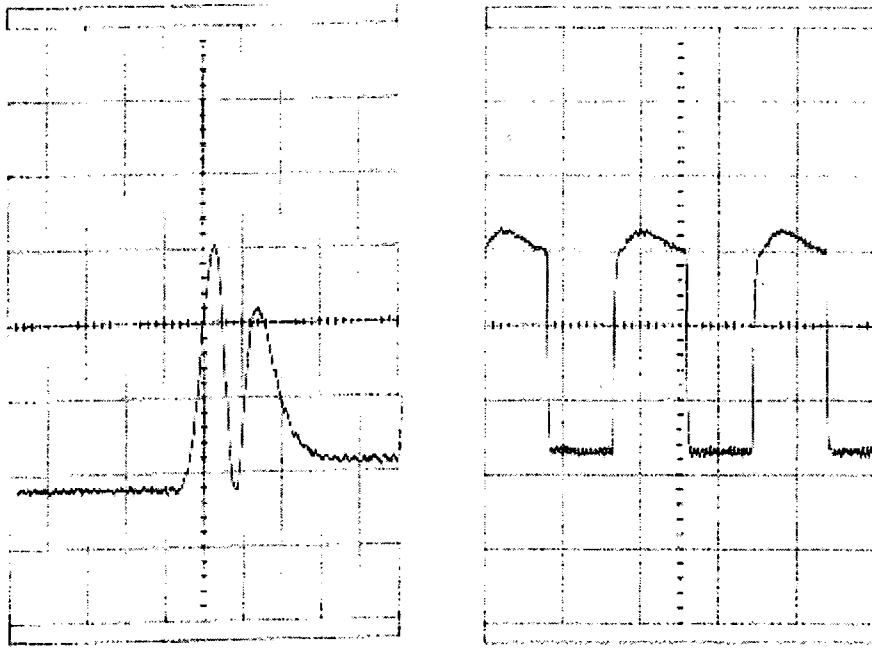


*Figure 6.7. Examples of the DSO display. The graphs are the intensity transmissions versus time of the liquid crystal when placed between polarisers at  $45^\circ$  and  $135^\circ$ . The vertical axis is the intensity measured. The left image is the Hex69 being turned from fully off to fully on. The horizontal scale is 1ms per division so it took about 3.5 ms to fully turn on the SLM. The turning points on the graph are when the birefringence of liquid crystal is equal to multiples of  $\pi$ . The right graph has a horizontal scale of 40ms per division. In this graph, the Hex69 was switched on and off at the maximum electronic frame rate of the SLM. The lowest horizontal region of the graph is the device in its on state. As the device relaxes, the intensity throughput increases until the liquid crystals birefringence is  $\pi$  and then it starts to decrease. It took 40ms for the liquid crystal to fully relax and 2ms to switch on.*

Figures 6.7 show examples of the DSO display. It can be seen that the maximum frame rate of the SLMs electronics was 38ms, however the liquid crystal did not necessarily correspond to this time. If the phase shift was greater than  $\lambda$  the liquid crystal took longer to relax than electronics' frame speed. If it was less than  $\lambda$  then the device was being limited by the drive electronics.

Clearly, if the SLM only achieves a complete phase shift of a time up to 0.6 seconds it will be limited in use for adaptive optics. The histogram in figure 6.8

shows the phase changes between successive frames of the data to be used for the ATS. It can be seen that most of the time the SLM will be limited by the drive electronics.

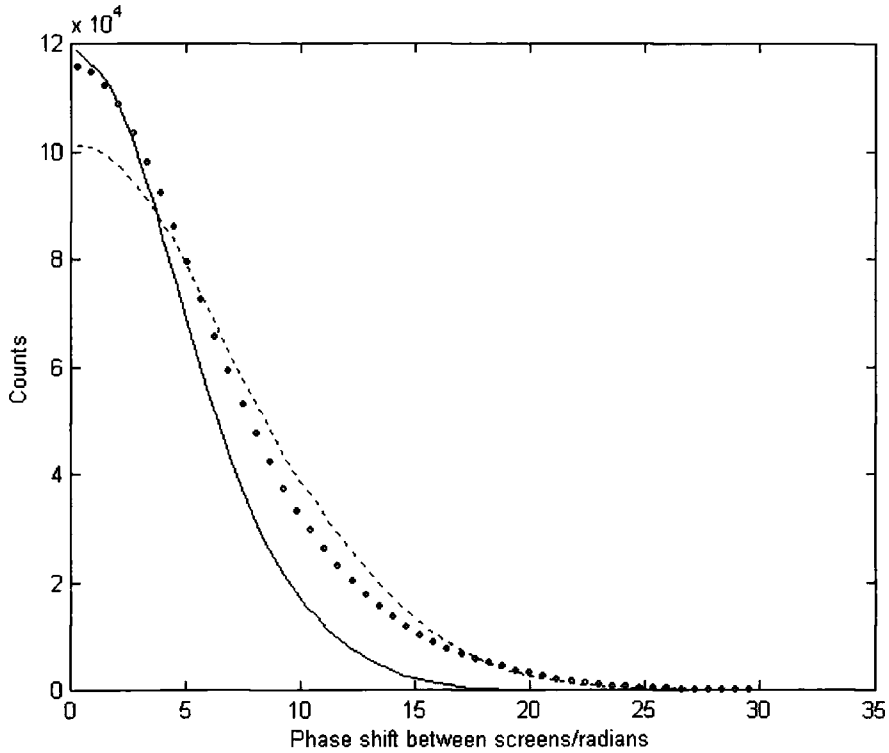


Figure 6.8. The histogram of the phase shifts between consecutive frames for different values of wind speeds. Solid line  $0.7\text{ms}^{-1}$ , dotted  $1.4\text{ms}^{-1}$ , dashed  $5.4\text{ms}^{-1}$ . Figure 6.8 is for  $D/r_0=8.5$ . In the case of  $v_w=0.70\text{ms}^{-1}$ , 84% of all the phase shifts would occur within the frame rate of the SLM. In fact 56% would be within half the frame length time. In this case, the liquid crystal material does not usually limit the ATS and so the frame rate of the device can be assumed to be limited by the electronics.

### 6.7.5 SHACK-HARTMANN SOFTWARE

As in chapter 5, the software was in two parts: the C40 DSP code and the PC code. The DSP handled the accessing of the frame buffer, handled the image grabbing and calculated the Zernike amplitudes, and returned these to the PC. The software for the DSP used the Oculus libraries supplied by Coreco and was compiled on a Texas Instruments C40 compiler. The PC software used a Microsoft C compiler.

The PC software acted as the user interface and the DSP code was only run via a function call from the PC. There were several options given when the software was first run:

1. Align system
2. Align and remove static aberrations.
3. Measure the Zernike modes
4. Measure the Zernike modes and write them to a file.

The first option was for the system alignment. The Shack-Hartmann spots were displayed on the monitor with the position of the theoretical spots and a dark spot displaying the results of the centroiding, i.e., there was a dark spot in the centre of the lenslet spot. This was a visual check to ensure the centroiding software was working correctly. The positions of the theoretical spots could be scaled and moved with the software. The camera was moved until all the Shack-Hartmann spots were aligned with the theoretical spots. Zernike aberrations were introduced onto the Hex69. Large amounts of crosstalk indicated a misalignment.

Once the system was aligned there was still some residual error. This came from aberrations in the lenslet array and imperfections in other components. Option 2 removed this by measuring 30 frames of Zernike modes and then subtracting the mean of each of these amplitudes from all subsequent measurements. If the system was disturbed in any way this option needed to be re-run.

Option 3 measured the modes and wrote them to the PC screen. Option 4 also measured the modes but wrote them to a file. It did not display anything on the PC or CCD monitors to increase the speed of the system. Figure 6.9 shows the software flow chart of the system.

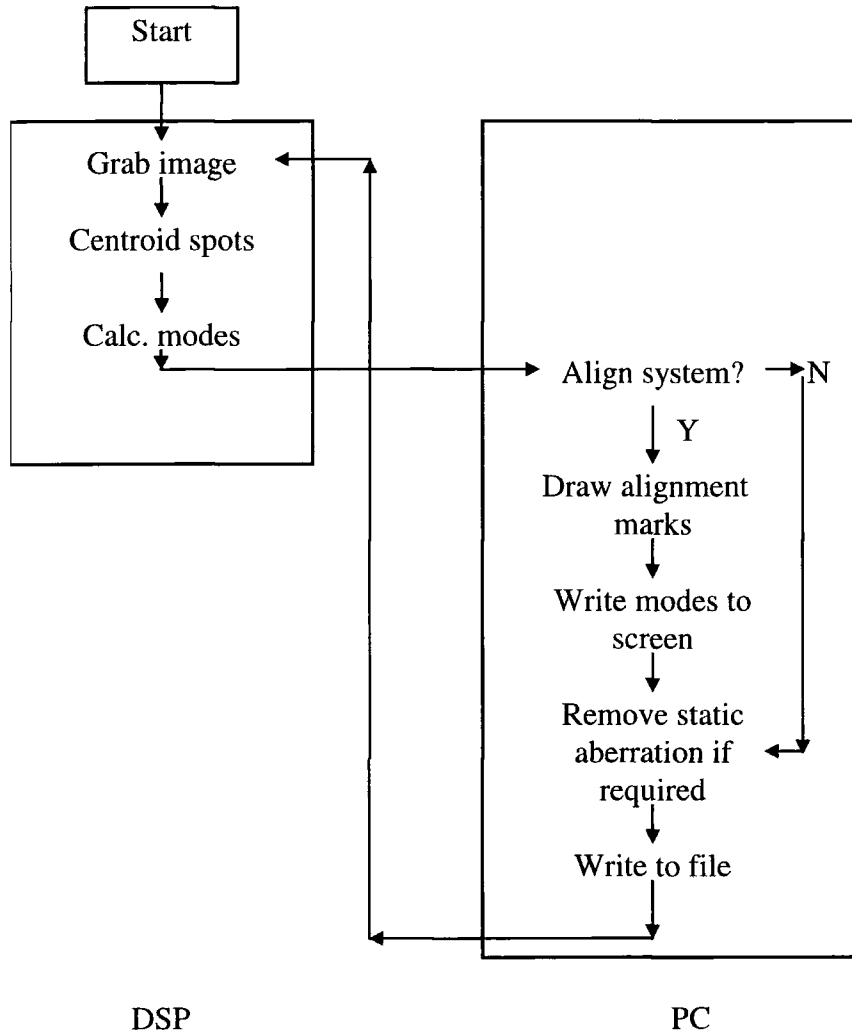


Figure 6.9. The software flowchart of the Shack-Hartmann system.

### 6.7.6 CALIBRATION OF SYSTEM

Each Zernike mode needed to be calibrated. Slight errors in the alignment and scaling of the system meant that there was a systematic inaccuracy in each mode, this needed to be calibrated out. Once the system was aligned different Zernike modes were placed on the Hex69. The first 12 modes were measured with the Shack-Hartmann. The amplitudes placed on the Hex69 were  $-0.5\lambda$ ,  $-0.25\lambda$ ,  $0\lambda$ ,

$0.25\lambda$  and  $0.5\lambda$ . By plotting these amplitudes against the measured amplitude a calibration line was calculated. This was then added to the PC software so that all future measurement would be correct.

### **6.7.7 SYSTEM LIMITS**

The Shack-Hartmann was limited in the largest aberration it could have measured by either of two factors:

1. The lenslet spots moved out of the search area.
2. The lenslet spots were diffracted by the Hex69 pixels in to more than one peak.

By drawing a box around the search area it was possible to check that the spots did not move out side the area. The search areas could have been increased as long as they did not overlap. They were however kept as small as possible to increase the speed of the centroiding.

Because the Hex69 is a pixelated device it does cause some diffraction effects. When the Shack-Hartmann spots were diffracted badly they did not centroid correctly. This placed the limit on how big the aberration could be. In practice the limit was  $\sim 0.8\lambda$  for any mode.

The smallest amount detectable was determined by the noise of the system. This came from environmental perturbations, such as vibrations or camera noise. This was measured experimentally and the mean RMS noise for all of the modes was found to be  $0.015\lambda$ . The RMS noise for each mode is shown in figure 6.10. The noise on modes 1 and 2 (tip/tilt) is larger than the rest. This is likely to come from mechanical vibrations in the optical system.

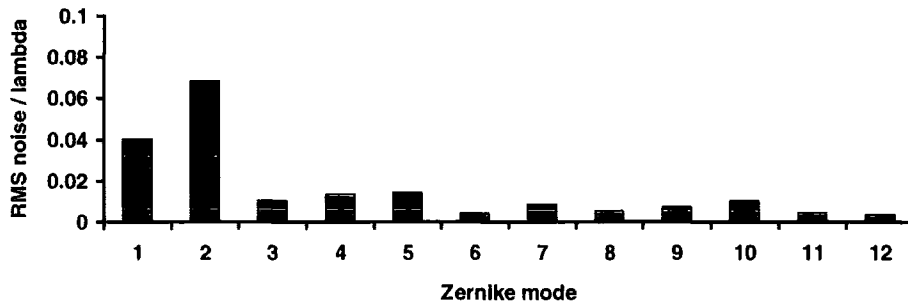


Figure 6.10. The RMS noise limit of each mode.

## 6.8 Experimental Measurements

### 6.8.1 THE ZERNIKE POWER SPECTRUM

The Zernike power spectrum was measured by placing the Hex69 into the Shack-Hartmann system. A  $D/r_0 = 8.5$  was chosen ( $r_0=10\text{cm}$ ,  $D=85\text{cm}$ ). This was large enough to give a good signal to noise ratio with the Shack-Hartmann, but not too large to cause the Shack-Hartmann spots to diffract into more than one peak. The SLM was run at the maximum frame rate of 38ms (26Hz) and the Shack-Hartmann's frame rate was 40Hz. This gave 1.5 Shack-Hartmann frames per Hex69 frame. 4252 measurements were made with the Shack-Hartmann and the 12 modes each frame generated were written to a file. The RMS for each mode was then calculated off line. This was compared to a theoretical model by Wang *et al.* (Wang, 1977). The power spectrum for the first 12 modes is shown in figure 6.11. The first two modes are zero because the tip/tilt was removed from the data.

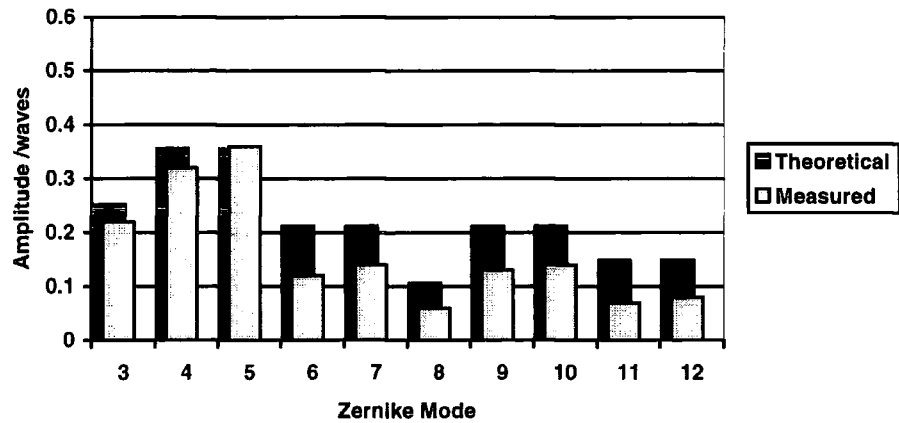


Figure 6.11. The RMS power spectrum of the ATS. This data was taken over 4552 frames.

### 6.8.2 MEASUREMENT OF TEMPORAL CHARACTERISTICS

The Zygo can not measure any temporally varying phase screen because of the time it takes to grab 5 frames in order to unwrap the phase. A conventional interferometer could, in principle, be set up with a video camera recording the interferogram in real time, but this would not address the problem of the phase ambiguity. To measure a varying phase screen one is generally left with the option of using a Shack-Hartmann wavefront sensor.

The data was taken in §6.8.1. Figure 6.12 shows the first 10 seconds of mode 3. It can be seen that there was a large variation over time and that there are no discontinuities in the data. The wind speed was  $0.70\text{ms}^{-1}$  and  $D/r_0=8.5$  ( $r_0=10\text{cm}$ ,  $D=85\text{cm}$ ). The exact value of the windspeed depended upon the value chosen for  $r_0$ . For the same value of  $D/r_0$ , but with  $r_0=20\text{cm}$ , the windspeed becomes  $1.4\text{ms}^{-1}$ .

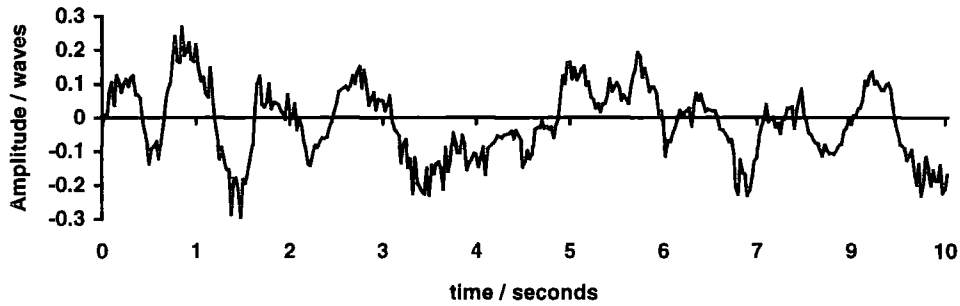


Figure 6.12. The first 10 seconds of mode 3 (defocus) data taken with the Shack-Hartmann. The Hex69 ATS provides the aberration source.

A measure of the temporal performance of the ATS can be obtained by looking at the temporal power spectrum. This should compare to the theoretical power spectrum of [3.8]. The power spectrum for the phase produced by the ATS is shown in figure 6.13. The power spectrum was calculated by taking 4252 frames of Shack-Hartmann Zernike data and converting these into phase screens. A point was selected in each screen and the data fast Fourier transformed.

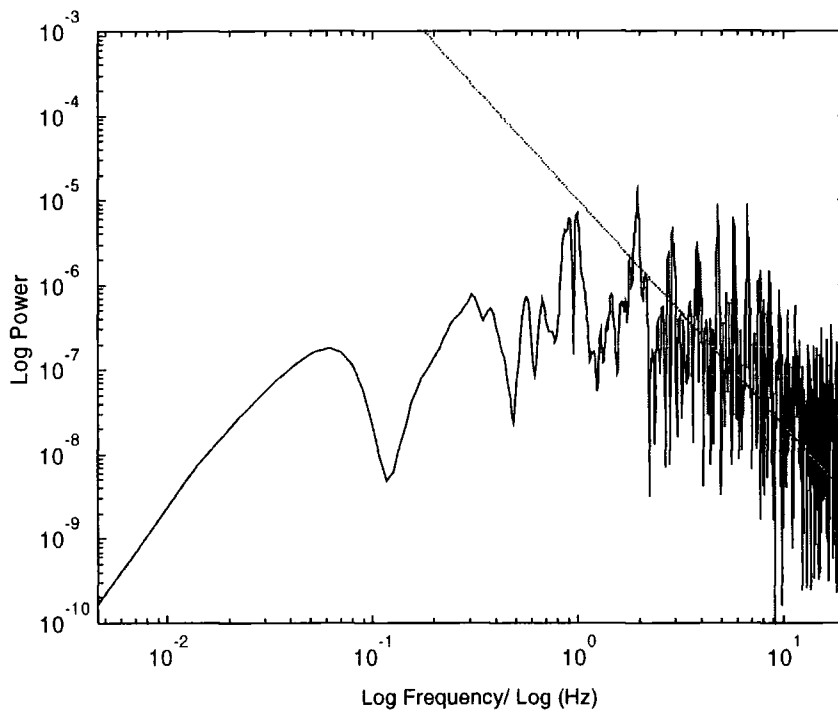
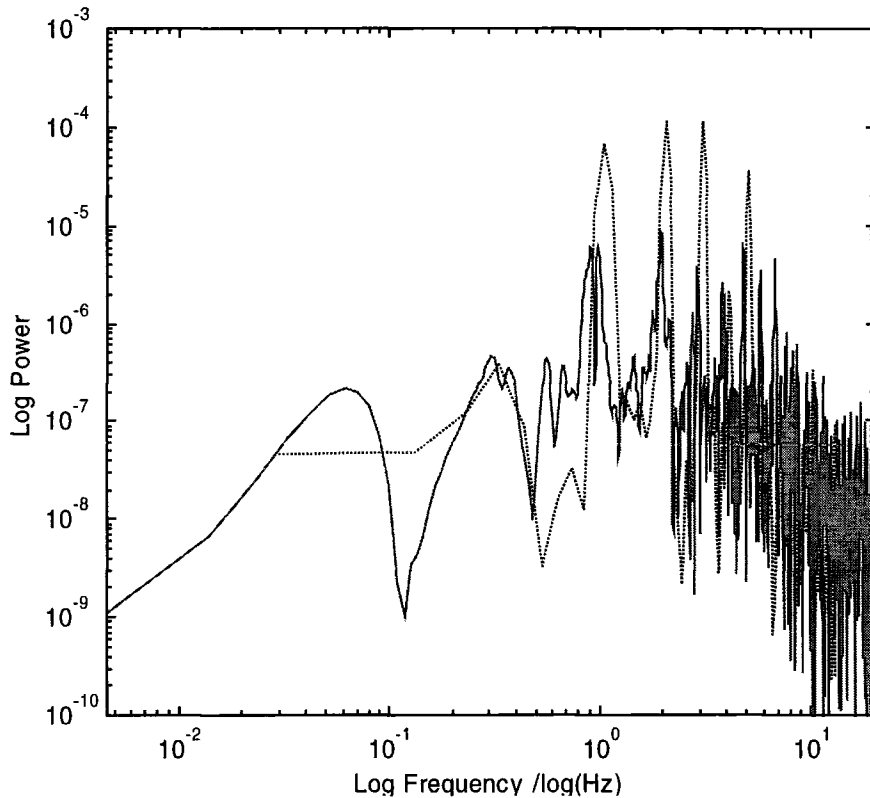


Figure 6.13. The power spectrum of the phase produced by the ATS (solid). The dotted line shows a  $-8/3$  power law.

A defocus Zernike mode was fitted to the raw data produced by the Glindemann software. The power spectrum of this raw data was then compared to the experimentally measured data produced by the ATS. Both spectrums are shown in figure 6.14. It can be seen that the high frequency gradients of the two lines follow each other reasonably closely.



*Figure 6.14. The power spectrum of the measured mode 3 (solid line) and the power spectrum of the initial data (dotted line) showing that the Hex69 accurately represents the phase data generated by the Glindemann software.*

### 6.8.3 STREHL RATIO MEASUREMENTS

Using the same data as before, the Strehl ratio produced by the ATS was measured. This was done by placing the ATS in the path of collimated light from

a red polarised He-Ne laser. This was then focused onto a CCD camera by a doublet lens. A microscope objective magnified the image of the PSF on the CCD camera's image plane. It was assumed that when no aberrations were introduced into the system the PSF was diffraction limited. The Strehl ratio was defined as being 100% at the peak intensity of this image.

The CCD camera was connected to an ITEX frame grabber. This frame grabber digitises the CCD images with 8 bit accuracy. It however, has more than one frame buffer. The ITEX board was programmed to use two frame buffers together, giving in effect a 16 bit frame buffer. It was then possible to take up to 256 8 bit images and store them in one buffer. Adding all the images together effectively gives an integrating frame store. It took 0.05 seconds (20Hz) to process a single frame. The CCD camera was running at 25Hz so some data was lost.

In the actual Strehl ratio measurement only 200 frames were used (10 seconds of data) because there was some damage to one of the frame buffers. With the ATS running, the measured Strehl ratio was 17%.

The theoretical Strehl ratio is commonly defined with equation [3.15]. This equation is only accurate for a small  $\sigma$ . To calculate the theoretical Strehl ratio the data produced by the Lane and Glindemann software was fast Fourier transformed and the mean of the 2000 PSFs was taken as the theoretical expectation. The theoretical Strehl ratio was 11%.

## **6.9 Discussion**

This chapter has developed an ATS using nematic liquid crystals and measured its performance. It can be seen from figure 6.11 that the system has approximately the correct RMS value of each Zernike mode for the  $D/r_0$  value that was modelled. The other measure of this was the Strehl ratio. Although this was slightly higher than was expected, it is possible that the discrepancy comes from the coarse pixelation of the Hex69 device.

Figure 6.13 shows a  $-8/3$  power law at high frequency for the phase shifts produced by the ATS. This is in good agreement with the expected gradient from equation [3.8].

The study in §6.7.4 showed that the liquid crystal was fast enough to reach the desired phase shift most of the time within one frame. In figure 6.14 it can be seen the SLM produces the correct amount of high frequency power. These two facts suggest that the slow speed of the liquid crystal was not limiting the ATS.

The Hex69 SLM is 9 pixels across. When an aberration with a  $D/r_0$  of 8.5 was used, each Hex69 pixel is approximately modelling one Fried length. It seems sensible to suggest that this should be the maximum aberration that should be applied to the ATS. There is no clear cut off since the drop in performance will be a sliding scale.

The wind speed the ATS was simulating was chosen to be  $0.70\text{ms}^{-1}$ . Since the maximum frame speed is fixed, the only way of increasing this speed is to skip frames, e.g., only use every second frame, effectively doubling the simulated wind speed. This has two effects: it increases the decorrelation between frames and it introduces discontinuities between frames. It can be assumed that these effects will decrease the accuracy of the ATS. It is not presently known what would be the maximum effective speed of the ATS. This will require further experimental work.

The ATS demonstrated has been shown to reasonably model the atmosphere. The device can be used in testing adaptive optics systems (in chapter 7 for example). Because of the low cost nature of the SLM it will be possible to cascade several devices, each representing a layer of turbulence. It should then be then possible to provide a good aberration source for testing multiconjugate adaptive optics.

### **6.10 Summary**

An atmospheric turbulence simulator has been demonstrated. This has many possible applications in testing adaptive optics systems. Now that an atmospheric turbulence source has been developed it can be used in the next chapter with the Shack-Hartmann wavefront sensor.

## **Chapter 7: Binary Adaptive Optics with a Shack-Hartmann Wavefront Sensor**

### **7.1 Introduction**

Chapter 5 demonstrated a binary adaptive optics system using a PDI. Although it provided good correction there were still various problems associated with the PDI. There was a low optical throughput, pixel oscillations, and the system took several frames to reach the best solution. In this chapter a more conventional wavefront sensor, the Shack-Hartmann, will be used. The ATS system developed in chapter 6 will be the aberration source.

### **7.2 Background**

Shack-Hartmann wavefront sensors have become the standard sensor in adaptive optics. They are well understood and there is a large amount of literature (see (Tyson, 1991), (Beckers, 1993) for examples). They are commercially available in 'off the shelf' packages as complete systems, with all the necessary analysis software (Ref. AOA). However, these commercially available systems are too slow for adaptive optics applications ( $\sim 1\text{Hz}$ ). It is unlikely that the Shack-Hartmann should cause the oscillations seen in chapter 5 and the complete system should also reach the correct solution in the first frame. It also has the advantage that there are many Shack-Hartmann systems already built for adaptive optics systems on other telescopes. A laboratory based system could easily be modified to use this equipment so that there would be no need to ship our wavefront sensor to a telescope. It is not unreasonable to assume that most telescopes' Shack-Hartmann cameras will work better with starlight than our laboratory camera, which was not optimised for low light.

## 7.3 Experimental System

### 7.3.1 OPTICAL SET-UP

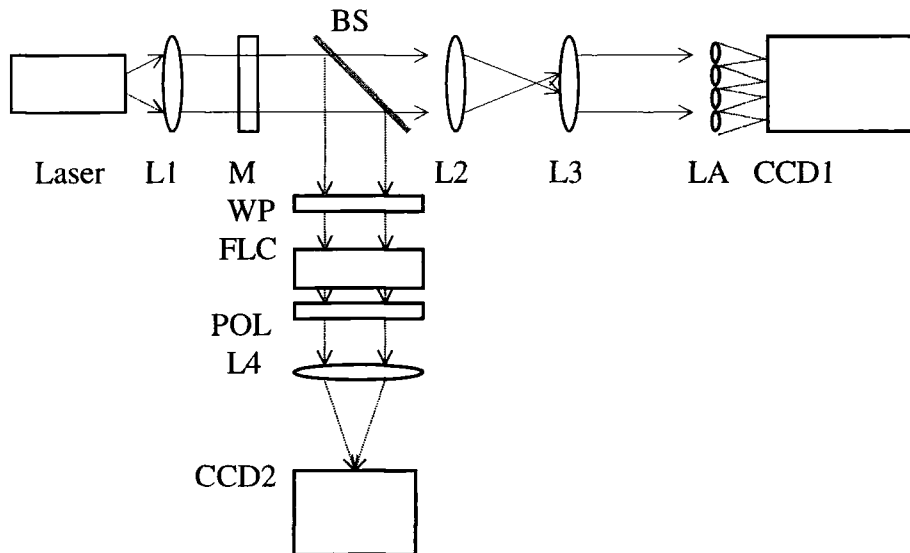


Figure 7.1. The optical set-up. L1, L2, L3, L4 are doublet lenses; M is the Hex69 SLM which was used to generate optical aberrations; WP is a half wave plate; BS is a beam splitter; FLC is the Displaytech FLC which provided the wavefront correction; POL is a polariser; CCD1 is the Shack-Hartmann CCD camera; CCD2 is the science camera; and LA is the lenslet array. L2 and L3 demagnify the beam so that the Hex69 pixels map onto the lenslet array.

The experimental system is shown in figure 7.1. The system is similar to that in chapter 6 except for the addition of the FLC system. A polarised 10mW He-Ne laser was used so that only one polariser was needed. The laser was polarised along the extraordinary axis of the Hex69. The Hex69 acted as the source of optical aberrations, the ATS. The system was in open loop because when the FLC was tried in a closed loop the inter-pixel gaps of the FLC blocked out some of the Shack-Hartmann spots. Unfortunately this made the alignment of the system considerably harder. The two lenses, L2 and L3, demagnified the beam to the size of the lenslet array, LA.

The beam splitter deflected 50% of the light through the FLC arm. The halfwave plate was required to rotate the polarisation axis round so that it bisected the two optical axes of the FLC. The polariser after the FLC was orthogonal to this axis. This light was focused on to a CCD camera which recorded the PSF.

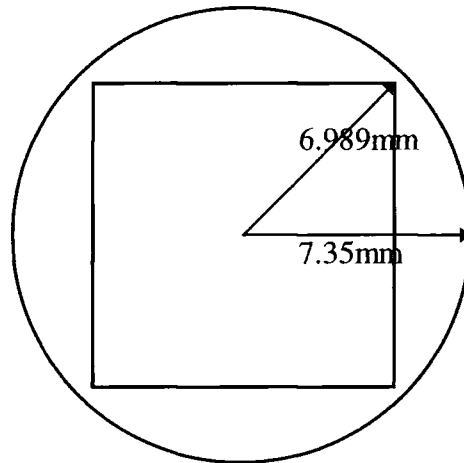


Figure 7.2. The FLC has approximately the same radius as the Hex69.

There was a slight discrepancy between the size of the FLC aperture (6.989mm maximum radius) and the size of the Hex69 (7.35mm radius). This error was small and was ignored. The FLC has a square aperture which fitted inside the Hex69s (see figure 7.2). Any light outside the FLC's aperture was absorbed and so did not effect the result.

### 7.3.2 HARDWARE DESIGN

The hardware system was similar to that described in chapter 5. The DALSA camera was however not available so it was replaced with a standard CCD camera. This was the only change to the hardware design (see figure 5.7).

### 7.3.3 SOFTWARE DESIGN

The image acquisition, spot centroiding and Zernike mode amplitude calculations were carried out by the C40 DSP (as in chapter 6). The C40 code

had to be altered to work with the CCD camera. The previous method of separating the 32 bit words in to the four 8 bit intensity values by grabbing the image and copying it into the F/64's RAM would not work. This was because the image from the CCD camera was larger than the F/64's RAM. Instead, a function call was written to access each pixel directly from the frame buffer. The other modification to be made was to the centroiding algorithm. The CCD camera did not have square pixels, but pixels with a 3:4 width:length ratio as in a TV. The position of the pixels sampled was modified to remove the biasing in one direction caused by the rectangular shape of the pixels. The CCD pixels were also smaller than the DALSA so the search box area for the centroiding had to be increased to 50x50 pixels.

The PC code was also based on the code from the last chapter. The Zernike modes were returned to the PC from the DSP as before. The system was aligned and two new options were added:

1. Correct with diagnostics
2. Correct without diagnostics

The diagnostics option caused the measured modes to be printed to the PC screen and display the position of the centroid spots on the camera monitor, as well as perform the correction of the aberrations. This only had a bandwidth of ~1Hz. Option 2 did not display any information. The bandwidth of the system was 6Hz. This is considerably slower than the similar system in chapter 6 because of the large amount of image data to process, and the slowness of accessing each pixel with a function call. If the system was not limited by the computation, the fundamental limit would of been that of the camera, 25Hz.

The correction algorithm was as follows.

1. The Zernike modes were calculated by the DSP and returned to the PC over the ISA bus.
2. Each mode was corrected with the calibration gain (that was measured chapter 6).
3. A 10x10 floating point array was created. Each element represented an FLC pixel. The phase over each FLC pixel was calculated in turn by summing the Zernike modes for that pixel, and were stored in the array.
4. The modulo  $2\pi$  of the phase in each element was calculated.
5. A second array,  $\mathbf{P}$ , containing the values to be applied to the FLC was used. It only contained the values of 0 or 1. The value of each element was determined by

$$\mathbf{P}_{x,y} = \begin{cases} 1 & \text{for } \left| \phi(x,y)_{\text{modulo } 2\pi} \right| \geq \pi / 2 \quad \text{and} \quad \left| \phi(x,y)_{\text{modulo } 2\pi} \right| \leq 3\pi / 2 \\ 0 & \text{otherwise} \end{cases} \quad [7.1]$$

where

$$\phi(x,y) = \sum_{j=1}^8 a_j Z_j(x,y) \quad [7.2]$$

where  $Z_j$  was the  $j^{\text{th}}$  Zernike function in Cartesian co-ordinates  $x$  and  $y$ , and  $a_j$  was the amplitude. The first 8 Zernike modes were used. This array was then changed to the correct format and was passed to the FLC drive electronics through the printer port. In the next frame, and every second frame afterwards, the results from equation [7.1] were inversed (i.e., passed through a NOT function). This ensured that the driving electric field of the FLC was AC, and stops the liquid crystal molecules degrading. The use of an AC field has no effect on the correction. In binary adaptive optics there is no absolute piston term in the phase, so it is impossible to define which part is in phase and which part is

out. The addition of  $\pi$  radians to a pixel in frame 1 is equivalent to the addition of  $-\pi$  in frame 2. When using an FLC, one is only concerned with the phase difference between on and off pixels not the absolute phase.

### **7.3.4 OPEN LOOP CONSIDERATIONS**

The Shack-Hartmann lenslet array used in this system had a hexagonal format. There was therefore, a mismatch between the sampling area of the lenslet and the FLC pixel areas. The interpixel gaps also posed problems by interfering with the spots when the FLC was placed in front of the lenslet array. For this reason the device was run in open loop. This presented two problems to be overcome.

1. There was no feedback. If the device were in a closed loop the system would always tend towards the correct solution even if the calibration was not accurate. In an open loop system the lack of feedback means that any error in the measurement will not be corrected.
2. The alignment of the system was more difficult. Because of the lack of feedback there was no easy way of testing if the system was correctly aligned. In a closed loop system, an aberration could be applied to the FLC and measured with the Shack-Hartmann. This would have also ensured that the FLC was orientated correctly, i.e., it was not back-to-front, upside down, or rotated, etc.

However, the lack of feedback was not critical once the system was aligned because of the binary nature of the system. It was expected that any phase measurement errors would be less than  $\pi$  radians. Any additional accuracy was not needed in this system.

### 7.3.5 ALIGNMENT

The Hex69 was easier to align than the FLC. Zernike modes could be applied to the Hex69 and these were measured with the Shack-Hartmann. Any rotational misalignments (in units of  $90^\circ$ ) could be corrected in the Shack-Hartmann software, for example, if Zernike mode 1 was applied but only mode 2 was measured this could be corrected by changing the order of the modes in the software.

The alignment of the FLC was much more difficult. This was done by taking advantage of the liquid crystal SLMs' birefringence. By using polarisers at the correct angles, the SLMs were used as intensity modulators. The steps involved applying a Zernike mode, such as astigmatism, to the Hex69. This was measured with the Shack-Hartmann and this measured amplitude was also applied to the FLC. A polariser at  $45^\circ$  to the Hex69's optical axis was then placed before the Hex69, and one at  $135^\circ$  was placed after. This made the SLM an intensity modulator. The orientation of the Zernike mode on the FLC was then checked in a similar manner. This was repeated for all modes. The magnification of the system can be checked with defocus. A defocus mode applied to the FLC should produce a dark ring. The Hex69 and FLC have slightly different sizes so the scale factor in the software was altered to compensate for this.

### 7.3.6 PREDICTED PERFORMANCE

The FLC used in this chapter is the same as in chapter 6, so it suffered from the same problems of having a small number of pixels. The expected performance of the system can however be calculated. The wavefront error after correction depends on several factors. Let  $\sigma^2$  be the residual wavefront error after correction. This is calculated from

$$\sigma^2 = \sigma_{\text{WFS}}^2 + \sigma_{\text{corr}}^2 + \sigma_{\text{Zem}}^2 + \sigma_{\text{temp}}^2 \quad [7.3]$$

where  $\sigma_{\text{WFS}}$  is the wavefront sensor error,  $\sigma_{\text{corr}}$  is the fitting error of the wavefront corrector,  $\sigma_{\text{Zem}}$  is the residual error from the high order Zernike modes not corrected, and  $\sigma_{\text{temp}}$  is the error from the finite speed of the system.

An estimate for the wavefront sensor error can be derived from the measurements of the Shack-Hartmann noise. The contribution for each mode's noise to the total variance was calculated. Software was written to calculate the phase at 100 points, corresponding to each FLC pixel. The variance in phase was then calculated from the noise at these discrete points. This was calculated to be 0.0013 radians<sup>2</sup>.

It is not possible for any deformable mirror or liquid crystal SLM to completely match the aberrations produced by the atmosphere. There will always be some wavefront error after correction from the corrector's inability to completely fit the wavefront. Hudgin (Hudgin, 1997) developed a formula for the fitting error given by

$$\sigma_{\text{corr}}^2 = \alpha \left( \frac{r_s}{r_0} \right)^{5/3} \quad [7.4]$$

where  $r_s$  is the distance between actuators and  $\alpha$  is called the *fitting parameter*. He calculated various values for  $\alpha$  with different types of mirror. For a Gaussian response  $\alpha=0.28$ , for a pyramidal response  $\alpha=0.23$  and for a piston only response,  $\alpha=1.26$ . The FLC can be considered to behave like a piston only mirror so  $\alpha=1.26$  was chosen, however there is also an additional fitting error from the FLCs binary operation. If we consider some phase function over the aperture,  $\phi(\mathbf{x})$ , where  $\mathbf{x}$  is the two dimensional vector, in binary adaptive optics we are only concerned with  $\phi(\mathbf{x})$  being in the range of 0 to  $2\pi$  radians. For a (large) normal random distribution, after correction the mean phase is  $\bar{\phi}(\mathbf{x})=\pi/2$

and  $\phi(\mathbf{x})$  can vary from 0 to  $\pi$  radians. The variance wavefront error from the FLC,  $\sigma_{\text{FLC}}$ , is

$$\begin{aligned}\sigma_{\text{FLC}}^2 &= \left\langle [\phi(\mathbf{x}) - \bar{\phi}]^2 \right\rangle & [7.5] \\ &= 0.824 \text{ radians}^2\end{aligned}$$

This assumes that  $\phi(\mathbf{x})$  varies uniformly between 0 and  $2\pi$ . Since the FLC can be considered to have a piston response with a residual error given by [7.5], the total value for  $\sigma_{\text{corr}}$  is

$$\sigma_{\text{corr}}^2 = 1.26 \left( \frac{r_s}{r_0} \right)^{5/3} + 0.824 \quad [7.6]$$

for  $D/r_0 = 8.5$  and  $D/r_s = 10$  for the FLC, [7.6] equals 1.785 radians<sup>2</sup>.

The wavefront error from the limited number of Zernike modes corrected is given by Noll (Noll, 1976). If the first eight modes are corrected (see table 3.3)

$$\begin{aligned}\sigma_{\text{Zern}}^2 &= 0.0463 \left( \frac{D}{r_0} \right)^{5/3} & [7.7] \\ &= 1.639 \text{ radians}^2\end{aligned}$$

There was also an error from the finite speed of the corrector system,  $\sigma_{\text{temp}}$ . Tyson (Tyson, 1991) shows that

$$\sigma_{\text{temp}}^2 = \left( \frac{0.4v}{r_0 f_c} \right) \quad [7.8]$$

where  $v$  is the wind velocity (taken as  $5\text{ms}^{-1}$ ) and  $f_c$  is the bandwidth of the system. If  $f_c=40\text{Hz}$  and  $r_0=10\text{cm}$ , [7.8] equals  $0.5\text{ radians}^2$ .

For  $D/r_0=8.5$ , the uncorrected variance is  $4.7\text{ radians}^2$  (with tip/tilt removed). The total expected residual wavefront error after correct has been calculated as  $3.92\text{ radians}^2$ .

## **7.4 Results**

The correction performance was measured in terms of Strehl ratio. The PSFs were measured with the CCD 2 camera (figure 7.1). This was used in conjunction with the ITEX integrating frame grabber (see chapter 6).

### **7.4.1 STATIC CORRECTION**

An example of static correction is shown in figures 7.3, 7.4 and 7.5. An aberration was applied to the Hex69. The uncorrected PSF is shown in figure 7.4, the Strehl ratio was 30%. The corrected PSF is shown in figure 7.5, with a Strehl ratio of 48%. This is an improvement in a factor of 1.6. Figure 7.6 shows the actual PSF images.

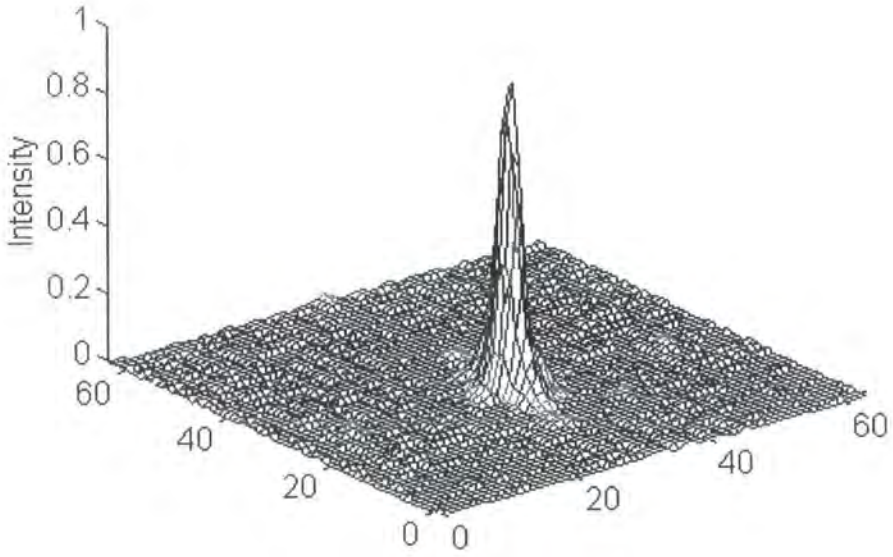


*Fig 7.3 The unaberrated PSF.*

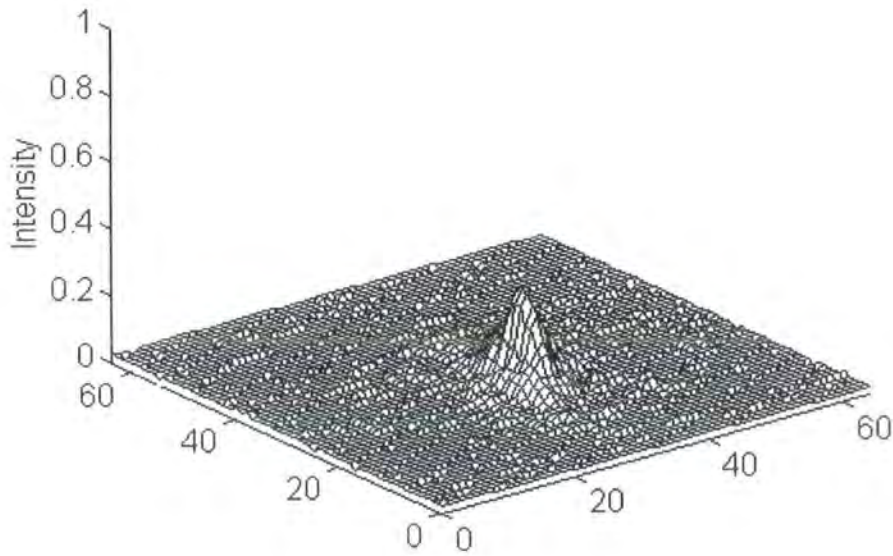


*Figure 7.4. The aberrated PSF. The Strehl ratio was 30%.*

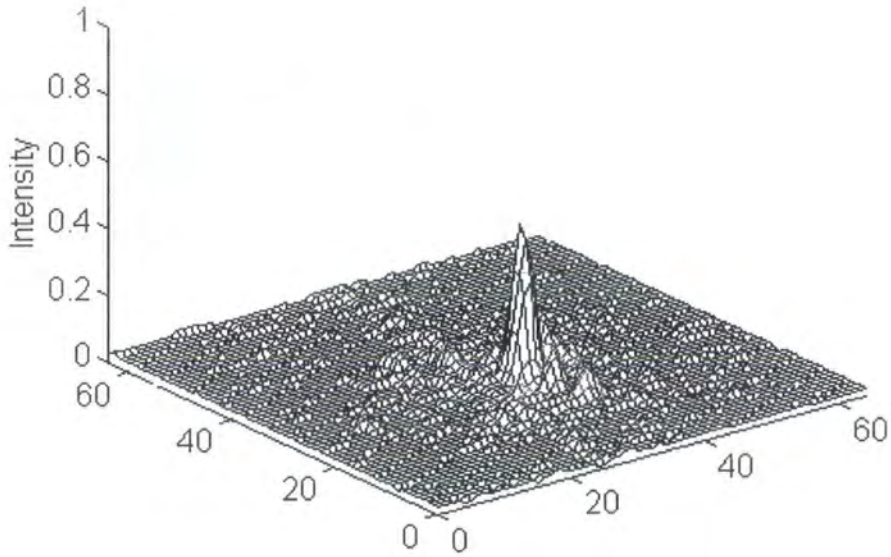


Figure 7.5. The corrected PSF. The Strehl ratio was 48%

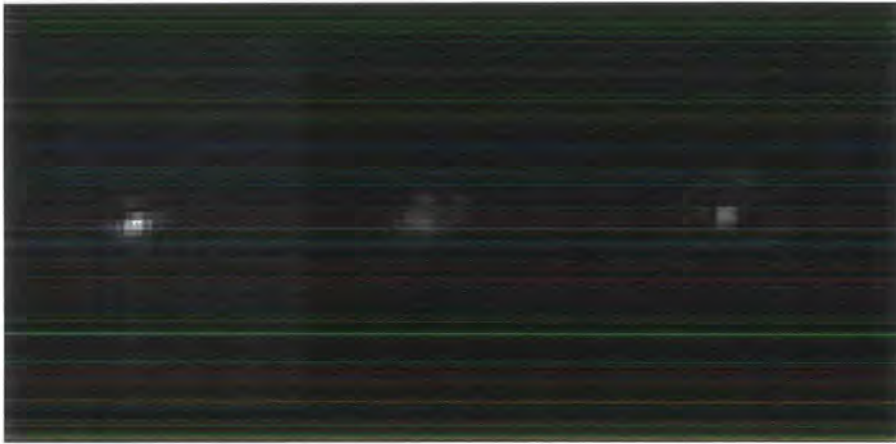
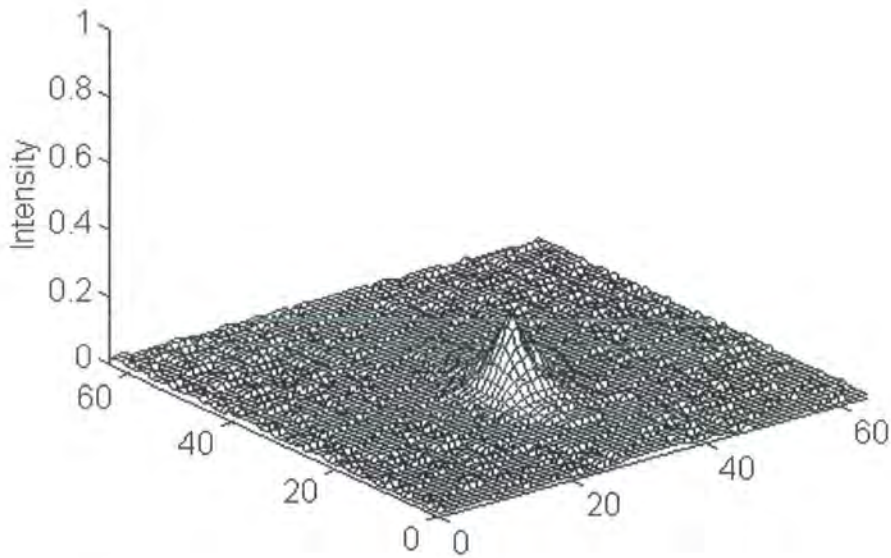


Figure 7.6. From left to right, the unaberrated, the aberrated and the corrected PSFs.

#### 7.4.2 REAL TIME CORRECTION

The ATS system developed in chapter 6 was used as the aberrator for the real time correction system. The phase data was scaled to give a  $D/r_0$  of 8.5. Because of the slow speed of the Shack-Hartmann (6Hz) the wind speed was reduced to

an unrealistically slow speed ( $\sim 1\text{ms}^{-1}$ ). The following PSFs were taken with the ITEX integrating frame grabber over 200 frames (10 seconds). Figure 7.7 shows the aberrated PSF, figure 7.8 shows the corrected PSF. The images are shown in figure 7.9. The uncorrected Strehl ratio is 23%. The corrected Strehl ratio is 33%. A 43% (0.7 fold) increase in the Strehl ratio (compared to a 420% for the PDI/FLC system).



*Figure 7.7. The aberrated PSF. The Strehl ratio was 23%.*

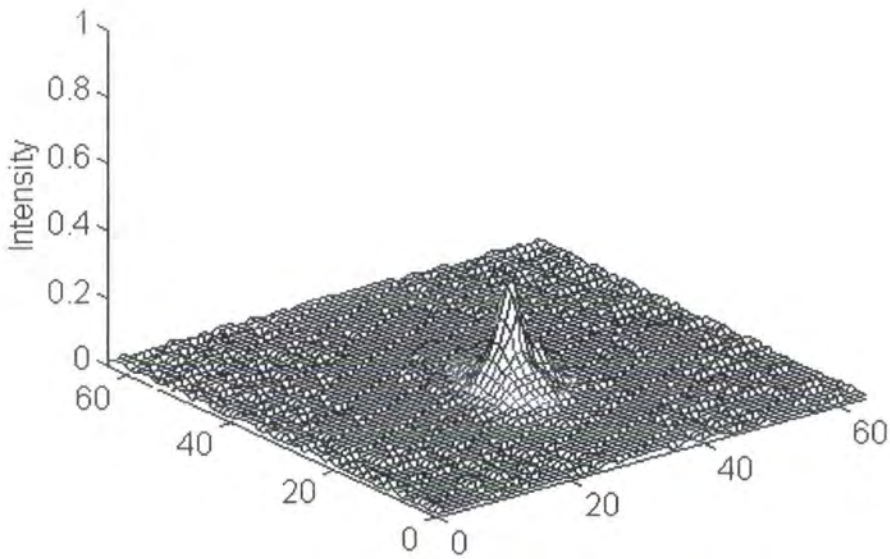


Figure 7.8. The corrected PSF. The Strehl ratio was 33%.

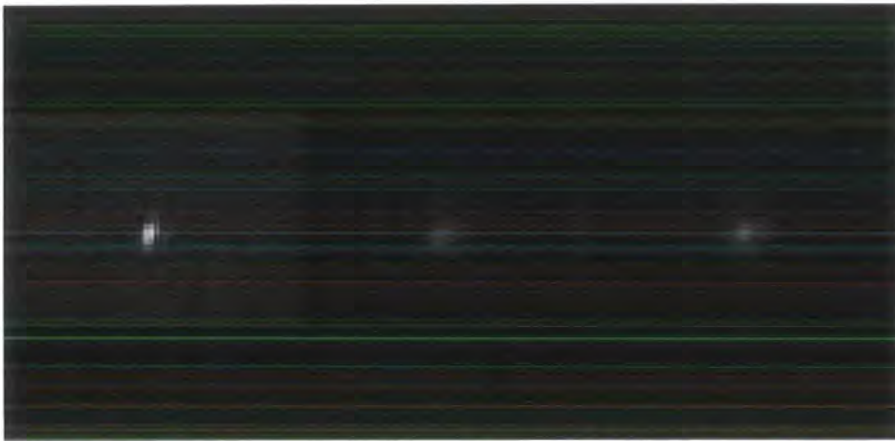


Figure 7.9. From left to right: the image of the unaberrated PSF, the aberrated and the corrected.

### 7.5 Discussion

Another working, low cost, adaptive optics system has been demonstrated. It shows partial correction at a speed of 6Hz. The wavefront sensor currently limits the speed of the system. It should be possible to replace the CCD camera used in

this experiment with the high speed DALSA camera. There is no reason why this system should not then work at the frame rate (40Hz) of the Shack-Hartmann used in chapter 6. The drop in the frame rate was because of the camera's lower speed (25Hz) and large number of pixels to process (768 by 575 compared to 128 by 128 for the DALSA). The Shack-Hartmann system has been tested on a 200MHz Pentium system with the DALSA camera; the frame rate of the system was then increased to 60Hz. At such frame rates the device is approaching speeds that would be useful in astronomical applications.

In common with the FLC/PDI system in chapter 5, the transmission of the FLC is prohibitively low for astronomical applications (2%). However, this system does have the advantage of having a more light efficient wavefront sensor. The Shack-Hartmann camera was not optimised for low light conditions but such systems are in use on telescopes.

A method of improving the transmission of the FLC would be to operate it at a different wavelength so that its retardance was  $\pi$  radians. The theoretical transmission of the SLM and the two polarisers (excluding absorption and reflections) would then be 50%. The Meadowlark polariser used in this experiment has a quoted transmission of 42% in unpolarised light, or an 8% loss in polarised light. The expected transmission with the two polarisers and the FLC with a retardance of  $\pi$  would then be 33%. Although lossy, it is considerably better than the measured value used in this experiment. The wavelengths that give  $\pi$  radians retardance for this device are 383nm (in the UV) or 1659nm (in the IR). However, if UV light was used the atmospheric turbulence would be more severe, and the transmission characteristics of the device are not known at either of these two wavelengths.

The measured correction was lower than the possible increase in Strehl ratio to 40.5%. Part of this performance drop has been quantified in equation [7.3]. There was always some residual error because of the finite capabilities of the

system. From [7.3] it can be seen that the greatest contribution to this comes from the  $\sigma_{\text{corr}}$  term given by equation [7.6]. In binary adaptive optics there will always be the 0.824 factor, however the left hand part of [7.6] (i.e., [7.4]) still contributes 0.96 radians<sup>2</sup>. A modest increase in the number of pixels to say 15 by 15 would reduce this number by a half.

The other major quantifiable contribution to the error in correction is from the number of Zernike modes used to describe the wavefront. Completely correcting the first eight modes still leaves a wavefront variance of 1.639 radians<sup>2</sup>. This is a large fraction of the total residual error and is much larger than the error from the finite speed of the system. If the system was to be operated with the high speed DALSA camera it is clear that more Zernike modes should be calculated even at the expense of system speed. If we consider the frame speed of the system to be 40Hz, the variance of the system from the temporal residual error is 0.5 radians<sup>2</sup> (from [7.8]). For  $\sigma_{\text{Zern}}^2$  to equal this requires the first 34 modes to be corrected (from [3.14]). There is clearly some room in the future for the optimisation of the system by balancing the number of modes calculated with the frame speed of the system. It should be noted that because only 19 lenslets are used, only the first 38 modes could be calculated. Redesigning the optics could increase this, but the Hex69 could then no longer be used as the ATS.

The other possible source of error is from misalignment of the optics. The exact contribution this causes is difficult to quantify. The most likely source of error comes from the positioning of the FLC in the system. The exact alignment is difficult because of the small size of the pixels. In the worse case, the FLC could be out of alignment by one pixel. This could cause the Strehl ratio to decrease when correction was attempted.

Using the FLC with a Shack-Hartmann has several advantages over the Smartt PDI system in chapter 5. The Shack-Hartmann has a considerably higher light efficiency. Except for losses from absorption by the glass components there is no

attenuation with the Shack-Hartmann system. The number of photons required by a Shack-Hartmann is well documented (Cao, 1994).

Because of the system's open loop nature there were none of the pixel oscillations that were seen with the PDI system, and the solution is found in the first frame. This means that the wavefront sensor does not have to be operated as fast as the PDI sensor for a given aberration. This also improves the overall light efficiency of the system.

When used in binary adaptive optics the Shack-Hartmann actually provides more information than is needed. In binary adaptive optics the only information needed is whether a pixel is in or out of phase relative to another pixel. However, using the Shack-Hartmann means that the system is easily modified for quarter wave correction. This is impossible with the PDI system in chapter 5, unless a phase shifting PDI is used. Since these devices rely on nematic liquid crystals, they will always be slow compared to what can be achieved with a Shack-Hartmann.

To achieve quarter wave correction with FLCs for astronomy, devices with higher switching angles will have to be developed. When used with polarisers, FLCs have too low a transmission for astronomical applications. Assuming that a high switching angle FLC would have a similar transmission to the Displaytech FLC, two cascaded together to give quarter wave switching would have a transmission of  $\sim 0.8^2 = 64\%$ , which is still low but usable.

With quarter wave switching it is expected that the Strehl ratio improvement in an experiment similar to one in this chapter would be better. The maximum correction achievable from a binary corrector is 40.5%. It is unlikely that FLCs will ever compete with deformable mirrors unless used as at least quarter wave correctors. This would enable correction up to a Strehl ratio of 81%.

With quarter wave correction [7.6] becomes

$$\sigma_{\text{corr}}^2 = 1.26 \left( \frac{r_s}{r_0} \right)^{5/3} + 0.206 \quad [7.9]$$

If we define a system to be well corrected when  $\sigma^2 \leq 1$  radians<sup>2</sup>. This happens when  $r_s \leq 0.75 r_0$ . To achieve a Strehl ratio of 80% we require  $r_s = 0.08 r_0$ .

Like in chapter 5, the system is limited by transmission. Assuming this problem could be addressed the next stage of constructing a future system would be to improve the frame speed of the system and calculate more Zernike modes. The system could then be tried on a real telescope.

Until high switching angle FLC materials are developed, it is unlikely that FLCs will be of much use in astronomical adaptive optics systems. At present, nematic liquid crystal SLMs have two major advantages: their high transmission and the ability to fully correct an aberration.

## **7.6 Summary**

In this chapter an FLC adaptive optics system with a Shack-Hartmann wavefront sensor has been constructed. The real time speed was limited to 6Hz due to equipment problems but an increase in the Strehl ratio from 23% to 33% was measured. This was a real time measurement over a period of 10 seconds.

It has been demonstrated in this chapter (and chapter 5) that an FLC does provide partial correction in real time. However, their limited throughput makes them unsuitable for atmospheric systems at present. For this reason the next chapter will describe a nematic liquid crystal SLM which will be used as the corrector. Although nematic liquid crystals have a slower speed they have a far higher transmission and perform complete analogue correction.

## Chapter 8: Nematic Liquid Crystal Correction

### 8.1 Introduction

In the previous chapters partial correction by binary adaptive optics was demonstrated using an FLC SLM. It was demonstrated that, although some correction is performed, the actual Strehl ratio increase is quite low. This is because of the low maximum theoretical performance (40.5%), compounded by the low number of pixels. For most applications it would be desirable to completely correct the wavefront. This enables the Strehl ratio to be completely restored and is the usual technique used in adaptive optics with deformable mirrors. Full correction is possible, in principle, with nematic liquid crystals where the phase modulation is analogue. (The nematic liquid crystal SLM could also be used as a binary corrector but offers no real advantage except for its potentially higher transmission- 50%, or 100% if two devices are cascaded). The disadvantage of using nematic devices are their lower speeds.

For a complete correction it is necessary to completely calculate the wave front. Both the Zygo interferometer and the Shack-Hartmann wavefront sensor are suitable for this. The Zygo can only be used to correct for static aberrations, but it does provide a complete wavefront analysis more accurately than the Shack-Hartmann and can be used as either a zonal or modal wavefront sensor.

### 8.2 Background

Several authors have discussed the possibilities of using nematic liquid crystals as correction elements (Bonaccini, 1991), (Dou, 1995), (Love, 1997), (Bold, 1997), (Amako, 1993). As with the FLC SLM adaptive optics experiments so far, these have been static. Nematic liquid crystal SLMs can be thought of as similar to segmented mirrors with piston only actuators. Liquid crystal SLMs have the potential for having a larger number of pixels compared to current segmented

mirrors, but segmented mirrors are typically driven with three actuators giving movement in the direction of tip, tilt and piston. This gives them three degrees of freedom per pixel/mirror compared to one degree for a nematic liquid crystal SLM pixel. This has been addressed with computer simulations by Bonaccini *et al.* (1991). Their model suggested that to get a good correction (Strehl ratio  $\geq 0.8$ ) 26x26 nematic SLM pixels are needed, whereas only 10x10 tip/tilt/piston actuators are needed for a  $D=3.5\text{m}$  and  $r_0=0.4\text{m}$  ( $D/r_0=8.75$ ).

### **8.3 Device Description**

The nematic SLM used in this chapter was the Meadowlark Hex69. A full description of the device is given in §6.5.

#### **8.3.1 DRIVING SOFTWARE**

To control the device three programs were used. The first two were for static control of the device. These programs could either control individual pixel values or added Zernike modes. The third was a modified version of the Shack-Hartmann software used in §6.7.5 and §7.3.3 and was used to perform the real time correction. This program is described below.

### **8.4 Static Correction**

To assess how well the Hex69 can shape wavefronts static corrections are useful. The wavefront measurements were done with the Zygo interferometer. The Zygo produced a data file containing 196 by 226 data points. To locate the Hex69 pixels on the interferogram a map file was generated. This was done by setting the voltages of all the Hex69 pixels to 0V and increasing one pixel until there was a dark fringe on the pixel in the Zygo's display screen. This interferogram was saved to disk and the process repeated for all the Hex69 pixels. The 69 files were then thresholded to determine where the dark pixel was. A calibration file

was then produced containing the position of each Hex69 pixel on the interferogram. This is shown in figure 8.1

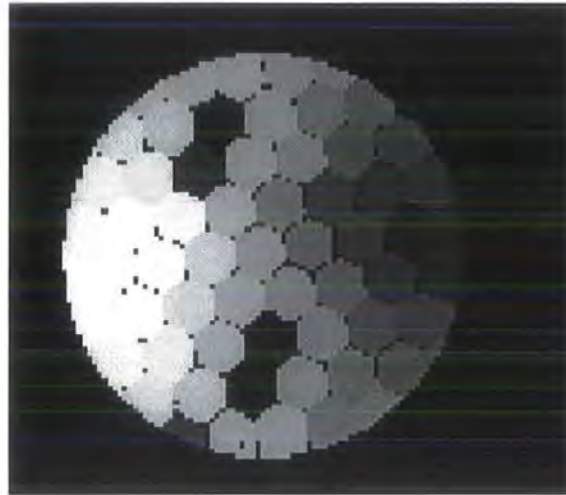


*Figure 8.1. A grey scale representation of the calibration map file.*

Using this map file it was then possible to calculate the phase over any given Hex69 pixel from the Zygo, providing the Hex69 was not moved.

An aberrating piece of glass was placed in front of the Hex69 in the Zygo system (see figure 8.2). The phase screen was then measured with the Zygo. This file was saved and the required phase shift for each pixel needed to correct the aberration induced by the glass was calculated off line. The Zygo calculated the Strehl ratios before correction and after correction by Fourier transforming the phase data. The improvement is shown in table 8.1. The aberrated and corrected wavefronts are shown in figure 8.3 and in figure 8.4.

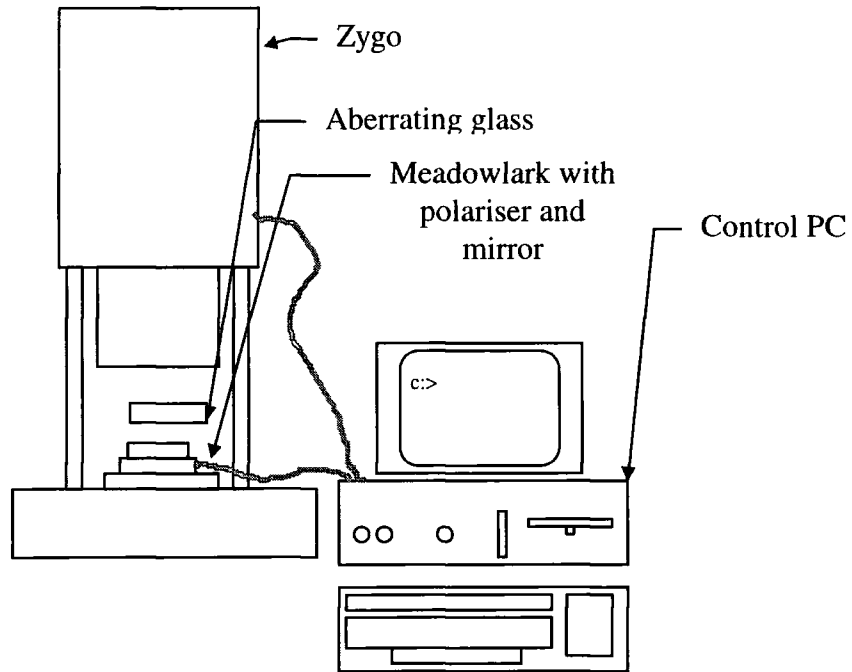


Figure 8.2. The Hex69 in the Zygo interferometer. The Hex69 is mounted on top of an optically flat mirror and a high quality polariser is placed on top of the Hex69. A PC controls both the Hex69 and the Zygo, however the correction is not real time.

Parameter	Uncorrected	Corrected
Strehl ratio	63.3%	96.6%
RMS wavefront error	0.11 $\lambda$	0.029 $\lambda$
Peak to valley wavefront error	0.48 $\lambda$	0.2 $\lambda$

Table 8.1. The results from correcting a piece of aberrating glass with the Hex69 and Zygo.

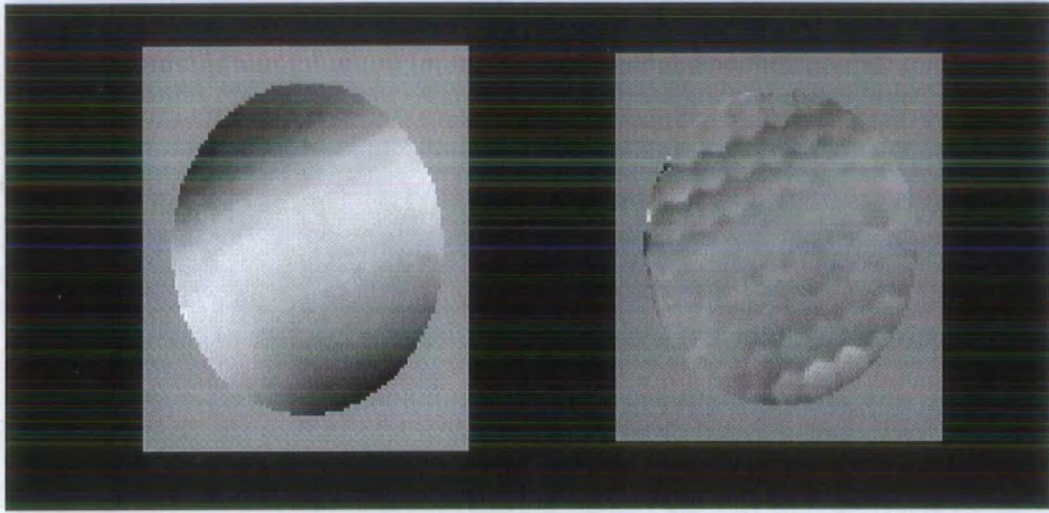


Figure 8.3. The left is the uncorrected phase map of a piece of glass. The right is the corrected phase map by the Hex69. The pixelation of the Hex69 is clearly visible.

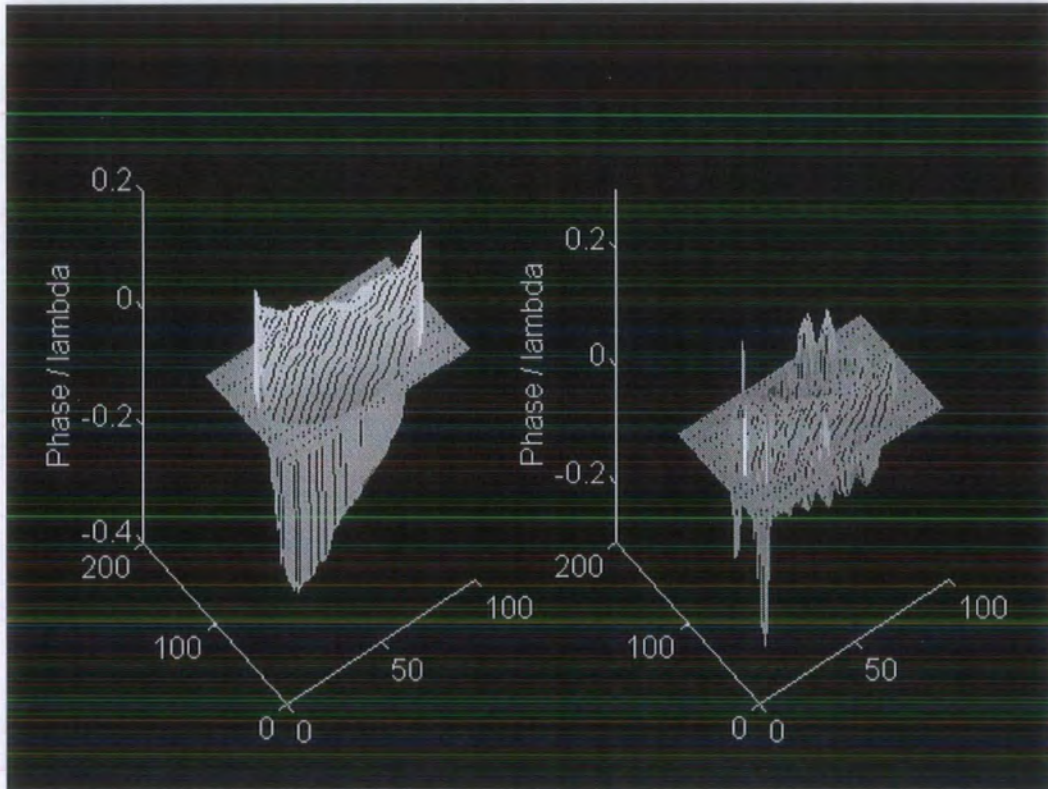


Figure 8.4. The left graph is the uncorrected phase graph. The right graph is the corrected. The sharp peaks on the corrected phase graph are from bad data points measured by the Zygo. Ignoring these points will greatly improve the peak to valley measurement.

The Zygo takes about 20 seconds to process the data and the whole process takes of the order of a minute so this is in no way a real time system. It does demonstrate the correction ability of nematic liquid crystal SLMs.

#### 8.4.1 STATIC ZERNIKE CORRECTION

To access how well the Hex69 could correct for simulated data, Zernike modes were added to the raw measured data with the Zygo. Using this it was possible to add imaginary aberrations into the system. The Zygo added various Zernike modes to the data and the software attempted to correct them. This was really a measurement of how well the Hex69 could generate Zernike modes using the Strehl ratio as a measure of performance.

Various Zernike mode amplitudes were added into the data and the Hex69 attempted to correct for these. The Zygo measured the mode applied to the Hex69 and added the software data to this. If the two were exactly conjugate the Zygo should measure a flat wave and the Strehl ratio would be restored to 100%. The before and after Strehl ratios are shown in figure 8.5 for an amplitude of  $\lambda/4$  and figure 8.6 for an amplitude of  $\lambda/2$ . The corrected Strehl ratios in figure 8.5 are all above 90% (except mode 8), so the residual wavefront variance is less than 0.3 radians. In this case the Strehl ratio is defined as being the ratio of the measured and diffraction limited intensities at the DC term. This is so that the performance of correcting tip and tilt could be assessed.

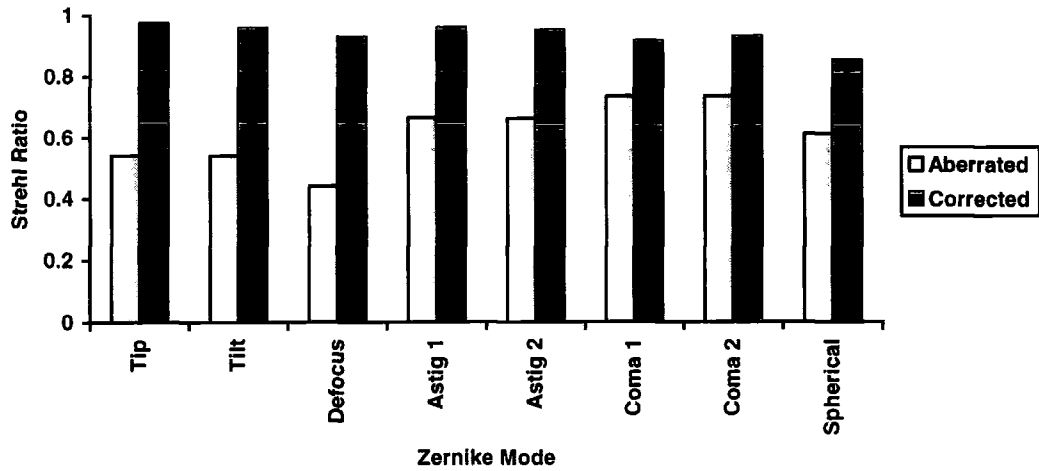


Figure 8.5. The aberrated and corrected Strehl ratios from simulated data. The amplitude of the Zernike modes was  $\lambda/4$

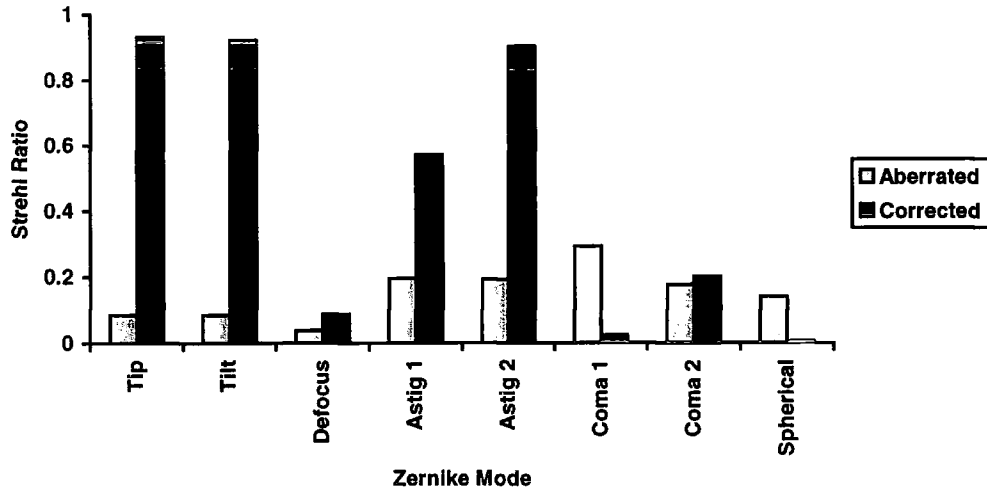


Figure 8.6. The aberrated and corrected Strehl ratios from simulated data. The amplitude of the Zernike modes was  $\lambda/2$ . Defocus, astigmatism 1, coma 1 and 2 and spherical are incorrect because the Zygo could not measure the aberration produced by the Hex69 due to the coarse pixelation so no reliable results were possible for these modes at this amplitude.

In figure 8.6 the limitation of the correction was not the Hex69, but the Zygo's difficulty in measuring coarsely pixelated wavefronts.

### 8.4.2 MODAL CROSSTALK MEASUREMENTS

Zernike modes of various amplitudes were applied to the Hex69. These were measured with the Zygo. The Zygo fits Zernike modes to the data by using a least-square-fitting algorithm. The measured modes are shown in figures 8.7 to 8.15. They were also measured with the Shack-Hartmann in §8.5.3. It can be seen that there was considerable crosstalk between certain modes. This happens between similar modes, that is, between a low order mode and its higher order equivalent. This can be clearly seen when  $0.25\lambda$  of spherical aberration (mode 8) was applied and  $-0.11\lambda$  of defocus (mode 3) and  $-0.14\lambda$  of high order spherical (mode 15) was measured. Only  $0.11\lambda$  of mode 8 was measured. This problem is reduced when lower amplitude aberrations are applied. When using the Hex69 as a corrector this becomes less of a problem because the effect is mainly seen in higher order modes. The actual typical amplitudes of the higher order modes are not as big as the low order modes in atmospheric turbulence.



Figure 8.7. The Zernike power spectrum of a tilt aberration introduced by the Hex 69 of amplitude  $0.25\lambda$ .

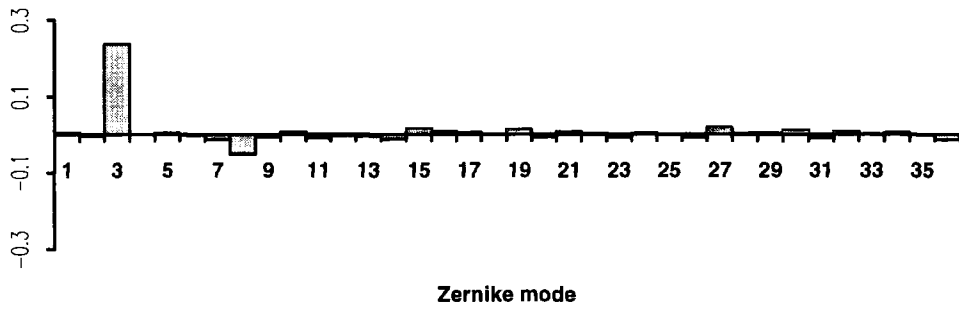


Figure 8.8. The Zernike power spectrum of a defocus aberration introduced by the Hex 69 of amplitude  $0.25\lambda$ . There is some crosstalk into mode 8.

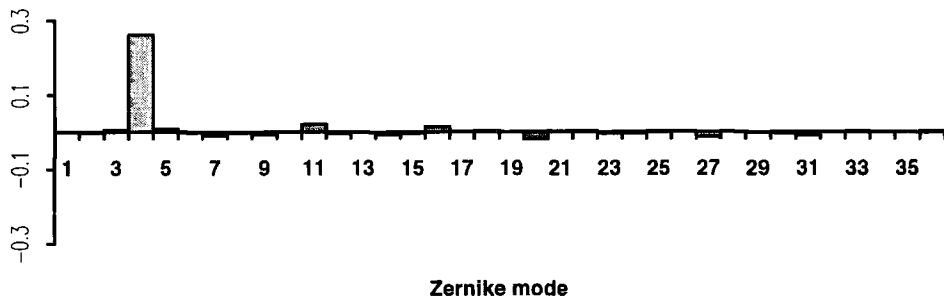


Figure 8.9. The Zernike power spectrum of an astigmatism (mode 4) aberration introduced by the Hex 69 of amplitude  $0.25\lambda$ .

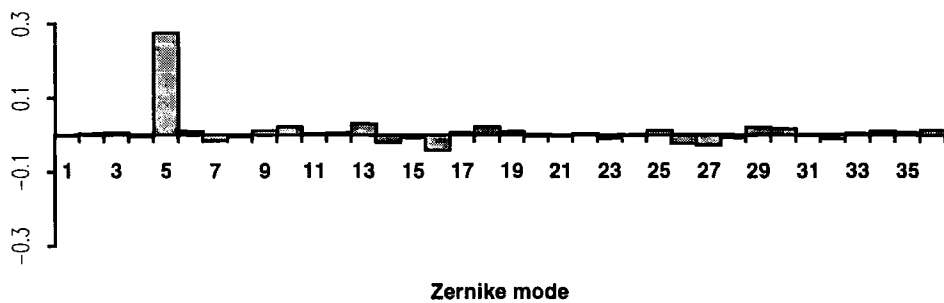


Figure 8.10. The Zernike power spectrum of an astigmatism (mode 5) aberration introduced by the Hex 69 of amplitude  $0.25\lambda$ . There is some crosstalk into higher order modes (mode 16).

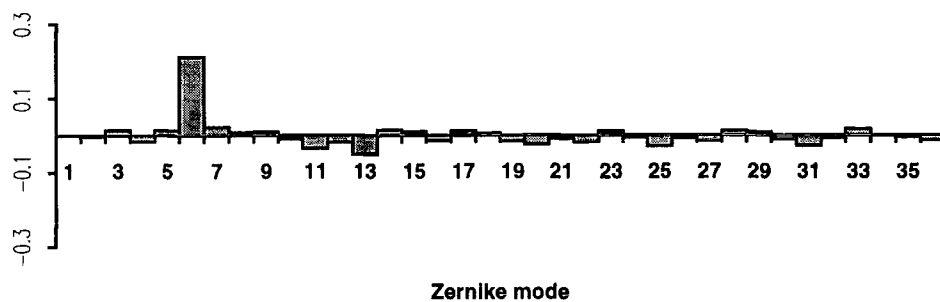


Figure 8.11. The Zernike power spectrum of an astigmatism (mode 6) aberration introduced by the Hex 69 of amplitude  $0.20\lambda$ .

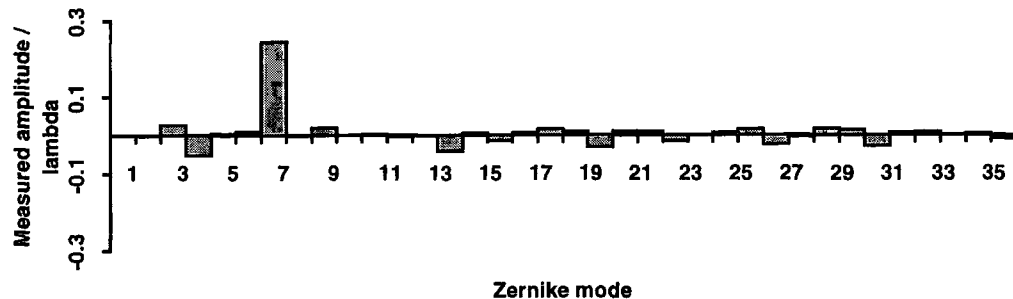


Figure 8.12. The Zernike power spectrum of a coma (mode 7) aberration introduced by the Hex 69 of amplitude  $0.25\lambda$ .

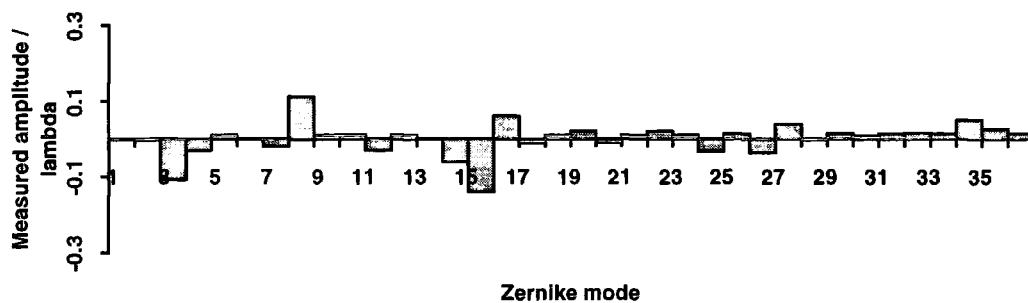


Figure 8.13. The Zernike power spectrum of a mode 8 spherical aberration introduced by the Hex 69 of amplitude  $0.25\lambda$ . There is some crosstalk into defocus, higher order spherical (mode 15) as well as other modes.

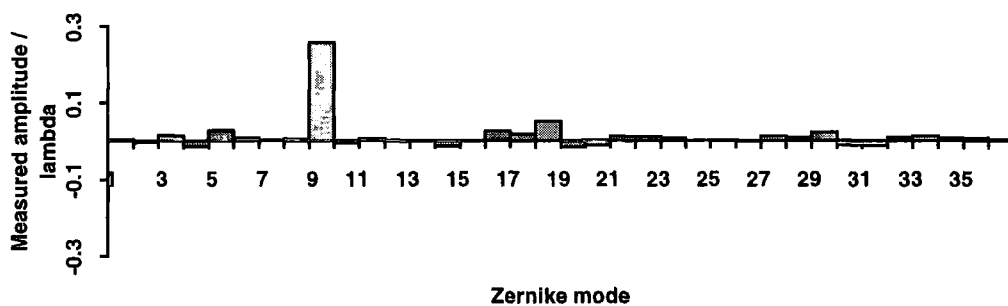


Figure 8.14. The Zernike power spectrum of a mode 9 aberration introduced by the Hex 69 of amplitude  $0.25\lambda$ . There is some crosstalk into mode 18.



Figure 8.15. The Zernike power spectrum of a mode 10 aberration introduced by the Hex 69 of amplitude  $0.25\lambda$ .

The higher order modes could not be measured with the Zygo unless the amplitude of the modes was reduced. The information about crosstalk was then lost in the background noise. Figure 8.16 shows the Hex69s Zernike power spectrum with no modes applied.

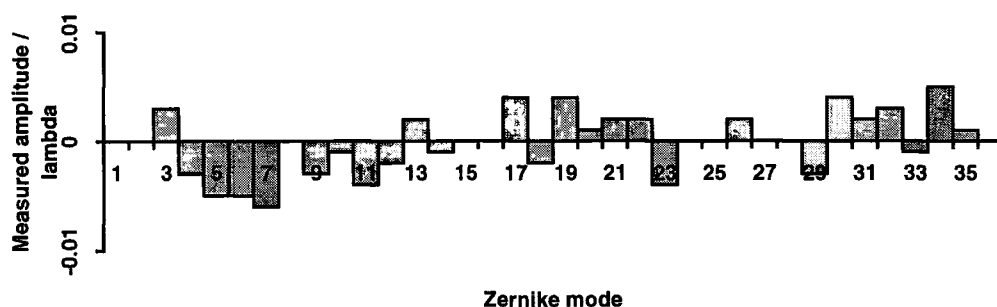


Figure 8.16. The Zernike power spectrum of the Hex69 with no Zernike modes applied. Note the scale difference when compared with the above measurements.

## 8.5 Shack-Hartmann / Hex69 System

### 8.5.1 THE SHACK-HARTMANN SYSTEM

The Shack-Hartmann used in this chapter was the same as in chapter 6. There were several differences in the software because the Hex69 was in a feedback loop. Twelve modes were calculated by the C40 and returned to the host PC. A

simple control algorithm was used to determine the phase shift applied to the Hex69. The  $n^{\text{th}}$  Zernike amplitude applied to the SLM is  $a_n(j)$  in the  $j^{\text{th}}$  frame and is calculated by

$$a_n(j) = a_n(j-1) + GAIN_n \times \xi_n(j) \times \Omega_n \quad [8.1]$$

where  $\xi_n(j)$  was the measured mode from the wavefront sensor and  $\Omega_n$  was the calibration gain.  $\Omega_n$  was calculated by applying each Zernike mode with the amplitudes of  $-0.5\lambda$ ,  $-0.25\lambda$ ,  $0.25\lambda$  and  $0.5\lambda$  to the Hex69 (as in §6.7.6). A best fit line was fitted to the data and the gradient of this used as  $\Omega_n$  (the intercept of the best fit line was approximately zero and so could be ignored). Using [8.1] filters out some of the random noise from the system but no other control loop considerations have been made so far. A high value for  $GAIN_n$  would have caused oscillations in the system so it was deliberately kept low at 0.25 for each mode. This system was only for demonstration purposes so it was not fully optimised.

### 8.5.2 SYSTEM ALIGNMENT

Because the Hex69 was in a closed loop it was easier to align than the open loop system in chapter 7. The application of Zernike modes to the Hex69 was measured by the Shack-Hartmann. It was important to check that each mode with an angular dependency, such as astigmatism and coma, were in the correct rotation. From §8.4.2 it can be seen that there was little, if any, crosstalk between low order modes, until spherical (mode 8). This can be used to check the optical alignment. If there was a significant amount of crosstalk it indicated that there was an alignment error in the system.

### 8.5.3 CROSSTALK MEASUREMENTS

The above crosstalk measurements were repeated using the Shack-Hartmann as the wavefront measurement device. The Zygo and Shack-Hartmann use two

completely different techniques for measuring the Zernike modes. If crosstalk was present in both results, it is more likely to be a real phenomenon and not just an error from the Zygo's fitting routine. The data taken was the mean of 100 Shack-Hartmann frames and is shown in figures 8.17 to 8.26.

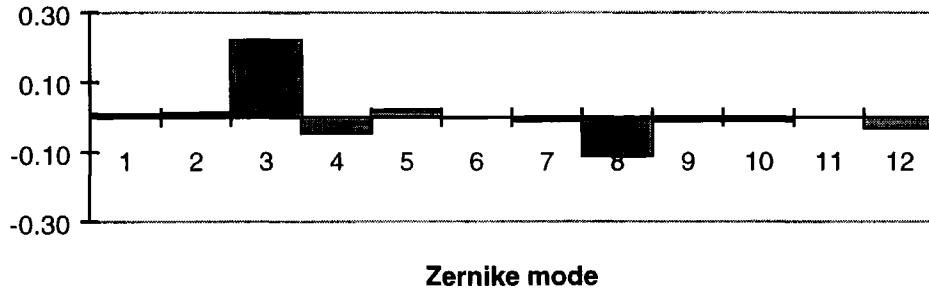


Figure 8.17. The Shack-Hartmann measured power spectrum of mode 3.

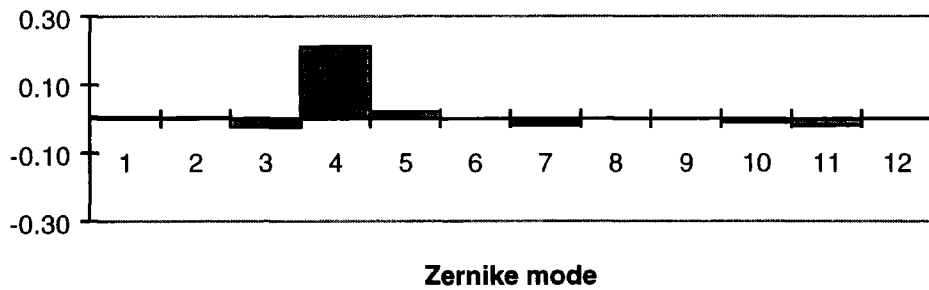


Figure 8.18. The Shack-Hartmann measured power spectrum of mode 4.

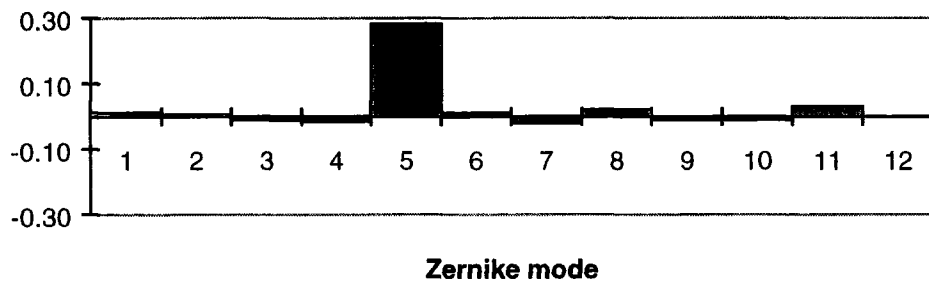


Figure 8.19. The Shack-Hartmann measured power spectrum of mode 5.

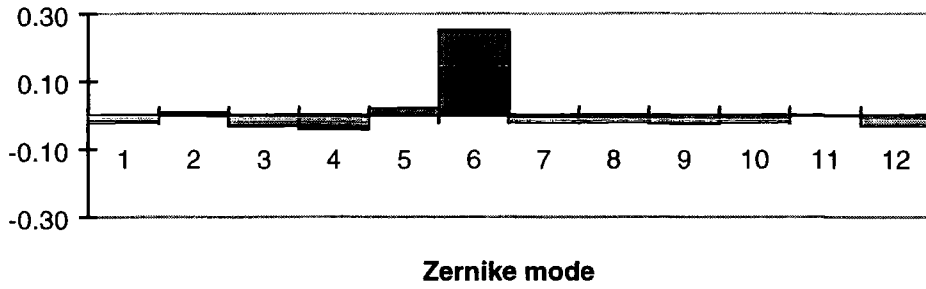


Figure 8.20. The Shack-Hartmann measured power spectrum of mode 6.

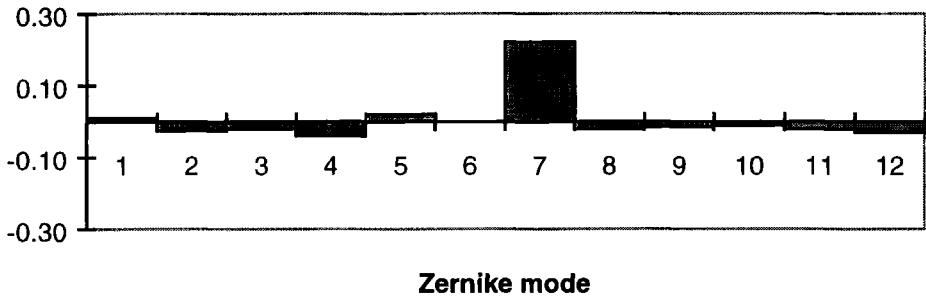


Figure 8.21. The Shack-Hartmann measured power spectrum of mode 7.

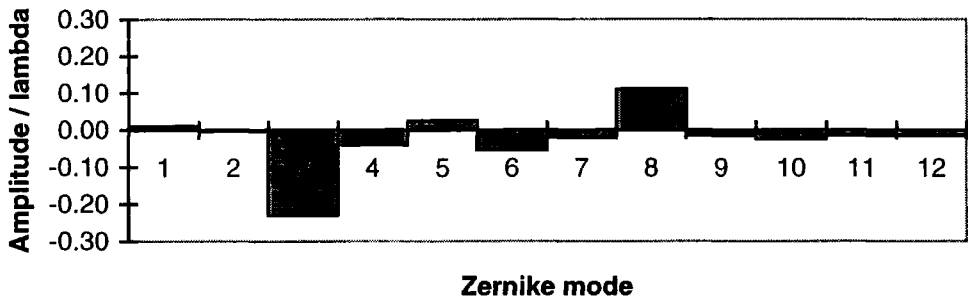


Figure 8.22. The Shack-Hartmann measured power spectrum of mode 8.

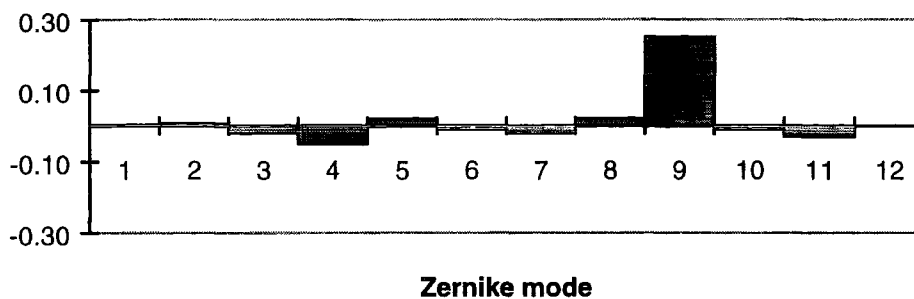


Figure 8.23. The Shack-Hartmann power spectrum of mode 9.

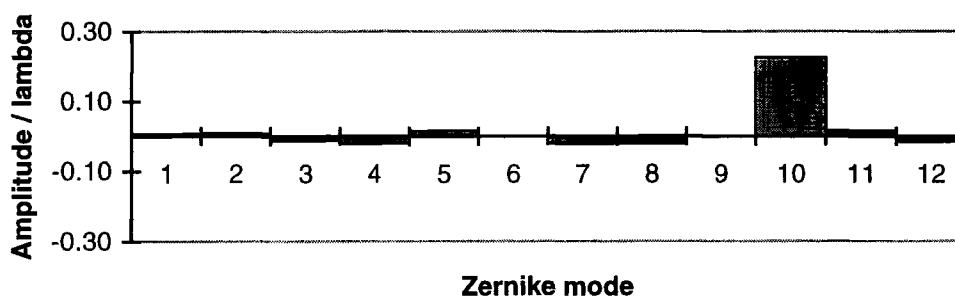


Figure 8.24. The Shack-Hartmann measured power spectrum of mode 10.

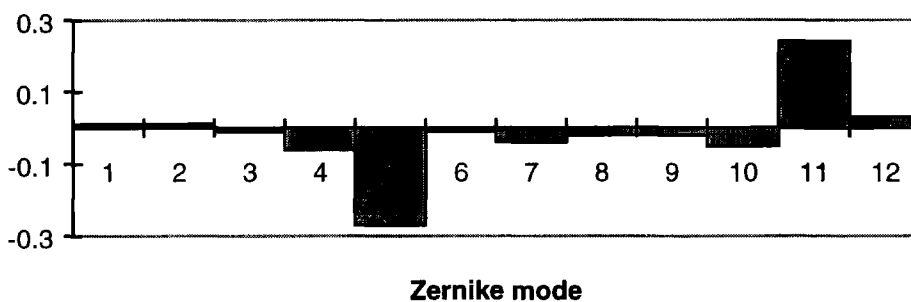


Figure 8.25. The Shack-Hartmann measured power spectrum of mode 11.

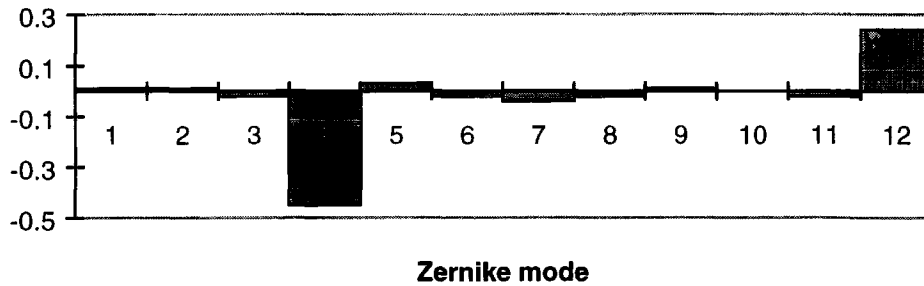


Figure 8.26. The Shack-Hartmann measured power spectrum of mode 12.

It can be seen from the above figures that the crosstalk between modes was also present in the Shack-Hartmann measurements. The effect of this crosstalk on the correction performance will be discussed below.

#### 8.5.4 THE CAUSE OF THE HEX69'S CROSSTALK

The source of the crosstalk in the Hex69 does not come from an electrical source as in chapter 4, but from the coarse pixelation of the Hex69. It can not reproduce the complex waveform of the higher order modes. Many of the high order modes place most of the aberration at the edge of the aperture. Since the pixel size of the Hex69 is approximately constant over the whole of its aperture, it has more difficulty reproducing these higher order modes.

The crosstalk can be simulated with a computer model. The DC term of the cross correlation of two functions gives a measure of the similarity of the two functions. Unpixelated Zernike modes are orthogonal functions and so there is a zero DC term of the cross correlation. If  $f_1$  and  $f_2$  are two functions, the cross-correlation is given by

$$|FT[FT(f_1) \cdot FT(f_2)^*]|^2 \quad [8.2]$$

where  $*$  represents the complex conjugate and FT is the Fourier transform function.

Simulations were carried out using MATLAB™. The SLM was represented by 100 10x10 pixels. The first 12 Zernike modes were mapped on to the array and each was cross correlated with each other. The results are shown in figures 8.27 to 8.38. The lighter shaded bars show the height of the DC term for 100 pixels and the solid bar is for a 400 pixel SLM.

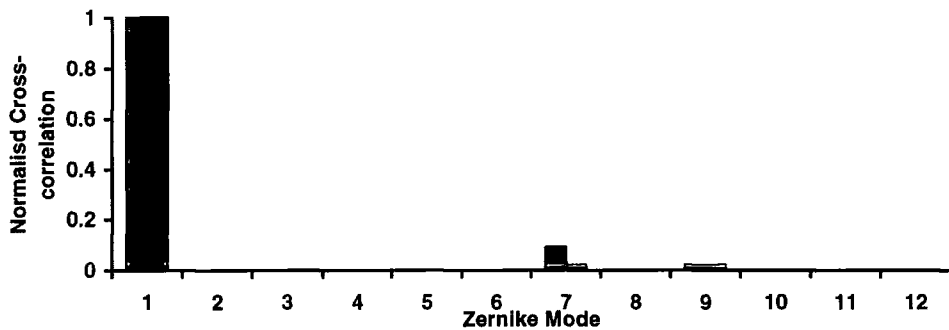


Figure 8.27. Mode 1 cross-correlated with the other Zernike modes.

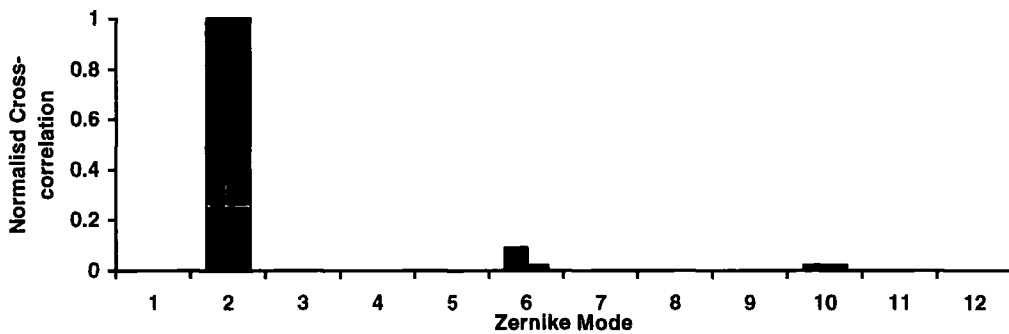


Figure 8.28. Mode 2 cross-correlated with the other Zernike modes.

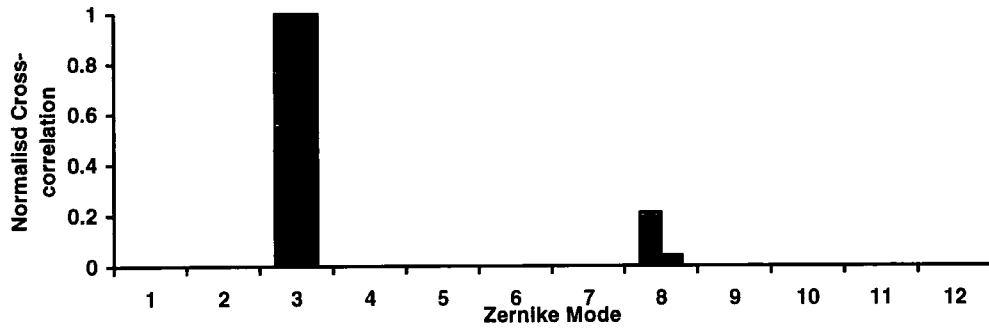


Figure 8.29. Mode 3 cross-correlated with the other Zernike modes.

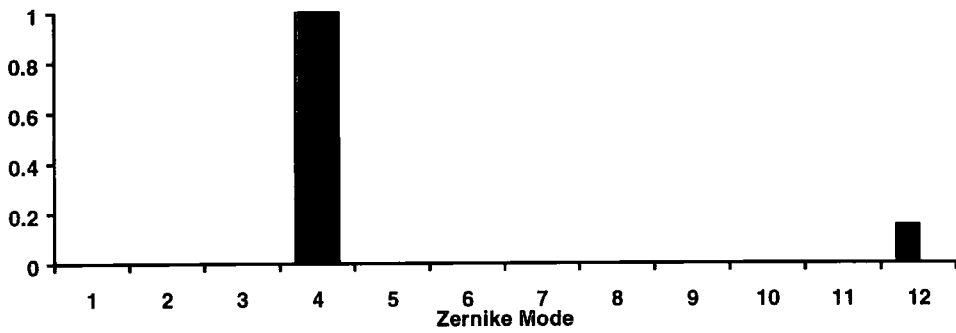


Figure 8.30. Mode 4 cross-correlated with the other Zernike modes.

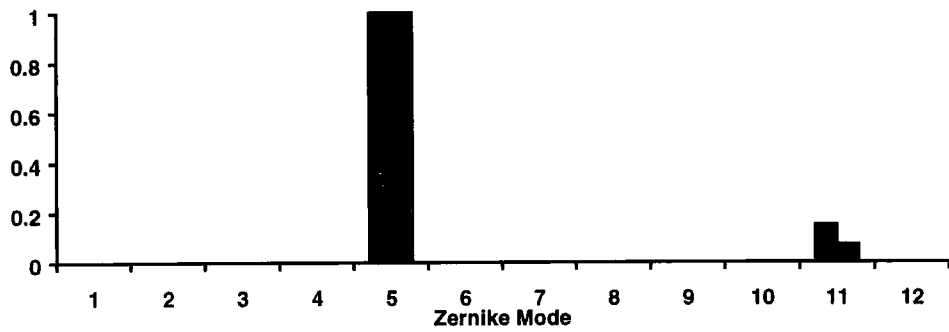


Figure 8.31. Mode 5 cross-correlated with the other Zernike modes.

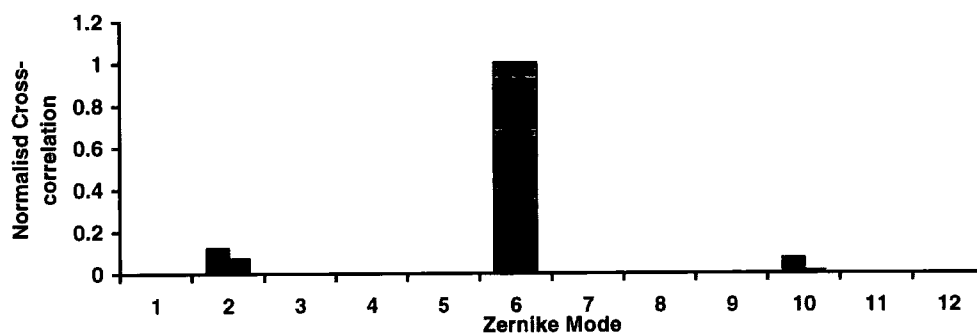


Figure 8.32. Mode 6 cross-correlated with the other Zernike modes.

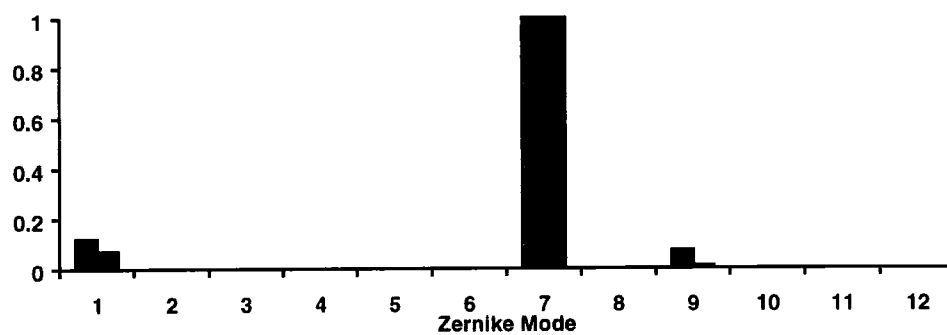


Figure 8.33. Mode 7 cross-correlated with the other Zernike modes.

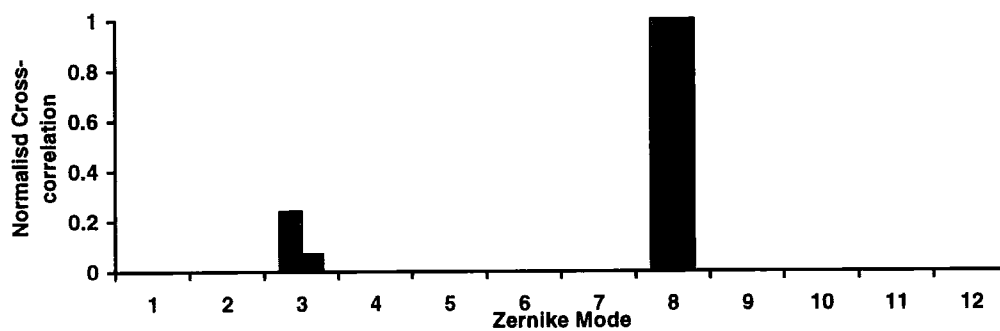


Figure 8.34. Mode 8 cross-correlated with the other Zernike modes.

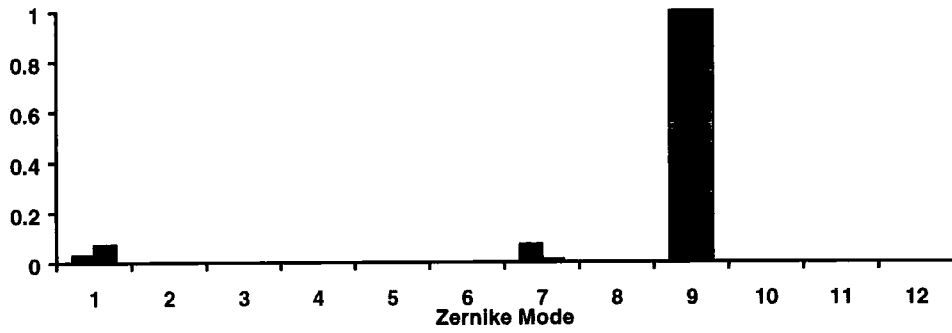


Figure 8.35. Mode 9 cross-correlated with the other Zernike modes.

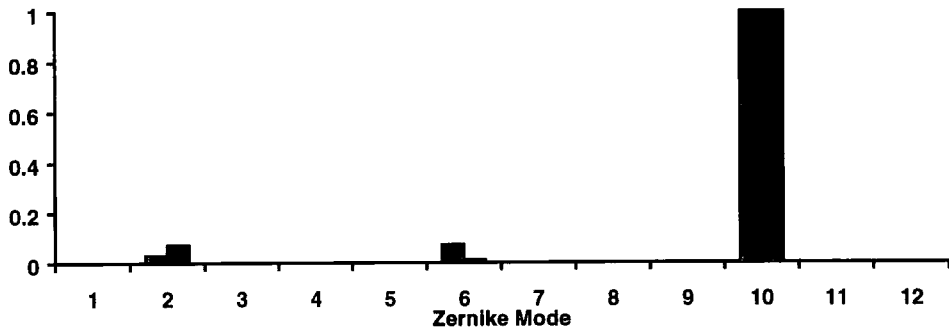


Figure 8.36. Mode 10 cross-correlated with the other Zernike modes.

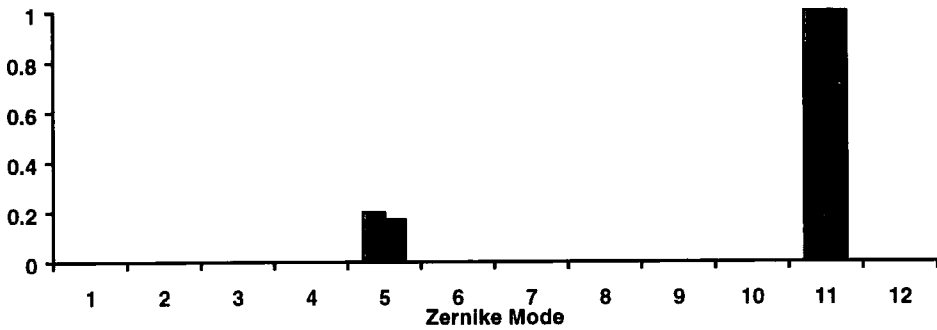


Figure 8.37. Mode 11 cross-correlated with the other Zernike modes.

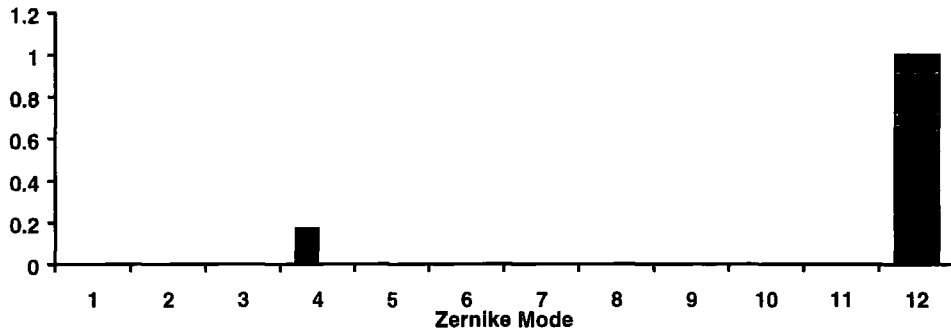


Figure 8.38. Mode 12 cross-correlated with the other Zernike modes.

It can be seen that the positions of the peaks in figure 8.27 to 8.38 agree reasonably with those measures in the above two sections. There is some slight discrepancy that is likely to be due to the pixel shapes been different in this model. By increasing the number of pixels to 20x20, the crosstalk effect is generally reduced. Mode 8 (spherical) has a large amount of crosstalk into mode 3 (defocus). This is likely to come from the similarity between the modes. Both are independent of  $\theta$ , defocus is  $\propto r^2$  and spherical is  $\propto r^2+r^3$ , where  $\theta$  is the angular co-ordinate and  $r$  is the dimensionless radial co-ordinate. Plotting a cross section of these two modes (figure 8.39) shows that they are approximately similar in the central region and diverge toward the edge of the aperture. Since the gradient at the edge of mode 8 is quite large it is not unreasonable to assume that the Hex69 will have difficulty in modelling the edges accurately. This error will make modes 8 similar to mode 3 when they are coarsely pixelated.

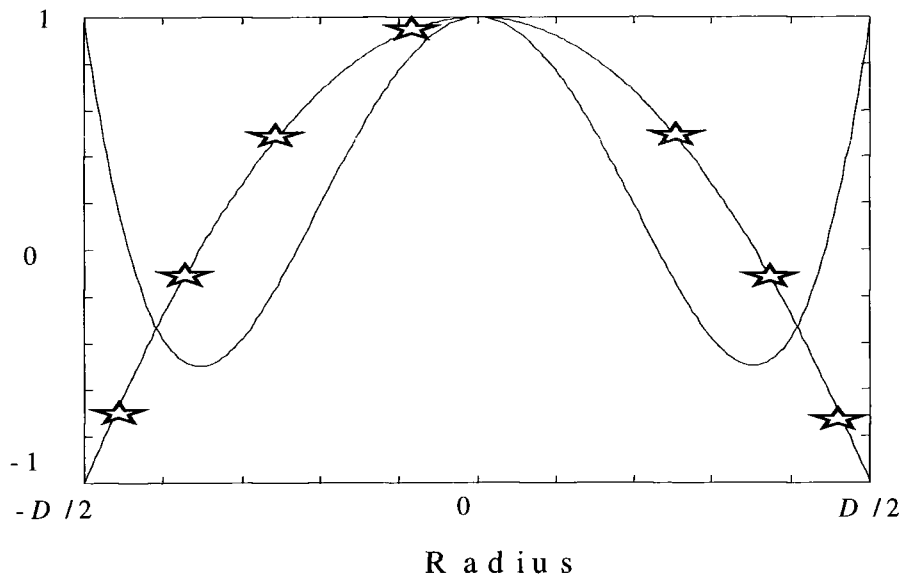


Figure 8.39. A cross section of two Zernike modes. One negative wave of defocus (indicated by stars) and a wave of spherical (solid line) are shown demonstrating the similarities of the two modes in the central region.

These crosstalk effects can be minimised when the Hex69 is used as the corrector because of two reasons. The system incorporates negative feedback and so any added mode will be removed in the next frame. Secondly, the DSP only returns the first 12 modes to the PC. The low order modes do not generate large amounts of crosstalk. Out of the 12 modes only the first 8 were used and the amplitude that could be applied to the Hex69 was limited to  $\pm 0.5$  waves for each mode.

### 8.5.5 LABORATORY TURBULENCE SIMULATION

To demonstrate a real time adaptive optics system in the laboratory it is necessary to introduce randomly varying aberrations, preferably with Kolmogorov statistics. This was achieved in chapter 6 by using the Hex69 SLM. However, there is currently only one such device at the University of Durham. An alternative device was constructed from a cardboard tube about 50cm long with a resistive wire inside. There was also a computer cooling fan in the centre of the tube to generate further turbulence. Both of these elements could be controlled by varying the voltage across them.

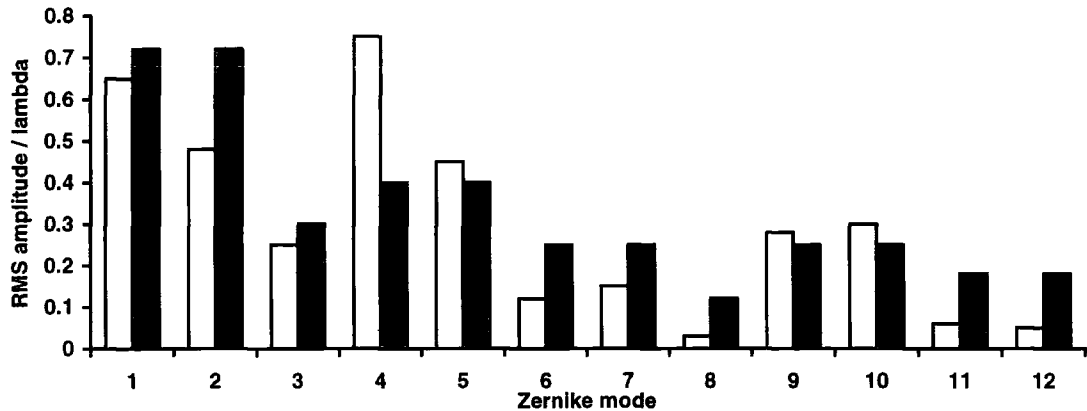
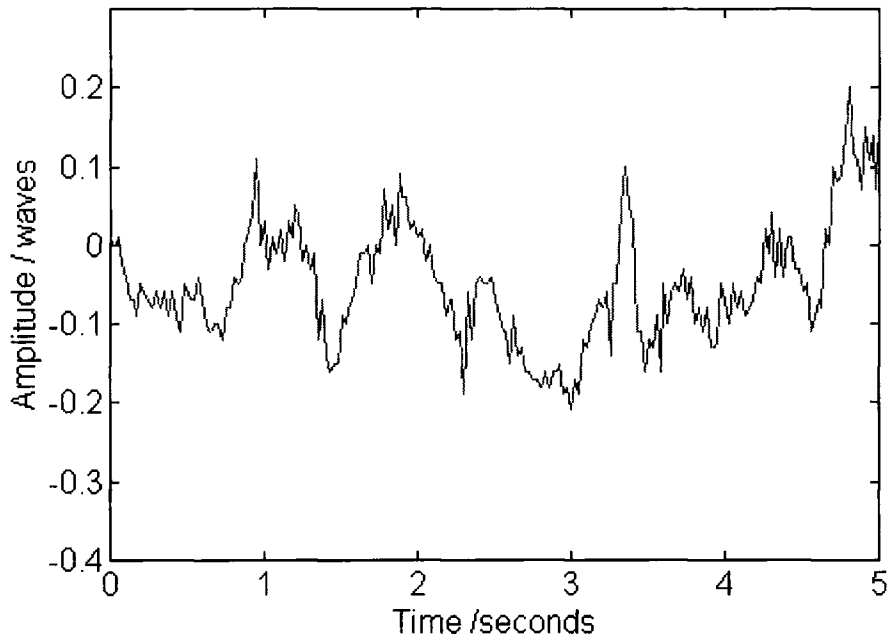


Figure 8.40. The measured RMS Zernike mode amplitudes of the cardboard tube ATS. The solid bars represent the theoretical modes for a  $D/r_0$  of 10. The white bars are the measured modes.

A thousand frames of the Shack-Hartmann were taken to analyse the performance of the atmospheric turbulence simulator. The RMS of the first 12 Zernike modes is shown in figure 8.40. Although modes 1 and 2 (tip/tilt) are slightly lower than desired and mode 4 (astigmatism) is higher, it quantitatively approximates to Kolmogorov statistics. The lower than average tip/tilt is advantageous because in a real telescope system there would be a tip/tilt mirror to remove these two terms. The solid columns in figure 8.40 show the theoretical Kolmogorov power spectrum for  $D/r_0 = 10$  (Wang, 1978). Figure 8.41 shows 1000 frames of mode 3 (defocus) measured with the Shack-Hartmann. The temporal characteristics show abrupt changes in amplitude. This is qualitatively similar to the atmosphere.



*Figure 8.41. The first 5 seconds of data for mode 3 (defocus).*

### 8.5.6 STATIC CORRECTION

The system was first run with a static aberration added into the optical path. A piece of aberrating glass was placed in front of the Hex69. The measured modes were written to a file as the correction was performed. The correction of mode 3 (defocus) is displayed in figure 8.42. It can be seen that it takes 5 frames to perform a correction from 0.8 waves to system noise level. The frame rate of the system was 15Hz.

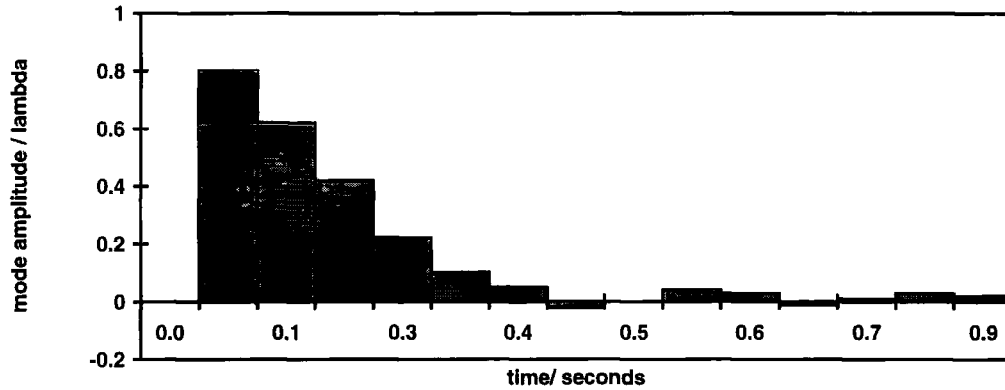


Figure 8.42. A step response of mode 3 for a static correction in closed loop.

### 8.5.7 CLOSED-LOOP EXPECTATIONS

By using equation [7.3] it is possible to estimate the correction achievable with the Hex69 and Shack-Hartmann system. It can be assumed that the wavefront sensor noise,  $\sigma_{WFS}$ , is the same as before. The temporal bandwidth of the corrector is taken to be that of the Hex69's electronics frame speed, i.e.,  $f_c=26\text{Hz}$ . Equation [7.8] requires the wind velocity but this is however unknown for this simulator. However, by visual inspection, the spots of the Shack-Hartmann moved at a similar speed to the spots of the Shack-Hartmann used to study the ATS in chapter 6. To make an order of magnitude calculation of the wavefront variance the wind velocity has been approximated to  $5\text{ms}^{-1}$ , so  $\sigma_{Temp}^2=0.769$  radians<sup>2</sup>.

The Hex69 is 9 pixels across, and so for  $D/r_0$  of 10,  $\sigma_{Corr}^2=1.06$  radians<sup>2</sup>.  $\alpha$  has been taken as 1.26 again. The residual error after correcting 8 modes is calculated from [7.7] and  $\sigma_{Zern}^2=2.149$ . The total variance is then 3.96 radians<sup>2</sup>. This is approximately the same residual variance calculated in §7.3.6 for the FLC. Despite the Hex69s ability to give analogue correction of the wavefront it is disadvantaged because of its slower speed contributing to a larger value of  $\sigma_{Temp}^2$ ,

and its smaller number of pixels contributing to a larger value of  $\sigma_{\text{Corr}}^2$ . However, the Hex69 does also attempt to correct for a larger  $D/r_0$ . Using the value of  $D/r_0=8.5$  which was used in chapter 7, the total residual variance drops to 3.46 radians<sup>2</sup>. So in theory the system should perform better than the system of chapter 7.

### 8.5.8 CLOSED LOOP CORRECTION

Closed loop correction was then performed. The system was run with the simulated turbulence generator. The frame rate of the Shack-Hartmann system was 40Hz, although the Hex69 was only run at 26Hz. Because of the cross-talk effects and in an attempt to maximise the speed of the system, only the first 8 modes were used in the correction routine. The PSF measurements were taken with the ITEX integrating frame grabber, over a period of 10 seconds.

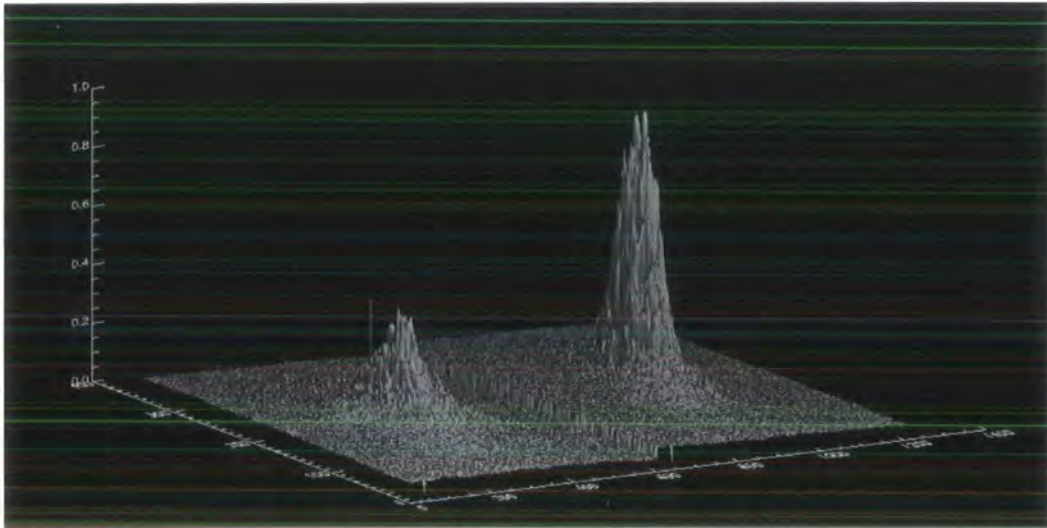


Figure 8.43. Real time correction results. The left graph is the uncorrected PSF, Strehl ratio = 7%. The right graph is the corrected, Strehl ratio = 12%.



Figure 8.44. The uncorrected PSF (left) and the corrected (right).

Figure 8.43 shows the aberrated and corrected PSFs. These are also shown as an image in figure 8.44. The Strehl ratio was increase from 7% to 12%, an increase of a factor of 1.7. The full width half maximum was decreased by a factor of 2.2.

### 8.5.9 REAL TELESCOPE TRIALS

The above system (without the turbulence simulator) has been tested on a real telescope. The telescope was the 'Vacuum Tower Telescope' (VTT) at Sunspot, New Mexico, USA. The telescope has a diameter of 76cm. It was planned to use the telescopes tip/tilt mirror in conjunction with the Hex69. Unfortunately the tip/tilt mirror would not work on night-time starlight and the Hex69 had to correct for tip/tilt itself. Because of the large sweep required in order to correct tip/tilt, the Hex69 was too slow to correct for the seeing. It is hoped that in the future the device can be tried again with its own dedicated tip/tilt mirror.

## 8.6 Discussion

The above experiment shows that correction using the nematic Hex69 is possible. The improvement in Strehl ratio is non-trivial for a first time system. The improvement is however lower than the correction achieved in chapter 7. The Strehl ratio was increased from 7% to 12% (compared with 23% to 33% in chapter 7). However, as a percentage increase this system gives a larger improvement (70%, compared to 43% in chapter 7). It is still important to

understand where the losses in performance have occurred and where improvements in future systems can be made.

One of the greatest difficulties with this real time correction was the speed of the system. This system has not yet been optimised fully. The  $GAIN_n$  values for each mode were set to 0.25 each. With such a low value it was sometimes difficult tracking the aberrations generated by the ATS. Higher values of  $GAIN_n$  were tried but they tended to cause oscillations in the system. A detailed studied of the control system is required to optimise the  $GAIN$  values.

The cardboard tube method of generating turbulence was not very controllable. It could not be operated for more than a few minutes before the air flow inside the tube became settled and no longer produced a large aberration. The speed of the turbulence is particularly difficult to control. Several lengths of tube were tried but this had little effect on the controllability of the turbulence. It is well known that nematic liquid crystal SLMs have slow speeds so it would be desirable to have more control over the simulated wind speed so that the corrections at different speeds could be measured.

It has been shown in this chapter that static corrections can be corrected very well with the Hex69. It can be expected that with a few modifications the system can be made to perform better. It is not unreasonable to assume that if the simulated wind speed could have been reduced, the Hex69 would have improved the Strehl ratio much more substantially than it did.

The performance should also be improved with the inclusion of a tip/tilt mirror in the system. In Kolmogorov turbulence, the first two modes have the most power. This required the SLM to sweep through a larger dynamic range. Since the large range causes the SLM to slow down considerably, removal of tip/tilt would have allowed the Hex69 to correct the higher order modes faster. This idea is in line

with other adaptive optics systems such as ELECTRA where a separate mirror removes the tip/tilt.

In conclusion, the system has improved the Strehl ratio of a real time aberration. Although the increase in the numerical value of the Strehl ratio was smaller than in the system of the previous chapter, the percentage increase was greater and the light efficiency of the whole system was considerably higher. A large improvement in Strehl ratio was demonstrated using the device statically. It is the author's opinion that if the speed of the real time system can be increased this method will provide the best adaptive optics system for astronomical applications due to its higher optical transmission and ability to potentially fully correct for an aberration.

### **8.7 Summary**

In this chapter a nematic liquid crystal adaptive optics system has been built. The wavefront sensor was a Shack-Hartmann sensor. Cross-talk between various Zernike modes has been experimentally measured. Both static and real time corrections have been demonstrated.

The next chapter will draw together the conclusions from all the experimental chapters and compare the results. It will present the conclusions of this thesis.

## **Chapter 9: Summary and Conclusions**

### **9.1 Introduction**

The aim of this thesis was to demonstrate working liquid crystal based adaptive optics systems. This chapter shall begin by summarising the work done in each of the experimental chapters (chapters 4-8). It will then compare each adaptive optics system, discussing the merits of each. The final section will discuss suggestions for future work.

### **9.2 Summary of Results**

#### **9.2.1 CHAPTERS 2 AND 3**

Chapters 2 and 3 gave a basic introduction to liquid crystals, atmospheric turbulence and adaptive optics.

#### **9.2.2 CHAPTER 4**

In chapter 4 a multiplexed nematic device was examined. The device was based on standard display technology, slightly modified to be used as a phase only modulator.

The device was capable of giving a  $7\lambda$  phase shift, however through a series of experiments to measure the phase shift produced by the device, it was discovered that there was a large amount of crosstalk between pixels. This crosstalk was known to happen in intensity modulating multiplexed displays so an experiment was performed to characterise it. It was found that when half (A) of the device was turned fully on and the other half (B) was turned fully off the actual phases shifts measured were  $5\lambda$  on half (B) instead of  $0\lambda$  and  $6\lambda$  on half (A) instead of the expected  $7\lambda$ . By looking at the voltage waveforms it was suggested that this effect came about from the multiplexing technique.

Although the crosstalk effects were less severe when only small differences in the voltages were applied to each half, the device was clearly limited in its application in adaptive optics. For this reason, no further work was carried out on the device.

### 9.2.3 CHAPTER 5

In this chapter, one of the simplest types of adaptive optics to implement was tested: '*binary adaptive optics*'. This system used an FLC SLM with a PDI as the wavefront sensor. Binary adaptive optics only requires the knowledge of whether a pixel is in or out of phase. For this reason it is not important to fully calculate the phase from an interferogram.

A computer model of the system was developed to enable an understanding of the complexities of the PDI. It was necessary to experiment with several control algorithms to obtain the best correction performance. An experimental system was constructed and aberrations were applied. The system corrected from a Strehl ratio of 5% to 26%. However it took ~5 frames to reach the maximum correction achievable. Some pixels oscillated. The optical transmission of the system was also extremely low. Both the FLC and the PDI were very lossy.

### 9.2.4 CHAPTER 6

In chapter 6 an atmospheric turbulence simulator (ATS) was developed. This was to test the system in the next chapter. Computer generated phase screens were produced off line. These were then mapped on to the Meadowlark Hex69 nematic liquid crystal SLM. A Shack-Hartmann wavefront sensor was constructed to test the performance of the device. The RMS of each Zernike mode and the Strehl ratio were found to be in reasonable agreement with the theoretical expectations. The temporal power spectrum showed an expected  $-8/3$  gradient on a log-log graph.

### 9.2.5 CHAPTER 7

In chapter 7 the ATS developed in chapter 6 was used as an aberrator in an FLC binary adaptive optics system. A Displaytech 10x10b FLC SLM was used as the corrective element and a Shack-Hartmann was the wavefront sensor. The system was run in real time producing a Strehl ratio improvement from 23% to 33%. The system ran at a speed of 6Hz. Although the wavefront sensor's light efficiency was improved, the system was still limited by the lossiness of the FLC and the low theoretical expectation.

### 9.2.6 CHAPTER 8

In chapter 8 the FLC was replaced by a Meadowlark Hex69 SLM. This improved the transmission of the corrective element to 90%. The system was run in real time with a frame rate of 26Hz. An improvement in Strehl ratio from 7% to 12% was measured. There was also an analysis of the cross talk between Zernike modes generated by the Meadowlark. The static correction of a piece of aberrated glass was also performed. This suggested that if the device was not so limited by speed it should be able to correct aberrations very well in a real time system.

The correction results are summarised in table 9.1. Only considering the Strehl ratio increase the FLC/PDI system (chapter 5) is considerably better than the other two. However, the system has a very poor optical transmission. The FLC only allows 2% of light through and the PDI is known to have low transmission (although this could be improved by using a phase shifting PDI). The major problem with this system is its instabilities and the fact it takes several frames to reach the best solution. These factors make it unsuitable for atmospheric adaptive optics.

System	Aberrated Strehl Ratio	Corrected Strehl Ratio	Percentage Increase	Transmission of SLM*	Wavefront Sensor Frame Rate	Notes
FLC/PDI	5%	26%	420%	2%	10Hz	<sup>1</sup>
FLC/Shack-Hartmann	23%	33%	43%	2%	6Hz	<sup>2</sup>
Hex69/Shack-Hartmann	7%	12%	70%	44%	40Hz	<sup>3</sup>

*Table 9.1. A summary of the correction results.*

The second system, the FLC/Shack-Hartmann (chapter 7) had a more light efficient wavefront sensor. This system was considerably more stable than the PDI system and only took one frame to reach the best correction. The transmission of the FLC was still however very low. The system still had a low theoretical maximum performance. The maximum theoretical correction with binary adaptive optics of a severely aberrated wavefront is 40.5%, when taking into account other factors such as the finite number of pixels this is reduced further.

The third system provided the best real time correction. The transmission of the device was considerably higher than the FLC. Although the FLC/PDI system gave a greater improvement, this system was faster, more stable, and more light efficient. It must also be taken into account that this system was attempting to

---

\* Transmission value includes polarisers.

<sup>1</sup> The system took several frames to reach the final solution. The transmission of the PDI was very low. The system was prone to becoming unstable.

<sup>2</sup> The slow frame rate is because of a slower camera on the wavefront sensor than the Shack-Hartmann below. Using the same camera both systems should run at the same frame rate. 50% of the light was used by the Shack-Hartmann.

<sup>3</sup> The frame rate of the SLM was limited to 26Hz. 50% of the light was used by the Shack-Hartmann.

correct for an aberration greater and faster than that in the FLC/Shack-Hartmann system. Although the speed of the nematic liquid crystal SLM is slower than the FLC several options for future work will be discussed later which should make the device run slightly faster. For this reason, it is the conclusion that the Meadowlark Hex69 SLM with a Shack-Hartmann wavefront sensor is the best choice with current technology for a liquid crystal adaptive optics system for astronomy. Of the three systems tested, this system has filled the criteria required for an atmospheric adaptive optics system the best.

### **9.3 Future Work**

#### **9.3.1 MEADOWLARK/SHACK-HARTMANN SYSTEMS**

One of the most important steps in the next stage of the Meadowlark/ Shack-Hartmann system would be to increase the speed of the system. Several ideas are listed below.

1. Improve the drive electronics. At the moment the Meadowlark SLM is been driven through the printer port. This introduces the 26Hz frame speed. If the device was driven using a digital interface the bandwidth of the electronics should improve. Although the speed of the liquid crystal would not increase, it would mean a faster switching speed for phase shifts  $< \lambda$ .
2. Optimisation of the calibration curve. The response time of a nematic liquid crystal SLM is non-linear, i.e., a shift for 0 to  $\lambda/2$  takes a different amount of time to a shift from  $\lambda/2$  to  $\lambda$ . By choosing the correct range to be used by the calibration curve the liquid crystal will operate slightly faster.
3. Optimisation of the control loop. The control feedback loop for the system has not been optimised. Analysis of the system using linear control theory should enable the system gains to be set more accurately allowing the Meadowlark to reach the desired correction in less frames.

4. Include a tip/tilt mirror. The largest aberrations in Kolmogorov turbulence are tip/tilt. These aberrations require the Meadowlark to sweep through a large range to correct for them. If the tip/tilt was removed with a tip/tilt mirror, the Meadowlark could be used to only correct the higher order modes. These modes would require smaller ranges for the liquid crystal and so they could then be corrected faster.

As well as the above improvements the following should be also done.

1. Optimise the reflectivity of the beam splitter so that as much light as possible goes to the science camera and the Shack-Hartmann still works.
2. Cascade two devices together. The second device should have its optical axis orthogonal to the first. There would then be no polariser required and the transmission should improve to approximately 81% (assuming 90% transmission for both devices.)
3. A larger number of Zernike modes should be used to control the SLM. This will improve the total amount of correction possible. Any loss in computer speed could easily be compensated by replacing the 80486 PC with a Pentium PC.

### **9.3.2 FLC/SHACK-HARTMANN SYSTEM**

Currently the FLC system is limited by its poor transmission. Until a high switching angle device can be developed, FLCs will be of little use in astronomy. Once high switching angle device are developed FLCs will enable a very fast adaptive optics system. It will probably be desirable to cascade two or more devices together to get at least quarter wave switching so that the aberration can be more fully corrected. The best wavefront sensor for achieving this will probably be the Shack-Hartmann.

### **9.3.3 ATMOSPHERIC TURBULENCE SIMULATOR**

Many of the improvements that could be made to the Meadowlark adaptive optics system are applicable to this. In addition, the following is recommended for further work.

1. If tip/tilt is to be modelled, use a separate tip/tilt mirror to increase the speed of the liquid crystal.
2. Cascade several devices together to simulate multi-layer turbulence. This would be useful for testing multi-conjugate adaptive optics systems.

## Appendix 1: The Zygo Interferometer

The Zygo interferometer is used extensively in this thesis. This appendix briefly describes the device.

### A1.1 System Design

The Zygo is a double pass interferometer. The laser source is a 1mW red He-Ne. This light passes through a reference plate that reflects part of the light back to the Zygo's imaging CCD camera. This is the reference part of the beam. The rest of the light passes through to the test object. If the test object is transparent, such as a liquid crystal SLM, an optically flat mirror is placed behind the object. This reflects the light back into the Zygo where it then interferes with the test beam forming an interferogram on the CCD camera. A piezo-electrically controlled mirror can alter the path length of the reference beam so that the (modulo  $2\pi$ ) phase can be completely calculated. Taking the familiar interference intensity equation

$$I_1 = (1 + \alpha^2)I_0(1 + \gamma \cos(\theta)) \quad [A1.1]$$

where  $I_0$  and  $\alpha I_0$  are the intensities of the two interfering beams,  $\gamma$  is the fringe contrast (see equation [5.6]) and  $\theta$  is the phase between the test and reference beams. If an additional  $\pi/2$  phase shift is added to the reference beam (by moving the reference plate with piezo-electric crystals) we now get

$$I_2 = (1 + \alpha^2)I_0(1 - \gamma \sin(\theta)) \quad [A1.2]$$

Two additional shifts of the reference beam by  $\pi$  and  $3\pi/2$  radians gives

$$I_3 = (1 + \alpha^2)I_0(1 - \gamma \cos(\theta)) \quad [A1.3]$$

$$I_4 = (1 + \alpha^2)I_0(1 + \gamma \sin(\theta)) \quad [A1.4]$$

From a single measurement it is impossible to determine  $\theta$ . The arc-cosine does not give a unique solution, in addition  $\alpha$ ,  $\gamma$  and  $I_0$  are usually unknown. However, if all four measurements are made [A1.1], [A1.2], [A1.3], and [A1.4] can be rearranged to give

$$\theta = \arctan\left(\frac{I_4 - I_2}{I_1 - I_3}\right) \quad [\text{A1.5}]$$

which does give a unique solution between  $-\pi$  and  $\pi$  radians.  $I_0$  and  $\gamma$  also cancel. It is still impossible to distinguish between  $0+\theta$  and  $2\pi n+\theta$ , where  $n$  is an integer. The Zygo gets around this by assuming that the phase is continuous across the aperture, and adds  $2\pi$  to any pixels that are discontinuous (over certain threshold) with their neighbours.

Five measurements are taken by the Zygo. The first four have their reference beams phase shifted as described above. The fifth is identical to the first and is used to check for any environmental perturbations that may have occurred during the measurement. The interferograms are processed off line on an IBM compatible PC.

### **A1.1.1 THE ZYGO PTI SPECIFICATIONS**

The Zygo specifications are given in table A1.1. The resolution is determined by the digitisation of the interferogram by the CCD camera frame grabber. The accuracy is dependent on the flatness of the optical reference plate. This can be improved by subtracting the known aberrations of the reference plate from the test data.

Phase measurement resolution	$\lambda / 256$
Phase measurement accuracy	$< \lambda / 50$ Peak to Valley
Repeatability	$\lambda / 100$ to $1\sigma$
Data acquisition time	$\sim 1s$
Beam size	switchable to 33mm or 102mm
Light source	1mW He-Ne Laser, 632.8nm

*Table A1.1. The Zygo interferometer specifications*

### **A1.1.2 ZERNIKE MODE FITTING**

The Zygo fits up to 36 Zernike polynomials to the data. Each term is fitted by minimising the RMS error from a given test phase screen to typically less than  $1/50\lambda$ . Any of the Zernike modes can be altered and the measured phase screen regenerated with the new Zernike modes. This enables tip/tilt to be removed from the data. Tip/tilt is usually due to a misalignment of the interferometer and so is generally removed.

### **A1.1.3 DISADVANTAGES OF PHASE SHIFTING INTERFEROMETRY**

The obvious disadvantage of this technique of determining phase is that unless four separate interferometers are used, it is not possible to have a fast data acquisition time. The Zygo takes about 1 second to take the raw data but about a further minute to post-process it and write it to disk. This makes real time adaptive optics impossible with the Zygo.

The other disadvantage is when a pixelated device such as the Meadowlark SLM is measured, the assumption that the wavefront is smooth and continuous is no longer valid. If a large aberration is placed on to the Meadowlark SLM, the Zygo software will not unwrap the phase correctly and the result will be completely different from the expected phase screen.

#### **A1.1.4 ADDITIONAL FEATURES**

The Zygo can store the data in one of three formats: phase data; 36 fitted Zernike modes; or raw interferograms. The Zygo software also offers the additional possibilities: the calculation of point spread and modulation transfer functions; manipulation of Zernike mode coefficients and phase screens; and various data display options.

## Appendix 2: The design of a non-pixelated SLM

One of the limits of adaptive optics systems is the limited number of actuators that perform the correction. With deformable mirrors this can be limited by the cost and the technical demands of constructing such a large number of actuators. In liquid crystal SLMs the limit comes from the large number of connections requiring either a large dead space between pixels or having to multiplex and so losing accuracy. In this appendix a novel liquid crystal alternative is proposed. The device has no pixels to speak of, but is more like a continuous face plate deformable mirror. There is also the possibility of a very large number of actuators. With  $0.5\mu\text{m}$  wide electrodes it should be possible to achieve an actuator density of  $\sim 2 \times 10^4$  per  $\text{cm}^2$ . This would have no problems of interpixel dead space, although this calculation does not address the problem of how to electrically connect such a large number of electrodes.

### A2.1 Basic design

The basic idea is to use a resistive layer instead of individual pixels. Starting from the top layer there would be

1. A layer of ITO<sup>1</sup> coated glass. This would be the electrical ground.
2. Nematic liquid crystal material, with parallel alignment.
3. An electrically resistive material such as silicon. To this there would be electrodes attached at discrete points.

Because the electrodes are connected by a resistive layer there will be a ramp function in the voltage from an electrode with a high voltage applied and an electrode with a lower voltage (see figure A2.1)

---

<sup>1</sup> ITO (or indium tin oxide) is a transparent electrical conducting layer deposited on glass and is used for liquid crystal applications.

To demonstrate that in a 2 dimensional layer this will work, simulations were carried out using Spice. This is an electrical circuit simulation package. The 2 dimensional resistive layer was simulated by approximating it to an array of identical interconnecting resistors (see figure A2.2) and applying voltages to different points.

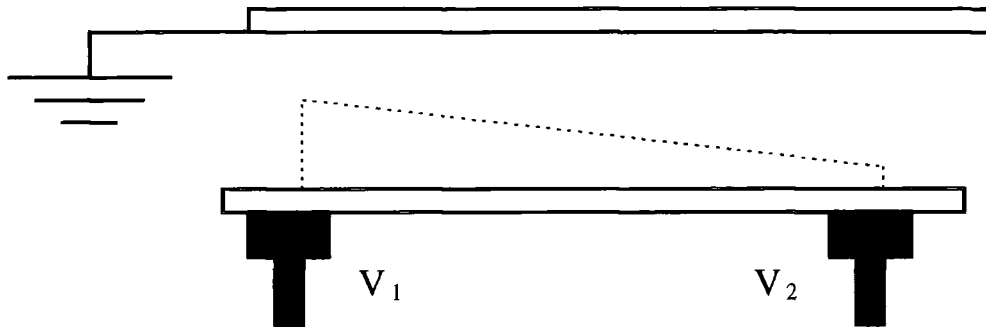


*Figure A2.1. The voltage slope across the resistive layer.  $V_1$  and  $V_2$  are applied via discrete electrodes. At the top is earthed ITO glass.*

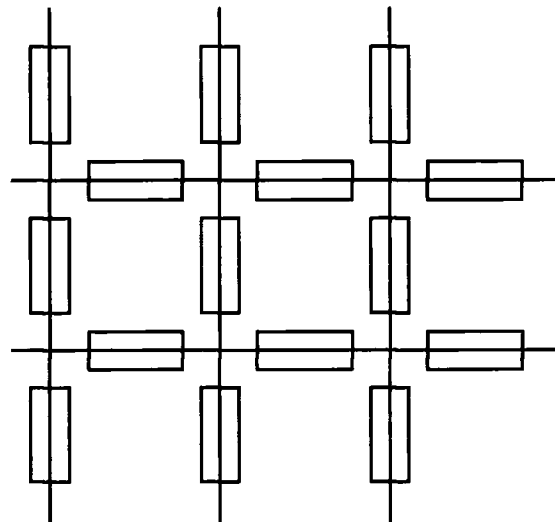


*Figure A2.2. An example of the resistive network used as an approximation for the simulation of the resistive layer.*

Figure A2.3 shows a contour map of the voltages over the area covered by 4 electrodes. The voltages applied to the electrodes were 2,4,6,8 volts.

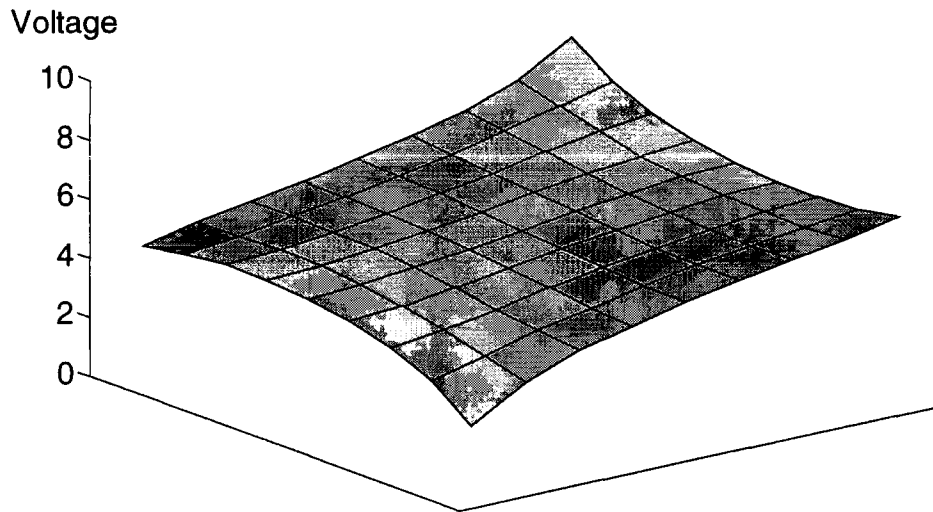


*Figure A2.3. The voltage profile across an area of the resistive layer. Electrodes are in the four corners.*

From figure A2.3, it can be seen that the phase shift caused by the device will be continuous, similar to that of a continuous face plate mirror. For this reason it is possible that the device would be well suited to be used with a curvature sensor wavefront detector, with each electrode lined up with a subaperture of the curvature sensor.

Riza *et al.* (Riza, 1994) has developed a 1 dimensional liquid crystal lens based on a similar idea to this. He applied voltages across strips of a resistive material to create a cylindrical lens. Because his device was one dimensional (he could only alter row voltages), the construction was simpler because each electrode was at the edge of the device. Construction ideas for a 2 dimensional device are slightly harder and are discussed below.

### **A2.1.1 DESIGN 1**

Several designs were considered for constructing such a device. The first design used a 12x12 pin chip holder. Graphite rods (from an automatic pencil) were placed in the pins and a layer of acrylic plastic placed on top of this which was the same depth as

the graphite rods. The surface of the device was then polished to get it optically flat. A resistive layer was then to be deposited on top of this (see figure A2.4). The exact material to be used was to be determined. Options included depositing a semiconductor on top or painting a layer of conducting glue on and re-polishing.

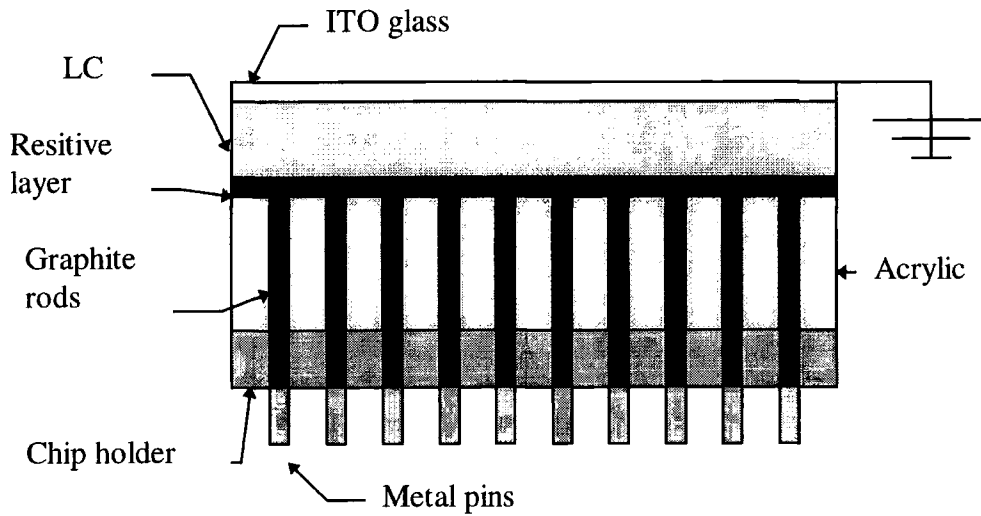


Figure A2.4. The first design.

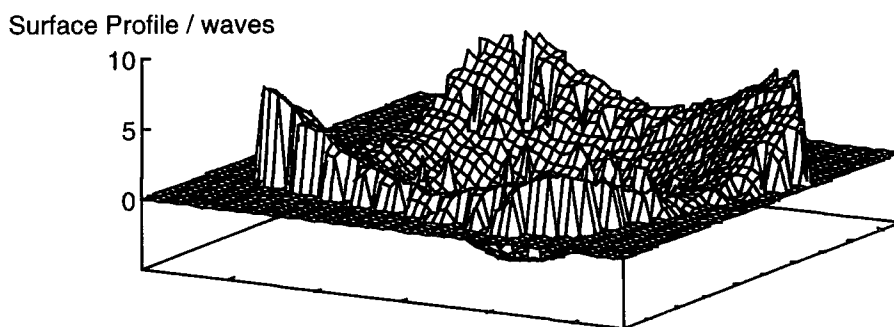


Figure A2.5. A surface profile of the plastic layer measured with the Zygo interferometer.

Figure A2.5 shows a surface profile measured with the Zygo. The plastic layer deformed under the pressure of polishing the device and so a flat finish could not be produced. The device continued to warp for several hours after the device had been polished. It became so bad that the Zygo could no longer measure the aberration.

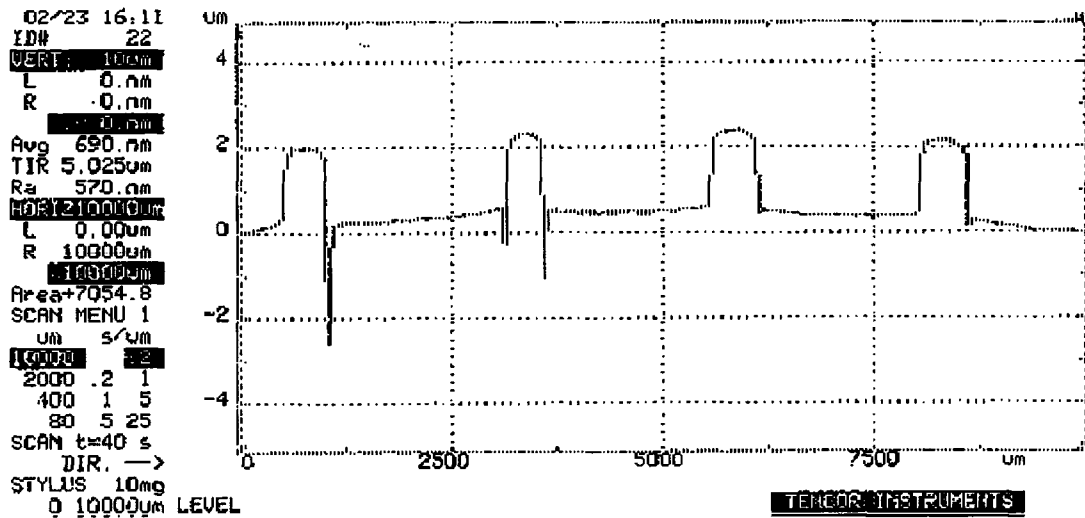


Figure A2.6. An Alpha-step profile of the device. Note how the graphite rods protrude from the surface by  $\sim 2\mu\text{m}$ .

An alpha-step profile was taken over several of the graphite rods (figure A2.6). The alpha-step works by dragging a needle over the device and measuring the vertical movement of the needle to an accuracy of  $\sim 1\text{nm}$ . This showed that the plastic is removed much faster than the graphite when the device was been polished. This left the graphite rods protruding from the surface by several micrometres. It was clear that this device would not have the specifications desired and the design was dropped.

### A2.1.2 DESIGN 2

The second design to be considered was to deposit aluminium tracks onto a semiconductor wafer (see figure A2.7). The wafer would be silicon and had one surface oxidised in an oven to resistive silicon oxide. Pits would be etched through the silicon oxide. The aluminium tracks would lead from these pits to the electrical connections of the device. The thickness of the silicon oxide wafer would shield the liquid crystal material from the tracks except for where the pits have been etched through to the silicon. The depth of the pits is controlled by the sputtering of boron

ions onto the reverse surface of the silicon. When the etching acid reaches the boron, it stops. This design has promise but the device was deemed to be too fragile to withstand the rest of the construction process (Wood, 1996).

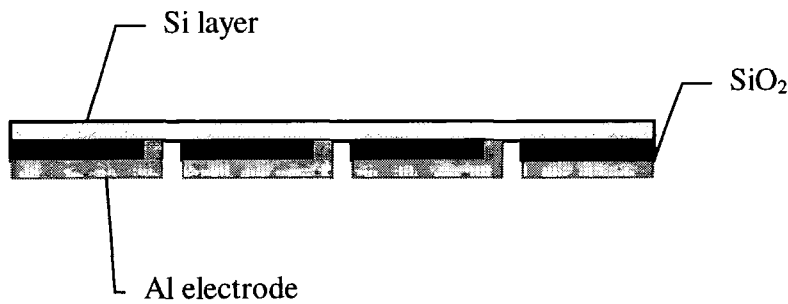


*Figure A2.7. Design 2. The liquid crystal material would go on top of the Si layer. The SiO<sub>2</sub> would shield the liquid crystal from the Al electrodes except at the points where pits are etched.*

### A2.1.3 DESIGN 3

The final design was the most promising. The device would be built on a glass substrate. This gives a strong, hard and optically flat surface. The aluminium electrode tracks are then deposited on to the glass lithographically. On top of this, a layer of silicon oxide (or liquid glass) is deposited. Holes are then etched into the layer through to the aluminium tracks (with an acid that does not readily attack aluminium), and a layer of semiconductor (silicon) is deposited on top of this. The rest of the cell can be constructed on top of this, i.e., the liquid crystal layer and ITO glass (see figure A2.8).

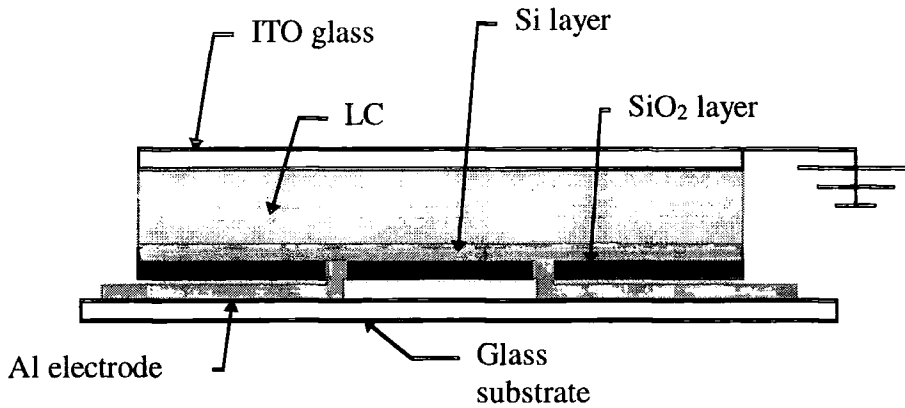


*Figure A2.8. Design 3. This design is based on a glass substrate with Aluminium tracks on top of this and either SiO<sub>2</sub> or 'liquid glass' acting as the insulator between the conducting tracks and the resistive Si layer.*

Out of the three designs, number three seems the most promising. The glass substrate is known to be both optically flat and strong enough to construct the rest of the cell on top. Figure A2.9 shows a possible design of the aluminium tracks. The squares around the edge are 1mm across. These are to connect the device to the drive electronics.

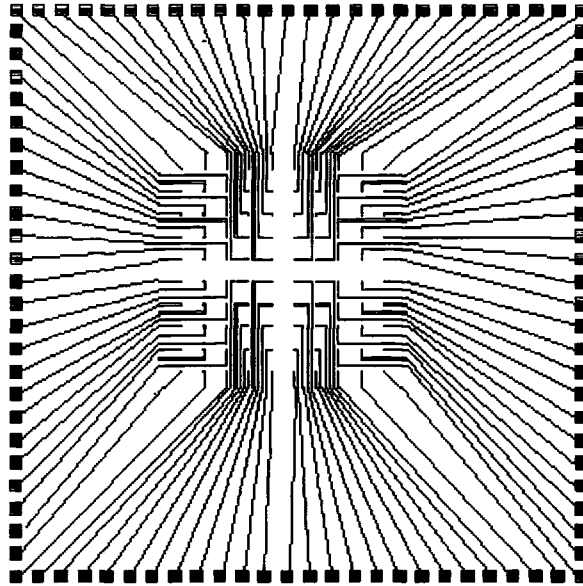


*Figure A2.9. A possible design for the electrode tracks. The central square area would be the active area. The diagonal tracks connect this to the pads around the edge. This is so that wires can be connected to the device.*

## **A2.2 Summary**

In this appendix, an idea for a liquid crystal device with no pixels and the potential for a very large number of degrees of freedom has been described. Three methods of constructing such a device have been described. The actual construction of such a device is outside the realms of this thesis, but such a device will hopefully be built in the future.

## References

- Anderson, 1995 C. S. Anderson, "Fringe visibility, irradiance, and accuracy in common path interferometers for visualization of phase disturbances." *App. Opt.* **34** (32) pp 7474-7485 (1995)
- AOA Adaptive Optics Associates, Inc. 54 Cambridge Park Drive. Cambridge, MA 02140-2308. USA
- Amako, 1993 J. Amako, H. Miura, T. Sonehara, "Wave-front control using liquid crystal devices." *Appl. Opt.* **32** (23) pp 4323-4329 (1993)
- Babcock, 1953 H. W. Babcock, *Publ. Astron. Soc. Pac.* **65** (1953)
- Beckers, 1993 J. M. Beckers, "Adaptive optics for astronomy: Principles, performance, and applications." *Annu. Rev. Astron. Astrophys.* **31** pp 13-62 (1993)
- Biernacki, 1991 P. Biernacki, T Brown, M Freeman, "Polarisation dependence and uniformity of FLC layers for phase modulation." *SPIE Liquid Crystal Devices and Materials* **1455** pp 167-178 (1991)
- Bold, 1997 G. T. Bold, T. H. Barnes, J. Gourlay, R. M. Sharples, T. G. Haskell, "Practical issues for the use of liquid crystal spatial light modulators in adaptive optics." *Opt. Comms.* In print.
- Bonaccini, 1991 D. Bonaccini, G. Brusa, S. Esposito, P. Salinari, P. Stefanini, V. Biliotti, "Adaptive optics wavefront correction using addressable liquid crystal retarders." *Proc. Soc. Photo-Opt. Instrum. Eng.* **1543** (1991)
- Broomfield, 1995a S. E. Broomfield, M. A. A. Neil, E. G. S. Paige, I. O. Thomas, "Binary optical correction of a wavefront aberration using spatial light modulators." *Proc. Soc. Photo-Opt. Eng.* **2534**, 167-175 (1995)
- Broomfield, 1995b S. E. Broomfield, M. A. A. Neil, E. G. S. Paige, "Programmable multiple level phase modulation that uses ferroelectric liquid crystal spatial light modulators." *App. Opt.* **34** (29) pp 6652-6665 (1995)

- Buffington, 1976 A. Buffington, F. S. Crawford, R. A. Miller, C. D. Orth, "First observatory results with an image sharpening telescope." *J. Opt. Soc. Am.* **67** (3) pp 304-305 (1976)
- Buffington, 1977 A. Buffington, F. S. Crawford, R. A. Miller, A. J. Schwemin, R. G. Smits, "Correction of a atmospheric distortion with an image-sharpening telescope." *J. Opt. Soc. Am.* **67** (3) pp 298-303 (1977)
- Buscher, 1997 D. F. Buscher, A. P. Doel, C. N. Dunlop, R. M. Myers, D. J. Robertson, R. M. Sharples, A. J. Vick, A. Zdrozny, "First results from the ELECTRA adaptive optics system." *Proc. Soc. Photo-Opt. Instrum. Eng.* **3126** (1997) In press.
- Cao, 1994 G. Cao, X Yu. "Accuracy analysis of a Hartmann-Shack wavefront sensor operated with a faint object." *Opt. Eng.* **33** (7) pp 2331-2335 (1994)
- Conan, 1995 J. Conan, "Wave-front temporal spectra in high resolution imaging through turbulence." *J. Opt. Soc. Am. A* **12** pp 1559-1570
- Clark, 1994 M. G. Clark "Current status and future prospects of poly-Si devices." *IEE Proc.-Circuits Devices Syst.* **141** (1) pp 3-8 (1994)
- Displaytech Displaytech, Inc. 2602 Clover Basin Drive. Longmont, CO 80503. USA
- Doel, 1990 A. P. Doel, C. N. Dunlop, J. V. Major, R. M. Myers, A. Purvis, M. G. Thompson, "Stellar image stabilisation using piezo-driven active mirrors." In L D Barr, editor, *Advanced Technology Optical Telescopes IV, SPIE* pp 179 (1990)
- Dou, 1995 R. Dou, M. K. Giles, "Closed-loop adaptive optics system with a liquid crystal television as a phase retarder." *Opt. Lett.* **20**, 1583-1585 (1995)
- Efron, 1985 U. Efron, "The Silicon Liquid Crystal Light Valve." *J. Appl. Phys.* **57** (4) pp 1356-1368 (1985)
- Fogel, 1994 D. B. Fogel, "An Introduction to Simulated Evolutionary

- Optimisation." *IEEE Transactions on Neural Networks* **5** (1) pp3-13 (1994)
- Foy, 1985 R. Foy, A. Labeyrie, "Feasibility of adaptive telescope with laser probe." *Astron. Astrophys.* **152**, (2) pp L29-L31 (1985)
- Freeman, 1992 M. O. Freeman, T. A. Brown, D. M. Walba, "Quantized complex ferroelectric liquid crystal spatial light modulators." *Appl. Opt.* **31** (20), pp 3917-3929 (1992)
- Fried, 1965a D. L. Fried, "The Effect of Wave-front Distortion on the Performance of an Ideal Optical Heterodyne Receiver and Ideal Camera." *Conf. on Atmospheric Limitations to Optical Propagation, US. Nat. Bur. Stds. CRPL.* (1965)
- Fried, 1965b D. L. Fried, "Statistics of a Geometric Representation of Wavefront Distortion." *J. Opt. Soc. Am.* **55** (11) pp 1427 (1965)
- Glindemann, 1993 A. Glindemann, R. G. Lane, J. C. Dainty, "Simulation of time-evolving speckle patterns using Kolmogorov statistics." *Journal of Modern Optics* **40** (12) pp 2381-2288 (1993)
- Greenwood, 1977 D. P. Greenwood, "Bandwidth specifications for adaptive optics systems." *J. Opt. Soc. Am.* **67** pp 390-392 (1976)
- Hardy, 1977 J. W. Hardy, J. E. Lefebvre, C. L. Koliopoulos, "Real-time atmospheric compensation." *J. Opt. Soc. Am.* **67** (3) pp 360-369 (1977)
- Hitachi, 1991 Hitachi, "Hitachi LCD Controller/Driver LSI.", 5<sup>th</sup> edition, Hitachi Ltd, Japan, 1991
- Hudgin, 1977 R. Hudgin, "Wave-front compensation error due to finite corrector-element size." *J. Opt. Soc. Am.* **67** (3) pp 393-395
- Hufnagel, 1974 R. E. Hufnagel, *Proc. Topical Mtg. on Opt. Propagation through Turbulence*, Boulder, CO (1974)
- Johnson, 1990 K. M. Johnson, C.C. Mao, G. Moddel, M. A. Handschy, K. Arnett "High-speed, low power optical phase conjugation using a hybrid amorphous silicon/ferroelectric-liquid-crystal device." *Opt. Letts.* **15** (20) pp 1114-1116 (1990)

- Johnson, 1993 K. M. Johnson, D. J. McKnight, I Underwood "Smart Spatial Light Modulators Using Liquid Crystal On Silicon," *IEEE Journal of Quantum Electronics* **29** (2) pp 699-714 (1993)
- Kadono, 1994 H. Kadono, M. Ogusu, S. Toyooka, "Phase shifting common path interferometer using a liquid crystal phase modulator." *Opt. Comms.* **110** pp 39-400 (1994)
- Kim, 1988 H. M. Kim, J. W. Jeong, M. H. Kang, S. I. Jeong, "Phase correction of a spatial light modulator displaying a binary phase-only filter" *Appl. Opt.* **27**(20),4167-4168 (1988)
- Kolmogorov, 1961 A. Kolmogorov, "Turbulence - Classic Papers in Statistical Theory." *Interscience Publishers Inc.* New York (1961)
- Kuo, 1994 C. Kuo, "Optical tests of an intelligently deformable mirror for space telescope technology." *Opt. Eng.* **33** (3) pp 791-799 (1994)
- Kwon, 1984 O. Y. Kwon, "Multichannel phase shifted interferometer." *Opt. Letts.* **9** pp 59-61 (1984)
- Landereth, 1992 B. Landreth, G. Moddel, "Gray scale response from optically addressed spatial light modulators incorporating surface-stabilized ferroelectric liquid crystals." *App. Opt.* **31** (20) pp 3937-3943 (1992)
- Lane, 1992 R. G. Lane, A. Glindemann, J. C. Dainty, "Simulation of a Kolmogorov phase screen." *Waves in random media* **2** pp 209-224 (1992)
- Liu, 1993 J. Liu, K. M. Johnson, M. G. Robinson, "Room temperature 10MHz electro-optical modulation in ferroelectric liquid crystals." *Appl. Phys. Letts.* **62** (9) pp 934-936 (1993)
- Love, 1993 G. D. Love, R. Myers, A. Purvis, R. Sharples, A. Glindemann, "A new approach to adaptive wavefront correction using a liquid crystal half wave phase shifter." *ICO-16 Conference on Active and Adaptive Optics, European Southern Observatory, Garching, Germany* (1993)
- Love, 1994 G. D. Love, S. R. Restaino, G. C. Loos, A. Purvis, "Wavefront

- control using a 64x64 pixel liquid crystal array." *Proc. Soc. Photo-Opt. Instrum. Eng.* **2201** pp1068-1072 (1994)
- Love, 1995 G. D. Love, N. Andrews, P. M. Birch, D. Buscher, C. Dunlop, J. Major, R. Myers, A. Purvis, R. Sharples, A. Vick, A. Zadrozny, S. R. Restaino, A. Glindemann, "Binary adaptive optics: atmospheric correction with a half-wave phase shifter." *App. Opt.* **34** (27) pp 6058-6066 (1995) & Addendum **35** (3) pp 347-350 (1996)
- Love, 1996 G. D. Love, J. Gourlay, "Intensity-only modulation for atmospheric scintillation correction by liquid crystal spatial light modulators." *Opt. Letts.* **21** (18) pp 1496-1498 (1996)
- Love, 1997 G. D. Love, "Wave-front correction and production of Zernike modes with a liquid crystal spatial light modulator." *Opt. Soc. Am.* **36** (7) pp 1517-1524 (1997)
- Mercer, 1996 C. R. Mercer, K Creath, "Liquid crystal point diffraction interferometer for wavefront measurements." *App. Opt.* **35** (10) pp 1633-1642 (1996)
- Moddel, 1987 G. Moddel, K. M. Johnson, M. A. Handschy, "Photoaddressing of High Speed Liquid Crystal Spatial Light Modulators." *Soc. Photo. Instr. Eng.* **754** pp 207-213 (1987)
- Muller, 1974 R. A. Muller, A. Buffington, "Real-time correction of atmospheric degraded telescope images through image sharpening." **64** (9) pp 1200-1210 (1974)
- Neil, 1994 M. A. A. Neil, E. G. S. Paige, "Improved transmission in a two-level, phase only, spatial light modulator." *Elec. Letts.* **30** (5) pp 445-446 (1994)
- Newton, 1704 I. Newton, "Opticks." *Dover Publications, Inc.* New York (1979 Edition) pp110 (1704)
- Noll, 1976 R. J. Noll, "Zernike polynomials and atmospheric turbulence." *J. Opt. Soc. Am.* **66** (3) pp 207-211 (1976)
- O'Meara, 1976 T. R. O'Meara, "The multidither principle in adaptive optics." *J. Opt. Soc. Am.* **67** (3) pp 306-315 (1976)

- Pankove, 1980 J. J. Pankove, "Topics in applied physics: Display Devices." *Springer-Verlag*, Berlin 1980
- Purvis , 1993 A Purvis, N. J. Bailey, G. D. Love J. V. Major, "Optical design, simulation and testing of an addressable 64x64 liquid crystal phase plate." *Proc. Soc. Photo. Opt. Instrum. Eng.* **2000**, pp 96-100 (1993)
- Rigaut, 1991 F. Rigaut, G. Rousset, P. Kern, J. C. Fontanella, J. P. Gaffard, F. Merkle, P. Léna, "Adaptive optics on a 3.6-m telescope: results and performance." *Astron. Astrophys.* **250** pp280-290 (1991)
- Riza, 1994 N. A. Riza, M. C. DeJule, "A novel programmable liquid crystal lens device for adaptive optical interconnect and beamforming applications." *Opt. Comput. Int. Conf.* pp 231-234 (1994)
- Roddier, 1990 N. Roddier, "Atmospheric wavefront simulation using zernike polynomials." *Opt. Eng.* **29** (10) pp 1174-1180 (1990)
- Rousset, 1990 G. Rousset, J. C. Fontanella, P. Kern, P. Gigan, F. Rigaut, P. Léna, C. Boyer, P. Jagourel, J. P. Gaffard, F. Merkle, "First diffraction-limited astronomical images with adaptive optics." *Astron. Astrophys.* **230** pp L29-L32 (1990)
- Schroeder, 1987 D. J. Schroeder, "Astronomical Optics." *Academic Press Inc.* San Diego (1987) pp 319
- Smartt, 1975 R N Smartt, W H Steel. "Theory and Application of Point-Diffraction Interferometers." *Japan J. Appl. Phys.* **14** (1975) Suppl. 14-1
- Smartt, 1979 R. N. Smartt, "Special applications of the point diffraction interferometer." *Proc. Soc. Photo Opt Instrum* **193** pp 35-40 (1979)
- Spektor, 1995 B. Spektor, J. Shamir, "Wave-front analysis using Fresnel lens array." *Opt. Letts.* **20** (13) pp 1504-1506 (1995)
- Srinivas, 1994 M. Srinivas, L. M. Patnaik, "Genetic Algorithms: A Survey." *Computer* **27** (6) pp17-26 (1994)

- Tam, 1990 E C Tam, S Wu, A Tanone, F T S Yu, D A Gregory. "Closed-loop binary phase correction of an LCTV using a point diffraction interferometer." *IEEE Phot. Tech. Letts.* **2**(2), 143-146 (1990)
- Thomas, 1993 I. Thomas, "Programmable correction for optical aberrations using a phase-only spatial light modulator." *MSc degree at the Department of Engineering Science. University of Oxford, UK.* (1993)
- Tyson, 1991 R. Tyson, "Principles of Adaptive Optics." *Academic Press* London (1991)
- Ulrich, 1988 P. B. Ulrich, "Hufnagel-Valley profiles for specified values of the coherence length and isoplanatic patch angle." *W. J Schafer Associates, WJSA/MA/TN-88-013* (1988)
- Wang, 1978 J. Wang, J. K. Markey, "Modal compensation of atmospheric turbulence phase distortion." *J. Opt. Soc. Am.* **68**(1) pp 78-87 (1978)
- Warr, 1995 S. T. Warr, R. J. Mears, "Polarisation insensitive operation of ferroelectric liquid crystal devices." *Elec. Letts.* **31** (9) pp 714-716 (1995)
- Wood, 1996 D. Wood, University of Durham. *Private communication.* (1996)
- Worboys, 1993 M. R. Worboys, G. White, K. Mitchell, A. Mosley "Miniature Display Technologies for Integrated Helmet Systems." *GEC Journal of Research* **10** 2 pp 111-118 (1993)
- Yoshikawa, 1997 N. Yoshikawa, M. Itoh, T. Yatagai "Adaptive Computer-Generated Hologram Using Interpolation Method." *Optical Review* **4** (1B) pp 161-163 (1997)

